Print ISSN 0033-9008
Online ISSN 1880-1765

QUARTERLY REPORT of RTRI

Nov. 2023 Vol. 64 No. 4

CONTENTS

[H] Human factors
[I] Infrastructure
[O] Operations
[R] Rolling stock
[T] Technical system integration and interaction
[W] Weather and climate change

RAILWAY TECHNICAL RESEARCH INSTITUTE

QUARTERLY REPORT of RTRI

Print ISSN 0033-9008
Online ISSN 1880-1765

November 2023 Vol. 64 No. 4

CONTENTS

PAPERS

SUMMARIES

[H] Human factors
[I] Infrastructure
[O] Operations
[R] Rolling stock
[T] Technical system integration and interaction
[W] Weather and climate change

Designing Auditory Warnings for Preventing Arousal-level Decline during Train Operation and Examining Its Effectiveness

Kei HOSHINO **Ayako SUZUKI**
Human Science Laboratory, Ergonomics Division

Masahiro HONDA
Japan Freight Railway Company

Takeshi HARA
Japan Freight Railway Company (Former)

Train driving is characterized by late-night and early-morning shifts when operators may be prone to drowsiness. This study developed and evaluated a system aimed at maintaining and improving arousal level by presenting auditory warnings. First, auditory warnings were designed based on a survey of train operators' opinions. In our experiments, designated auditory warnings were scored and selected in terms of three requirements ("audibility," "distinctiveness," and "arousal function") under train noise. The result shows that the arousal effects of the warning auditory were confirmed by presenting the designed sound during a monotonous task with the train driver environment.

***Key words*:** *auditory warning, sound design, train operators, noise, facial expression*

1. Introduction

Train drivers often work irregular hours, such as late at night or early in the morning when they are generally considered to be more prone to drowsiness, and depending on characteristics of the lines, there are sections where monotonous conditions continue without any braking or need to operate other equipment. According to previous studies, more than 60% of drivers experience drowsiness once a week [1]. For this reason, safety operation devices have been developed to automatically stop trains in the event of abnormal conditions such as a driver falling asleep or fainting. In addition, drivers are encouraged to review their sleeping habits and physical condition in order to prevent drowsiness while on board. As one measure to prevent drowsiness, we have been developing a support device that can detect decreases in the level of arousal during train operation and issue warnings. In this report, we design and verify the effectiveness of a warning sound with a higher arousal effect, assuming the use of "sound" given its ease of introduction.

2. Design of warning sounds

2.1 Setting the purpose and requirements

As a procedure for designing warning tones, previous research has shown a two-step process.

The first step is to organize information to reflect "for what purpose," "when," and "with what sound." The second step is to set acoustic parameters based on this information [2]. The response to the question "for what purpose" is to inform the driver that their arousal level has decreased and that they have entered a dangerous state thereby helping to prevent a lowered arousal level. As for "when," it was decided that it would be the time when a decline in arousal level was detected during train operation.

The "with what sound" was defined as a sound with "audibility (ease of hearing)" that allows the driver to hear the warning sound in the driver's cab when the train is running even in an environment with background noise, "distinguishability (ease of distinguishing other sounds)" that allows the driver to distinguish it from other warning sounds used in the cab, and "functionality" that raises arousal level. The functionality of the sound is that it can be objectively perceived as a biological response, in addition to being subjectively perceived as a signal to "wake up." We designed the warning sound based on the above requirements of "audibility, distinguishability, and functionality."

2.2 Survey of needs at railroad sites regarding warning sounds

Interviews and questionnaires were conducted to clarify driver needs and opinions about warning sounds.

2.2.1 Interviews with supervisory drivers

In order to collect data on needs and opinions about warning sounds and to develop specific items for the questionnaire survey, interviews were conducted with instructors. A total of 16 people were interviewed, including 7 supervisors and 9 managers of operations related to trainers. In response to the question, "What kind of warning sound should be used to support the prevention of alertness loss?" the respondents answered, "A sound that cannot be disturbed by the sound of driving in a tunnel (audibility)," and "A sound that cannot be confused with other sounds heard inside vehicles (distinguishability)." Regarding the "functionality" of the warning sound, the responses were "unpleasant sound, non-monotonous sound, and sound that makes people feel a sense of urgency."

2.2.2 Questionnaire for train operators

From the results of the responses concerning the interview results, the sounds listed in Table 1 were given as specific examples of "sounds that are unpleasant, not monotonous, or cause a sense of urgency," and the respondents were asked to answer one question about what kind of content they would like in the warning sound. Table 1 shows the results of the questionnaire survey of all 117 train

Table 1 Sounds selected by train drivers

Sounds list	Answer Number	%
Sounds like buzzer	29	25
Sounds like alarm clock	27	23
Sounds like electric product	23	19
Sounds like emergency earthquake warning	16	14
Sounds like the Japanese sirens of a police car, Japanese ambulance, or Japanese fire truck	7	6
Sounds that are physiologically repugnant	9	8
Others	6	5
Total	117	100

drivers in charge of sections that include long tunnels. As a result, "buzzer-like sound," which they are accustomed to hearing in trains, was the most frequently selected item, however other items tended to be selected frequently as well.

2.3 Setting auditory parameters

Among the sounds listed in Table 1, "buzzer-like sounds" were excluded from distinguishability, and the other sounds were classified into three types by "pitch variation" as shown in Table 2.

The first was "Type 1," which was high pitched sounds such as an "alarm clock" and the "electronic sound of household appliances," characterized by bell tones and electronic sounds in timbre and high speed in tempo, with little variation in pitch. The second type was "Type 2," which is a sound that evokes a sense of warning through a combination of specific pitches or an increase in pitch, such as the chime sound of the "Earthquake Early Warning." The third type, "Type 3," is a sound that evokes a sense of warning by changing the pitch of the ascending and descending lines of a dissonant sweep, as in the "siren sound of an emergency vehicle."

The characteristics of each of these types of sounds are summarized in Table 2 for the acoustic parameters of frequency, tempo, and timbre. For each of the three types, basic tones (tones 1, 11, and 14) were created by considering "audibility, distinguishability, and functionality" as follows.

First, for "distinguishability," the acoustic parameters underlined in Table 2 were adjusted so that the sound would differ from existing sounds.

Secondly, for "audibility," we took into consideration the fact that sounds above 1000 Hz are included as sounds that are not masked by driving noise [3], that ISO7731 recommends a fundamental frequency of 500 Hz to 2500 Hz for warning sounds [4] , and that the inclusion of a wide frequency band will address age-related hearing loss [5].

For "functionality," in addition to adjusting the fast tempo and timbre, we set "scales" and "additional tones" related to frequencies, as shown in Fig. 1. For the "scale," a chromatic scale with a series of higher or lower semitones was used to design a "trill," which is said to increase urgency, and a sound with a frequency change similar to the "sweep" often used in warning tones [4, 5]. The "added notes" were designed to include a wide frequency range in terms of "audibility" and to enhance the sense of warning by increasing the specific pitch difference of the chords [6].

A total of 15 notes were designed using Singer Song Writer Lite 9.5 (Internet Inc.). All sound durations were set to 4.8 seconds, and the loudness of the sounds was standardized using Adobe Audition (Adobe Corporation).

Table 2 Characteristics of acoustic parameters of each type† Sounds selected by train drivers

Type	Characteristics of frequency	Tempo	Timbre
Type1	High tone, little scale variation, single tone	Fast	Bell & electronic sounds
Type2	High tone, scales with certain ascending fifths, including augmented fourths and tension notes	Fast	Piano
Type3	Medium tone, mixed sweep, and duration, dissonant	Fast	Siren

† : underline the factors most relevant to distinguishability

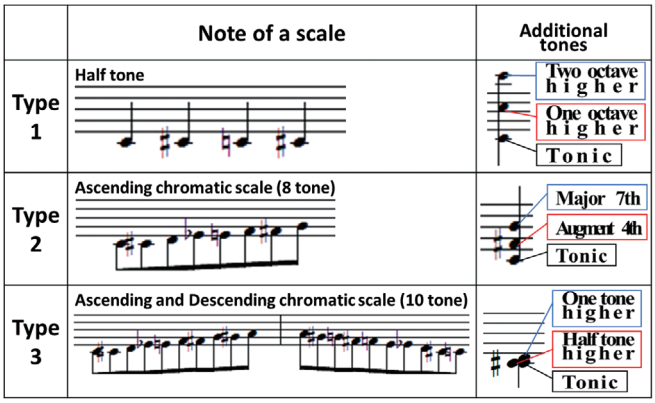

Fig. 1 Example of scale and additional tones for each type

3. Evaluation experiment of warning sound

3.1 Preliminary experiments <impression evaluation and warning sound selection>

Twenty-eight adults participated in the preliminary experiment, ranging in age from 26 to 52 years (mean age 37.0 years, standard deviation 7.23 years).

Impressions of the 15 sounds were evaluated regarding the three requirements" audibility, distinguishability, and functionality," with respect to the sounds that were randomly played on a laptop computer using headphones.

Participants were asked to rate them according to a 7-point Likert scale (1: not applicable at all to 7: very applicable). A rating score of 4 (neither applicable nor not applicable) or higher indicated that each condition was satisfied.

The average of the evaluation scores for each sound is shown in Fig. 2.

Based on these evaluation results, we selected the sounds to be used in the next experiment (comparison of warning sounds against the sound of a running train).

Since the preliminary experiment was conducted to evaluate the "discriminability" of the sounds that we hear in our daily lives, we interviewed one manager with experience as a train driver to exclude the sounds with particularly low "discriminability" in cabs, and four sounds (sound No. 1, sound No. 5, sound No. 9, and sound No. 10) were eliminated.

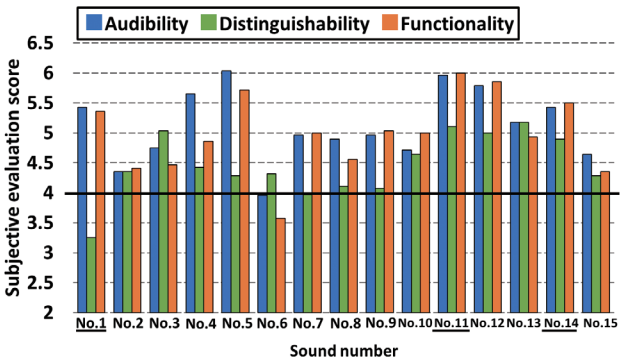

Fig. 2 Results of average evaluation scores for each condition on each sound

Table 3 Setting of auditory parameters for each designing sounds

Type	Sound No.	Pitch and frequency		Additional tone	Tempo (s/one tone)	Timbre
		Lowest	Highest			
1	7	C4	B4	Arg4/ major7	0.075	Glocken spiel
	8	C4	B4	Arg4/ major7	0.075	Electronic
2	**11**	**C6**	**F#7**	Arg4/ major7	**0.1**	**Violin**
	12	C#4	G5	Arg4/ major7	0.1	**Violin**
3	**14**	**G6**	**F#7**	half /one tone higher	**0.0375**	**Violin**
	15	C3	D#4	half /one tone higher	0.1	**Violin**
Filler		C5			1.2	Piano

Of the remaining 11 sounds, the top four sounds with the highest "functionality" scores (sound No. 7, sound No. 11, sound No. 12, and sound No. 14), plus sound No.8 and sound No.15, which are similar to sound No.7 and sound No.14, were selected for evaluation.

In addition, piano sounds (4 sounds of 1.2 seconds at the height of C5) were used as "filler sounds" as a standard for comparison. The composition of the acoustic parameters for a total of seven tones (six tones and filler tones used in the experiment) is shown in Table 3.

3.2 Experiment 1 <Comparison of warning sounds against noise of running train>

Since train running sounds are background noises in train cabs, Experiment 1 was conducted to compare each designed sound while running sounds are heard at the same time, and to select the sound with the highest three requirements ("audibility, distinguishability, and functionality.").

3.2.1 Sound pressure and frequency of driving and warning sounds

In this experiment, as a typical running sound, the running sound when a train passing a switch outside a tunnel was used (hereinafter referred to as "running sound").

The sound pressure of the running sound and the warning sound was 75 dB (L_{Aeq}).

In this experiment, an equivalent continuous A-weighted sound pressure level was measured by a sound level meter (RION-NL52), using a tripod at a height of 1.2 meters to be at the position of participants' right ear. Figure 3 shows the results of the 1/3-octave analysis when the running sound and selected warning sound were presented at 75 dB (L_{Aeq}).

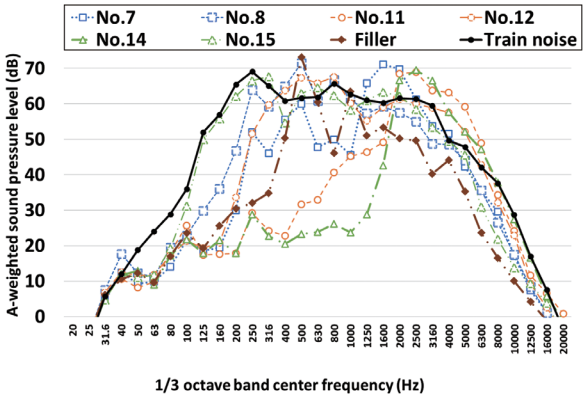

Fig. 3 1/3 octave band sound pressure level of each sound and noise

3.2.2 Participants and experimental environment

Twenty-seven adults participated in the experiment, ranging in age from 26 to 56 years (mean age 37.0 years, standard deviation 7.63 years).

The participants sat in chairs 1 meter away from the speakers (WS-X66A Panasonic wireless powered speaker system) placed at 1-meter intervals on the left and right sides of their desks. The left speaker presented the train running noise and the right speaker presented the warning sound respectively.

3.2.3 Experimental Procedure

Before participation, all individuals provided their written informed consent.

All sounds were compared using a Thurston's one-pair comparison method. A total of 21 pairs were presented in random order of two sounds from a total of seven sounds shown in the Table 3 against the sound of a running train.

About 5 seconds after the train running noise was presented, the first of the two warning sounds was presented, and the second sound was presented after an interval of about 4 seconds. The second tone was presented after an interval of about 4 seconds. After the two tones were presented, the participants were asked to choose the one they rated higher among the two tones for the three requirements of "audibility, distinguishability, and functionality," and to fill out a survey form.

3.2.4 Results and Discussion of Pairwise Comparisons

The results of the pairwise comparisons are shown in Fig. 4. Against the sound of a running train, sound No. 11 was selected as the best sound because it was the most highly evaluated sound for all three requirements of "audibility, distinguishability, and func-

tionality."

Previous studies have suggested that sounds in a 2000-4000 Hz band may be easier to listen to against the sound of a running train [7], and the frequency analysis in Fig. 3 shows that the components in these frequency bands are larger for sound No. 11, which may have influenced the evaluation of "audibility" and "functionality."

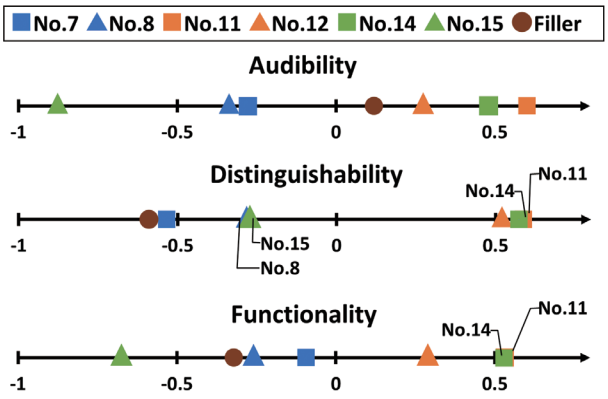

Fig. 4 Results of pairwise comparisons for each condition on each sound†

†: The filler sound is the piano sound used as a reference for comparison (C5, 4 notes of 1.2 seconds)

3.3 Experiment 2 <Assessment of functionality at reduced arousal level >

The "functionality" of the warning sound was tested on participants with reduced arousal levels against the background noise of a running train.

3.3.1 Warning sounds and train running noise

Sound No. 11, the selected sound, is hereinafter referred to as the "warning sound."

The background noise was the sound of a running train measured in a tunnel section (hereinafter referred to as "tunnel running sound") to simulate an environment during a driving operation in a tunnel section, which is a considered to be prone to continuous monotonous state.

As in Experiment 1, the sound pressure was set to 75 dB (L_{Aeq}) for both the warning sound and the running sound.

3.3.2 Participants

Twenty-nine adults participated in the experiment, ranging in age from 20 to 57 years (mean age 38.2 years, standard deviation 10.8 years).

All participants had a driver's license and had no problems with their vision, hearing, or health. Participants were required to sleep two hours less than usual the previous night or to sleep four hours if that would result in less than four hours of sleep.

These conditions were confirmed before the experiment by the participants' self-reports.

3.3.3 Experimental Environment

The experiment was carried out on a train driving simulator to simulate conditions during a driving operation. Three speakers were placed approximately 1 meter in front of the participant on the back side of the simulator. One speaker (WS-X66A wireless powered speaker Panasonic) was placed front and center to broadcast the warning sound, and two other speakers (MSR400 Powered Speaker YAMAHA) were placed 75 cm apart to the left and right of the center of the floor to broadcast the train running sound. The lighting in the laboratory was turned off in order to reproduce the environment of a driver's cab late at night when arousal levels tend to decrease.

A monotonous task was displayed on the simulator monitor, and the participants operated buttons on a keyboard placed on the simulator table.

During the monotonous task, the tunnel running sound was broadcasted at 75 dB (L_{Aeq}) through two speakers.

The tunnel running sound was also broadcasted at 65 dB (L_{Aeq}) during breaks and when participants responded to survey forms, so that the train running sound would not be interrupted.

3.3.4 Experimental Procedure

After written informed consent was obtained from each participant, a heart rate monitor (PolymatePocket MP208 Miyuki Giken) was equipped. Then, the participants were instructed to sit in the driving simulator and practiced keyboard operations for the monotonous task several times. Five to six sessions of the task were conducted as shown in Fig. 5. The total experiment time was 120 minutes.

Each session consisted of a 12-minute monotonous task, followed by a break of about 2 minutes to answer a survey form and to drink water.

As shown in Fig. 6, the monotonous task was to press the "×" button on the keyboard as quickly and accurately as possible when a circle composed of multiple "○" signs was displayed on the monitor and contained a "C-mark," or to press the "○" button when it did not contain a "C-mark." The number of "○" that make up the circle is randomly changed from 5 to 15 on each trial. Also, if there is a "c mark," the position of the "c mark" is randomly changed with each trial.

The warning tone was presented once during each of the two sessions, with at least one session in between, for a total of two warning tones per person.

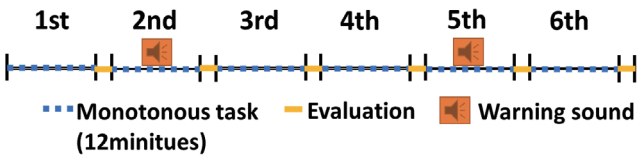

Fig. 5 Example of experimental time course

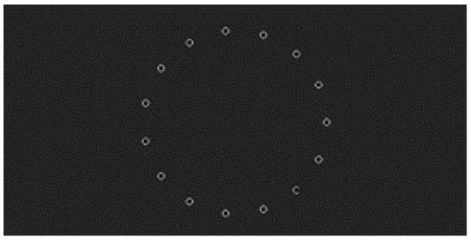

Fig. 6 Example of Monotonous task

3.3.5 Measurements

The following four items were measured to verify the functionality.

(i) Drowsiness rating (an objective index): Average of the values obtained by recording facial images during the task and rating facial expressions (1: not at all sleepy, 2: somewhat sleepy, 3: sleepy, 4: very sleepy, 5: extremely sleepy) [8] at 5-second intervals for 1 minute before and after the warning tone.

(ii) Task reaction time (performance index): Average reaction time for 30 seconds before and after the warning sound for the keyboard button operation time of the monotonous task.

(iii) Heart rate (physiological index): Instantaneous heart rates calculated from the RRI (heart rate interval) before and after the warning sound

(iv) Warning evaluation (subjective index): 9-point rating of subjective arousal effect of the warning sound, which is answered during the break time of the session in which the warning sounded.

3.3.6 Data Analysis

As shown in Table 4, the measured data were divided into three groups according to the arousal level at the time the warning sound was broadcasted, to confirm the effect of the warning sound in preventing a fall in arousal. In the three groups, drowsiness ratings 1 and 2 were defined as "low," drowsiness ratings 3 as "moderate," and ratings 4 and 5 as "high."

For indices (i), (ii), and (iv), a total of 58 data were obtained because the warning sound was presented twice for each of the 29 participants. For the heart rate of 18 participants for whom there was no noise contamination or malfunction of the measurement device, a total of 36 data were obtained from the two times the warning tone was broadcasted.

Table 4 Number of data for each level of drowsiness†

group	Drowsy rate	1st sound	2nd sound	Total	Total (each groups)
"Low" drowsiness	1	3 (2)	1 (1)	4 (3)	22 (17)
	2	12 (8)	6 (6)	18 (14)	
"Moderate" drowsiness	3	5 (2)	10 (6)	15 (8)	15 (8)
"High" drowsiness	4	5 (2)	6 (2)	11 (4)	21 (11)
	5	4 (4)	6 (3)	10 (7)	
Total		29 (18)	29 (18)	58 (36)	58 (36)

† : The number in parentheses is the number of heart rate data acquired

3.3.7 Results and Discussion

(1) (i) Drowsiness rating and (ii) Task reaction time

Figure 7 shows the change in the sleepiness rating for each group during the 1-minute period before and after the warning.

Figure 8 shows the change in reaction time to the monotonous task for 30 seconds before and after the sound of the warning for each group.

The median values of the sleepiness rating and task reaction time were compared by Wilcoxon signed test, and the median values of the sleepiness rating and task reaction time significantly decreased after the warning compared to before the warning in "high" drowsiness group. ($p<0.05$).

These results suggest that the warning sound is more effective when the degree of arousal decrease is high (i.e., when sleepiness is high) from the viewpoints of the objective and performance indices.

(2) (iii) Heart rate and (iv) Warning evaluation

Figure 9 shows the average heart rate for 10 seconds before and after the warning sound and for 1 minute after the warning was presented.

A two-way analysis of variance was conducted with the time change as a within-subjects factor and the degree of arousal reduction as a between-subjects factor, and a significant main effect was found for the time change before and after the warning broadcast ($F(2,66) = 13.77$, $p<0.001$). Multiple comparisons revealed that the mean heart rate significantly decreased 10 seconds after the warning

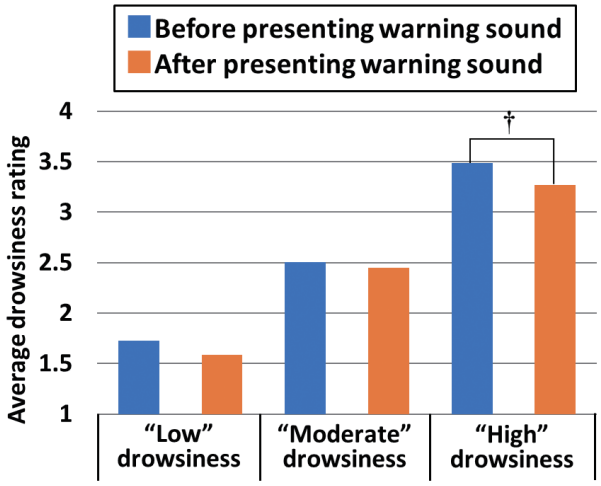

Fig. 7 Results of average drowsiness rating for each group

†: As a result of statistical analysis, in "high" drowsiness group, the drowsiness rating significantly decreased before and after the warning sound broadcast ($p < 0.05$).

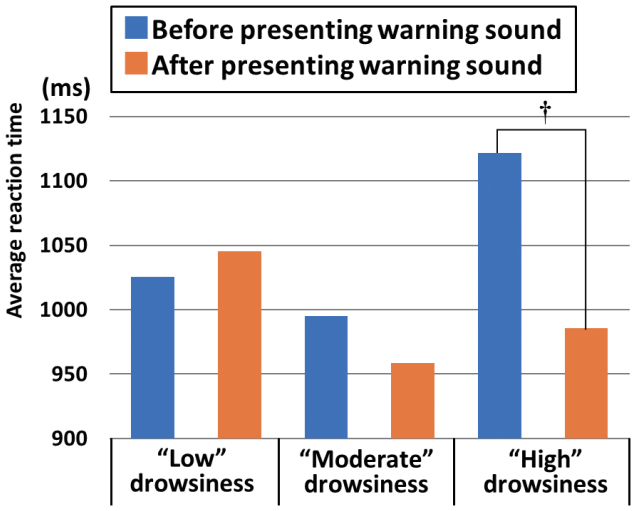

Fig. 8 Results of average reaction time for each group

†: As a result of statistical analysis, in "high" drowsiness group, the reaction time significantly decreased before and after the warning sound broadcast ($p < 0.05$).

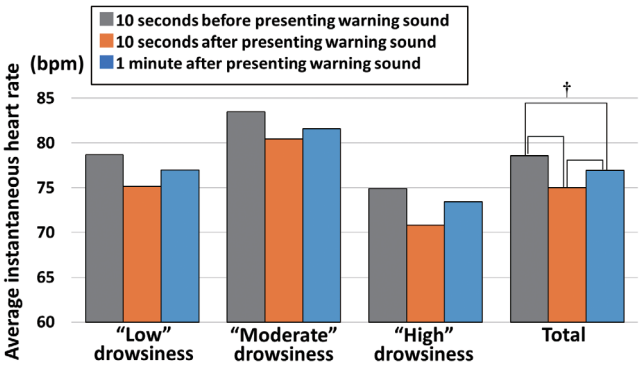

Fig. 9 Results of average instantaneous heart rate for each group

†: As a result of statistical analysis, the average instantaneous heart rate decreased significantly 10 seconds after sound broadcast compared to 10 seconds before broadcast ($p<0.001$) and 1 minute after broadcast ($p<0.05$). At 1 minute after broadcast, the mean value was significantly lower than at 10 seconds before broadcast ($p<0.05$).

Table 5 Results of subjective evaluation for arousal function

Awake level	Number of answers			Total	%
	Low	Moderate	High		
1. Very awake	1	1	2	4	7
2. Between 1 and 3	1	1	5	7	13
3. Awake	8	4	2	14	26
4. Between 3 and 5	1	1	0	2	4
5. Slightly awake	8	6	7	21	39
6. Between 5 and 7	1	1	2	4	7
7. Noticed but not awake	1	0	1	2	4
8. Between 7 and 9	0	0	0	0	0
9. Not at all noticed	0	0	0	0	0
Total	21	14	19	54	100
Average	4.00	3.93	3.79	3.91	

compared to 10 seconds before the warning ($p<0.001$). The mean heart rate significantly decreased at 10 seconds after the warning compared to 1 minute after the warning ($p<0.05$). Furthermore, the mean heart rate significantly decreased at 1 minute after the warning compared to 10 seconds before the warning ($p<0.05$). There was no significant difference in the main effect of the magnitude of arousal reduction and the interaction effect.

Table 5 shows the results of the subjective evaluation of the effect of the warning broadcast, excluding omitted responses. More than 90% of the respondents responded to the effects of warning tones from options 1 to 6.

It is generally believed that a decreased heart rate is observed when the parasympathetic nervous system is dominant and when relaxation or arousal level is lowered. This response is called the "orienting response" and is thought to be related to the state of attention and concentration [9]. Considering the high percentage of people who felt the effect of the warning in the results of subjective evaluation of the sound of the warning, it is possible that the decrease in heart rate due to the broadcast of the warning reflects the "orienting response." Therefore, it is suggested that the designed warning sound functions as a sound stimulus that promotes moderate alertness.

4. Evaluation by train operators

The effectiveness of the warning sound was verified for train drivers to confirm its practicality, since the experiments up to Chapter 3 were conducted with participants who were recruited from the general population.

4.1 Impression Evaluation

Train drivers were asked to evaluate their impressions of the warning tones. Considering the time required to obtain the cooperation of the train drivers, five sounds were selected from the seven used in Experiment 1: sound No. 7, sound No. 8, sound No. 11, sound No. 15, and the filler sound. These warning sounds were recorded with the sound level meter, which was output at 68 dB (L_{Aeq}) when the running sound was presented as background noise 75 dB (L_{Aeq}). The sound sources of these recorded warning sounds with train running sound were used for impression evaluation. The sound files were presented from a laptop computer at a constant volume that was easy to hear during the impression evaluation. The evaluation items were the same as in the preliminary experiment (Section 3.1).

Ninety-nine active train drivers (mean age: 39.3 years, standard deviation: 8.72 years) between 21 and 62 years old participated in the impression evaluation.

As a result, as shown in Fig. 10, all the evaluation values of "audibility, distinguishability, and functionality" for sound No. 11 exceeded 5 (more or less true), which was the highest among the five tones. Therefore, it was confirmed that the results of the general participants' evaluations tended to coincide with those of the train drivers.

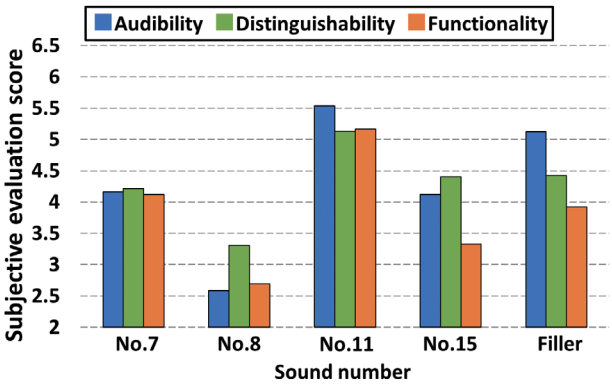

Fig. 10 Results of average evaluation scores for each condition of train drivers

4.2 Warning tone broadcast on operating trains

The practicality of the warning sound was verified by conducting a test in which a warning sound was presented to two active drivers and one supervisor driver when their arousal level decreased in an actual running train.

The warning sound "No.11" was presented at a sound pressure of 75 dB (L_{Aeq}) at the driver's right ear from a speaker (MSP3 Powered Monitor Speaker YAMAHA) under the passenger seat in the driver's cab.

For the two active drivers, the sound of the warning was presented in the driver's cab while the train was in operation, and the effectiveness of the warning was evaluated after the end of the train

ride. A simplified 6-point scale (1: very awake to 6: not at all noticed) was used, taking into account the workload and two active drivers provided a score of "1 (very awake)" and "3 (somewhat awake)."

In order to have the driver examine the effect of the warning sound in a drowsier state, the supervisor driver was seated in the cab facing the opposite direction of travel, where he was not driving. The results of the evaluation using the items in Table 5 used in Experiment 2 (Section 3.3) showed that the response was "2 (between [very awake] and [awake])."

5. Summary

In this study, we designed a warning sound that "assists in preventing the lowering of the arousal level during train operation" and confirmed that it satisfies "audibility, distinguishability, and functionality."

In addition, the practicality of the warning sound was confirmed by the fact that the sound presented while a train was running prevented the lowering of the arousal level.

On the other hand, it is necessary to continue to study the timing of the warning sound and the actions to be taken by train drivers after the warning sound is given, in cooperation with railroad companies.

(This paper is based on Reference 10, with additions and modifications [10].)

References

[1] Sawa, M., Yamauchi, K., Suzuki, A., Murakoshi, A. and Suzuki, D., "Occurrence Factors of Sleepiness of Freight Train Drivers," *RTRI report*, Vol. 26, No. 1, pp. 5-10, 2012 (in Japanese).

[2] Wake, S., Uwakubo, S., Fukuzumi, S., Asahi, T. and Hiroaki, T., "A Case Study on Establishing an "Matrix Design Method for Auditory Signals" for Human Interface," *The Transactions of the Institute of Electronics, Information and Communication Engineers*, Vol. 82, No. 10, pp. 1721-1728, 1999 (in Japanese).

[3] Shito, K. and Endo, H., "Interior Noise of Subway Vehicle," *The Journal of the INCE of Japan*, Vol. 7, No. 5, pp. 261-266, 1983 (in Japanese).

[4] International Organization for Standardization, "ISO 7731:2003(E) Ergonomics – Danger signals for public and work areas – Auditory danger signals," *ISO*, 2003.

[5] Kuwano, S., "Psychological Evaluation of Auditory Warning Signals," *The Journal of the INCE of Japan*, Vol. 25, No. 1, pp. 3-7, 2001. (in Japanese).

[6] Hayata, Y. and Tanaka, M., "Emergency sound intervals for danger alert," presented at *The 7th International Symposium on Affective Science and Engineering*, Online, March 9, 2021, pp. 1-4.

[7] Hashimoto, M. and Wada, K., "Evaluation of voice frequency spectrum and audibility," *The Japanese Journal of Ergonomics*, Vol. 57, No. Supplement, pp. 2E1-1, 2021 (in Japanese).

[8] Kitajima, H., Numata, N., Yamamoto, K., and Goi, Y., "Prediction of Automobile Driver Sleepiness (1st Report, Rating of Sleepiness Based on Facial Expression and Examination of Effective Predictor Indexes of Sleepiness)," *The Japan Society of Mechanical Engineers Collected Papers (C book)*, Vol. 63, No. 613, pp. 93-100, 1997 (in Japanese).

[9] Ohsuga, M., "Estimation of Driver's States using Autonomic Indices," *Journal of Society of Automotive Engineers of Japan*, Vol. 64, No. 10, pp. 24-29, 2010 (in Japanese).

[10] Hoshino, K., Suzuki, A., Honda, M., and Hara, T., "Designing Auditory Warnings for Preventing Arousal-Level Decline during Train Operation and Examining its Effectiveness and Practicality," *The Transactions of Human Interface Society,* Vol. 24, No. 4, pp. 215–230, 2022 (in Japanese).

Authors

Kei HOSHINO
Researcher, Ergonomics Laboratory, Human Science Division
Research Areas: Acoustics, Biosignal Processing

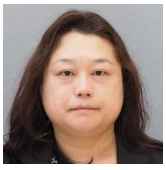

Ayako SUZUKI, Ph.D.
Senior Chief Researcher, Ergonomics Laboratory, Human Science Division
Research Areas: Occupational Health Psychology, Ergonomics

Masahiro HONDA
Deputy Leader, Japan Freight Railway Company
Research Areas:

Takeshi HARA
General Manager, Japan Freight Railway Company (Former)
Research Areas:

Experimental Verification of Handrail Effect on Injury Reduction for Passengers Seated in Long Seats in the Event of a Collision

Kazuma NAKAI **Shota ENAMI**
Ergonomics Laboratory, Human Science Division

In order to enhance the safety of passengers seated in long seats, it is important to identify the risk to passengers in the event of a collision. In a prior study, case studies using numerical analysis showed that the installation of handrails reduced the secondary impact velocity of passengers' heads. The purpose of this study is to investigate the effect of handrails in reducing the severity of injury to passengers through a series of physical tests. The experiment results showed that the occupant behavior and the severity of injury to the occupants were dependent on the initial seating position, and that the severity of head and thorax injuries decreased significantly in the presence of handrails.

***Key words*:** *crashworthiness, sled test, interior fitting, long seats*

1. Introduction

Although various approaches are adopted to prevent railway accidents, some situations cannot be prevented by railway operators alone, such as entry onto a level crossing immediately prior to a train approaching or natural disasters, and so on. As such, from a safety perspective it is important to consider counter measures to reduce the damage caused by accidents.

Collisions have two phases. The first, known as the "primary impact" is the collision of a rail vehicle with another rail vehicle or an obstacle on the track. Design approaches to reduce damage from primary impact include measures such as increasing car body structure rigidity to provide more space inside the vehicle and installing crushable zones to reduce the impact inside the vehicle. The second phase, known as "secondary impact" refers to when passengers collide with the interior fittings or other passengers following a primary impact. Design approaches against secondary impact include measures to reduce the degree of passenger injury in case of a collision with on-board interior fittings or other passengers. The study in this report focuses on secondary impact. This study is based on the scenario of a head-on collision between a train and a dump truck, drawing on the characteristics level crossing accidents in Japan which have caused serious damage.

The UK's Railway Safety and Standards Board has established Railway Group Standards GM/RT2100 (RGS) [1] to develop a crashworthy structural design, which is considered to be one of the most advanced specifications of its kind. This standard provides a physical test method for evaluating the injury to passengers seated in a transverse seating arrangement as shown in Fig. 1. However, there is no standard to evaluate the injury to passengers occupying long seats. In other words, an evaluation method for the passengers occupying long seats has yet to be established. Some large cities in Japan have commuter trains mostly equipped with long seats, similar to some metro trains in European countries. Therefore, it is important to ensure the safety of the passengers sitting on the long seats.

Recently, we have conducted research on passengers sitting on long seats [2–4]. A previous study [4] showed that the installation of handrails in long seats reduces the velocity of secondary impact with interior fittings at the end of long seats. This was ascertained through case studies using numerical simulations on the assumption that interior fittings are rigid. This means that the previous study did not evaluate the severity of injury to passengers. Therefore, the purpose of this study is to estimate the severity of injury to occupants on long seats and to verify the effect of reducing the severity of injury to passengers using handrails in a physical test.

2. Sled test methods

The severity of injury to passengers was estimated using an experimental program based on the physical impact test, which is called a "sled test" to simulate the scenarios of a level crossing accident. The dynamic acceleration pulse in the direction of travel was used as the input condition as shown in Fig. 2(a). An ES-2 dummy [5] was chosen to represent the seated passengers. This type of dummy was selected because of its capability to assess side-impact injury. The existing bench-end partition was arranged at the end of the long seat on the floor. The outside of the bench-end partition is covered with resin materials. The inside is comprised of the steel frame and polyurethane filled into the frame. The bench-end partition was fitted in a fixed position on the train as shown in Fig. 2(b). This type of partition is common in Japan.

2.1 Input acceleration pulse

In the event of a collision, there is relative deceleration (acceleration) between the car body and the passengers on board. Accelerations in the direction of the track were used as input. The accident scenario was a train collision with a 22-tonne dump truck at 54 km/h on a level crossing. The acceleration pulse was generated by using numerical simulation as shown in Fig. 3 [6-7].

2.2 Initial seating positions

Dummies were seated on the long seats. Four initial seating positions (Positions A, B, C, A and C) without handrail, Position C with handrail and Positions A and C with handrail were used, as

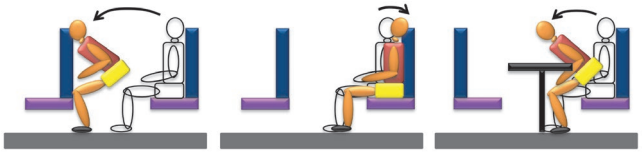

Fig. 1 Secondary impact on transverse seats

shown in Fig. 4, comprising twelve test conditions (Table 1). The T09-T12 test was conducted to assess the effect of using handrails on passengers seated on long seats. Position A is next to the bench-end partition (Fig. 4(a)). Position B is the second seat from the bench-end partition (Fig. 4(b)). Position C is the third seat from the bench-end partition (Fig. 4(c)). The conditions of position A and C were carried out to assess the effect of secondary impact between passengers (Fig. 4(d)). Position C with handrail (Fig. 4(e)) and Positions A and C with handrail (Fig. 4(f)) were carried out to assess the effect of the handrail on injury reduction. T02-T04, T05-T07 and T09- T11 were carried out three times under the same conditions to confirm the degree of variation in the measurements.

2.3 Evaluation method

The dummy behavior was assessed using the collision position of the dummy's head to the bench-end partition, and the Secondary Impact Velocity of the dummy's head to the bench-end partition (SIVH). The kinematic motion of the dummy was measured using high-speed cameras (MEMRECAM GX-1). The recording flame rate was set 1000 Hz. The injuries caused to the dummy were assessed using Head Injury Criterion (HIC), Rib Deflection Criterion (RDC) and Pubic Symphysis Peak Force (PSPF), which have been extensively used for assessing the safety of automotive occupants [5]. The limit values (IARVs: Injury Assessment Reference Values) for HIC, RDC and PSPF were 1,000, 42 mm and 6 kN, respectively. The HIC is calculated based on the data of three-axis translational resultant acceleration by using (1). The thorax of the dummies consists of three rib modules, i.e. the upper rib, the middle rib and the lower rib. The maximum values measured in the rib deflection in

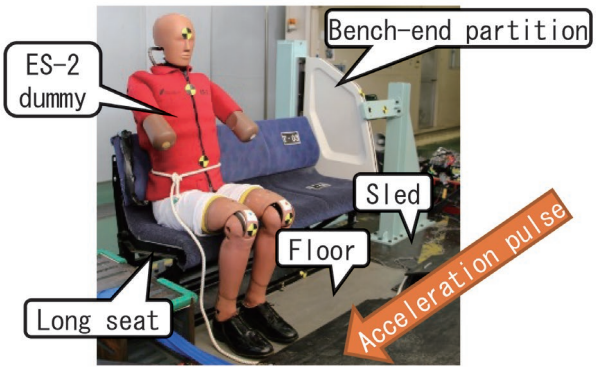

(a) Layout on the sled

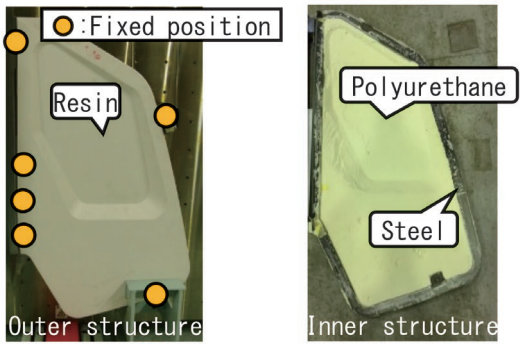

(b) Structure and material of bench-end partition

Fig. 2 Condition of the sled test

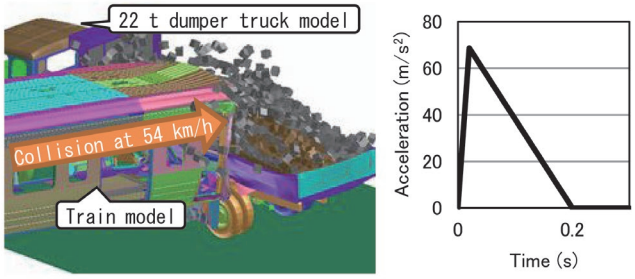

Fig. 3 Accident scenario and acceleration pulse

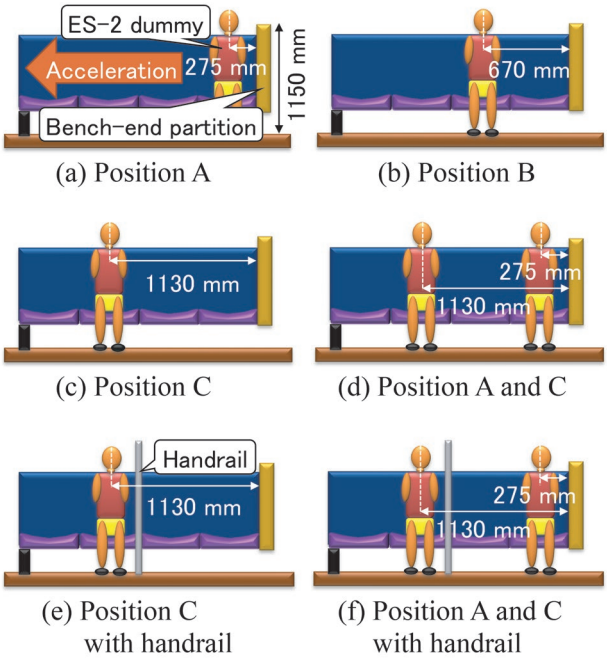

Fig. 4 Initial seating conditions

Table 1 Test conditions

Test ID	Initial seating position	Handrail
T01	Position A	Without
T02	Position B	
T03	Position B	
T04	Position B	
T05	Position C	
T06	Position C	
T07	Position C	
T08	Position A and C	
T09	Position C	With
T10	Position C	
T11	Position C	
T12	Position A and C	

each of the rib modules was defined as RDC. The maximum values measured in the pubic symphysis force was defined as PSPF.

$$HIC = \left\{ (t_2 - t_1) \left[\frac{\int_{t_1}^{t_2} a(t)\, dt}{(t_2 - t_1)} \right]^{2.5} \right\}_{max} \quad (1)$$

$$|t_1 - t_2| \leq 36 \text{ ms}$$

3. Results and Discussion

3.1 Evaluation of behavior

The ES-2 dummies were seated in the initial positions on the long seat (Fig. 5). The behavior of the dummies during the secondary impact is also shown in Fig. 5. The behavior of the dummy whose seating condition was in Position A was a secondary impact of chest on the partition followed by a secondary impact of head (Fig. 5(a)). The behavior of the dummy whose seating condition was in Position B was a secondary impact of shoulder on the partition followed by a secondary impact of head (Fig. 5(b)). Figure 5(c) depicts that the dummy's head collided with the partition before the remaining parts of the dummy. Figure 5(d) depicts that the dummy's head at Position C collided with the other dummy's head and that the dummy's shoulder at Position C collided with the other dummy's right thorax. Figure 5(e) shows that the secondary impact position of the dummy's head was lower than without the handrail. Figure 5(f) depicts that the dummy's head at Position C collided with the other dummy's shoulder. It was observed that the behavior of the dummies depends on their initial seating positions and the presence of the handrail, on the same acceleration condition.

Figure 6 shows the comparison of SIVH to quantitatively assess the behavior of the dummy' head. The average values of Positions B and C were calculated. The conditions of Positions B and C were each carried out three times. The error bar shows the maximum value and the minimum value. Figure 6(a) shows that the SIVH increases with distance from the bench-end partition. Figure 6(b) shows that the SIVH at Position C decreases by 20% with the use of handrails.

3.2 Overall evaluation of Injury

The average values, maximum values and minimum values of HIC, RDC and PSPF are shown in Fig. 7. To identify high-risk initial positions in terms of head, thorax and pelvis injuries, HIC, RDC and PSPF were standardized by dividing their respective limit and compared. This figure shows that HIC values are higher than any other values and that PSPF values are lower than any other values.

3.3 Evaluation of HIC

HIC values at position C were higher than IARVs as shown in Fig. 8. Figure 8(a) shows that HIC values increase with distance from the bench-end partition. Figure 8(b) shows that the HIC at Position C decreases by 50% with the use of handrails. Figure 8(c) shows that the HIC for both Positions A and C also decrease with the application of handrails. It was observed that the HIC of the dummies was dependent on the initial seating position and the presence of handrails at an identical acceleration pulse.

3.4 Evaluation of RDC

Figure 9(a) shows that RDC values are lower than the IARVs regardless of the initial seating position. Figure 9(b) shows that the RDC for Position C decreases significantly with the use of handrails. RDC was higher than the IARVs at position A as shown in Fig. 9(c) because of the collision between the dummy's thorax at position A and the dummy's shoulder at position C. This figure shows that the RDC for Position A decreases significantly with the use of handrails. It was observed that the RDC of the dummies was dependent on the handrail at an identical acceleration pulse.

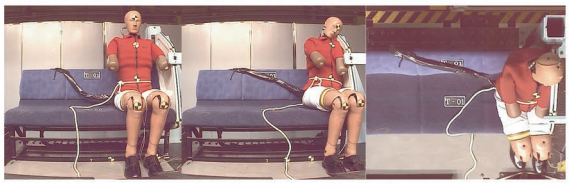

(a) Position A（T01）

(b) Position B（T02）

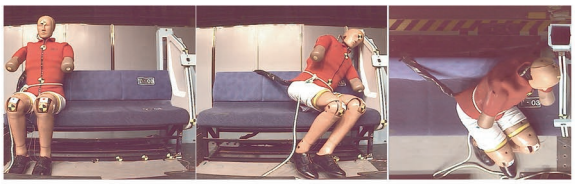

(c) Position C（T05）

(d) Position A and C（T08）

(e) Position C with handrail（T09）

(f) Position A and C with handrail（T12）

Fig. 5 Behavior of dummy

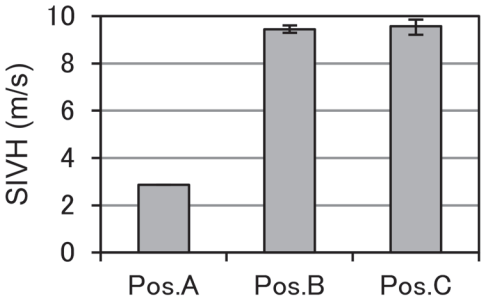

(a) Pos. A～C without handrail
(T01-T07)

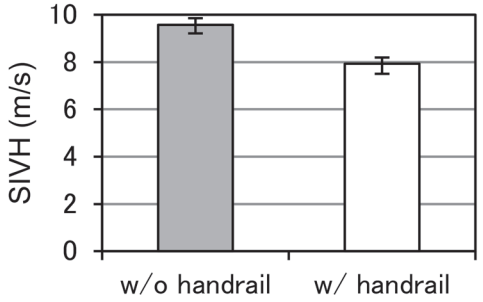

(b) Pos. C w/o and w/ handrail
(T05-T07, T09-T11)

Fig. 6 Comparison of SIVH

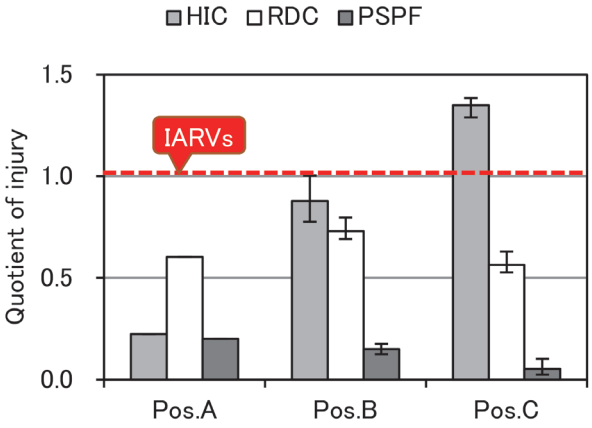

Fig. 7 Comparison of injury values

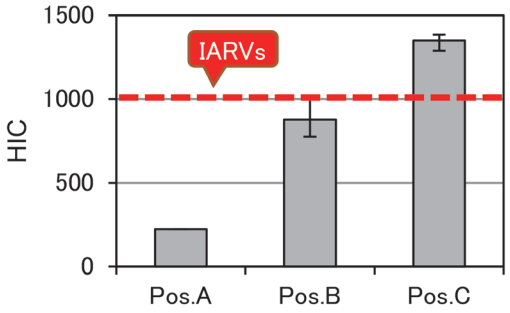

(a) Pos. A～C without handrail
(T01-T07)

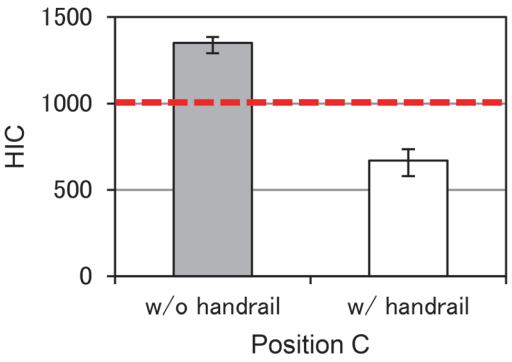

(b) Pos. C w/o and w/ handrail
(T05-T07, T09-T11)

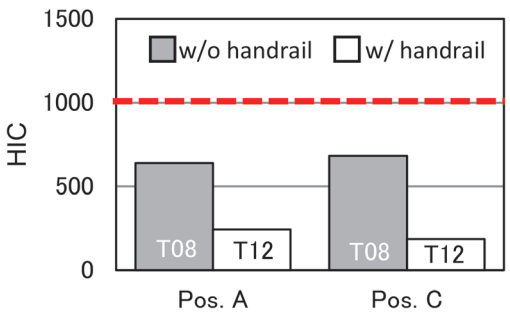

(c) Pos. A and C w/o and w/ handrail
(T08 and T12)

Fig. 8 Comparison of HIC

3.5 Evaluation of PSPF

Figure 10(a) shows that the PSPF values are less than the IARVs regardless of the initial seating position. Figure 10(b) and Fig. 10(c) show that both PSPFs were almost the same regardless of the presence or not of handrails. It was observed that the PSPFs of the dummies were very low and there was no handrail effect on injury reduction.

3.6 Effect of handrail

The above results show that the HIC at Position C decreased significantly in the presence of handrails. This section discusses the reasons for this result.

The first reason is that the SIVH at Position C with the handrail was lower than the SIVH without the handrail (Fig. 6(b)). This effect on SIVH reduction was also observed in previous research using numerical simulation [4]. The second reason is that the collision position of the dummy's head was more flexible in the presence of handrails than in the absence of handrails (Fig. 11). The inner parts of the partition were reinforced with a structural element. Therefore, it was observed that the stiffness of the partition varies with position.

The severity of injury to the passengers depends on the secondary impact velocity and the collision position. Therefore, there is a possibility that the handrail may not have much effect in reducing the severity of injury if the collision position of the head in the pres-

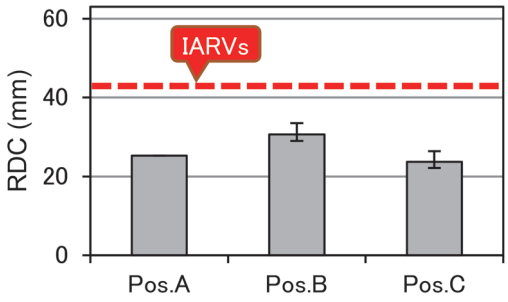

(a) Pos. A～C without handrail
(T01-T07)

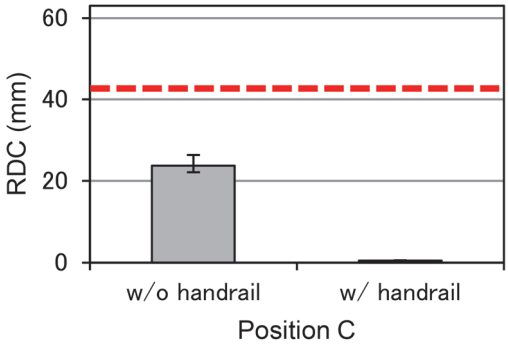

(b) Pos. C w/o and w/ handrail
(T05-T07, T09-T11)

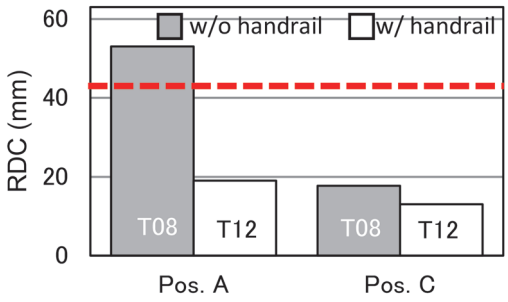

(c) Pos. A and C w/o and w/ handrail
(T08 and T12)

Fig. 9 Comparison of RDC

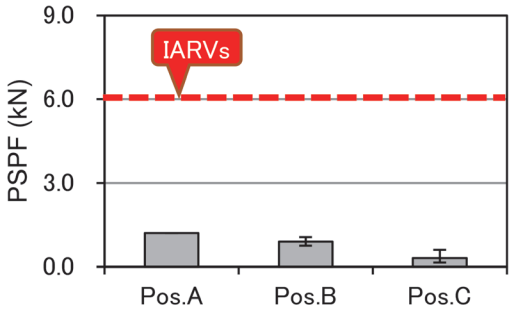

(a) Pos. A～C without handrail
(T01-T07)

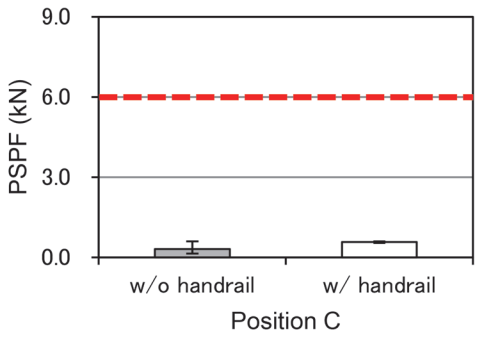

(b) Pos. C w/o and w/ handrail
(T05-T07, T09-T11)

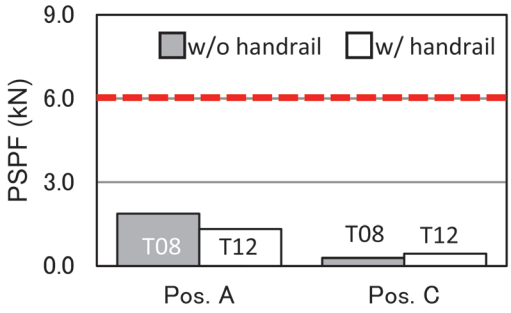

(c) Pos. A and C w/o and w/ handrail
(T08 and T12)

Fig. 10 Comparison of PSPF

ence of handrails is harder than the collision position in the absence of handrails.

4. Conclusions

The objective of this study was to estimate the severity of injury to occupants in long seats and to consider mitigation measures using sled tests. The occupant behavior and injury severity of a dummy were quantified in 12 test conditions. It was found that the behavior, HIC and RDC of the dummies depended on the initial seating position and the handrail at an identical acceleration pulse, and that the severity of head and thorax injuries decreased significantly with the installation of handrails.

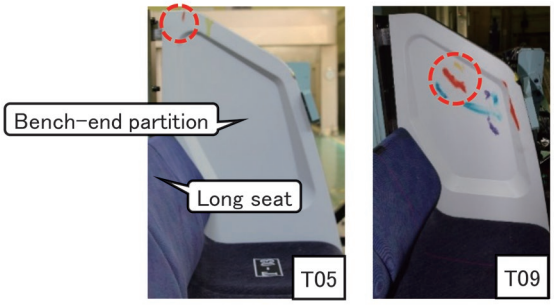

Fig. 11 Collision position to bench-end partition of the dummy's head

The acceleration pulse condition was limited in this work. Therefore, further studies using sled tests and numerical simulation are needed to develop effective measures to enhance the safety of occupants in long seats.

This study was published in Transactions of the JSME (in Japanese) in 2019 [8].

References

[1] RSSB, "Railway Group Standards GM/RT 2100 issue 5: Requirements for rail vehicle structures," 2012.

[2] Nakai, K., Omino, K., Shiroto, H. and Suzuki, D., "Simulation of Passenger Behaviour on Board a Commuter Train in the Event of a Level Crossing Accident," *Quarterly Report of RTRI*, Vol. 53, No. 4, pp. 235-240, 2012.

[3] Nakai, K., Suzuki, D., Enami, S., Okino, T., Takano, J. and Palacin, R., "An Estimation of Behaviour and Severity of Injury to Rail Passengers Occupying Longitudinal Seats in the Event of Collision," *Proceedings of IRCOBI Conference 2015*, pp. 315-326, 2015.

[4] Suzuki, D., Nakai, K., Enami, S. and Palacin, R., "A Countermeasure to Reduce Secondary Impact Velocity and Rib Deflection Criterion of Longitudinal-Seat Passengers in Railway Collisions," *Proceedings of IRCOBI Conference 2017*, pp. 296-297, 2017.

[5] Ministry of Land, Infrastructure, Transport and Tourism, "The new safety standard of the road transport vehicle," pp. 769-811, 2009 (in Japanese).

[6] Okino, T., Yamamoto, M., Takano, J. and Ujita, Y., "Crashworthiness evaluation for train carbody in the event of level crossing accident by driver's injury indexes," *Proceedings of the 19th Jointed Railway Technology Symposium*, No. 12-79, pp. 557-560, 2012 (in Japanese).

[7] Okino, T., Sato, H. and Kobayashi, H., "Numerical evaluation of impact deformation behavior of railway carbody in the event of level crossing accident," *Proceedings of M and M*, OS0430, 2017 (in Japanese).

[8] Nakai, K., Enami, S., "Experimental validation of effect on reducing the severity of injury to rail passengers occupying longitudinal seats using handrails in the event of collision," *Transactions of the JSME*, Vol. 85, No. 878, 2019 (in Japanese).

Authors

Kazuma NAKAI, Dr.Eng.
Senior Researcher, Ergonomics Laboratory, Human Science Division
Research Areas: Crashworthiness, Human dynamics, Ergonomics

Shota ENAMI
Assistant Senior Researcher, Ergonomics Laboratory, Human Science Division
Research Areas: Crashworthiness, Ergonomics

Numerical Analysis Method for Corrosion of Segment Joints in Shield Tunnels Caused by Chloride Attack

Kaho KINOSHITA
Tunnel Engineering Laboratory, Structures Technology Division

Takashi USHIDA
Foundation & Geotechnical Engineering Laboratory, Structures Technology Division

Deterioration caused by chloride ions may occur in some shield tunnels located in waterfront areas or near tidal rivers. In this paper, we propose a three-dimensional finite element analysis method for the maintenance of shield tunnels affected by chloride ions. In proposing this method, we developed a modeling method for deteriorated segment joints by reducing stiffness. In addition, we verified the validity of the method by loading tests of segmental lining specimens.

Key words**:** *shield tunnel, segment joint, chloride attack, corrosion, loading test numerical analysis*

1. Introduction

In recent years, there have been cases of steel corrosion in RC segments of shield tunnels located in waterfront areas or near tidal rivers. This corrosion is caused by water leakage containing chloride ions. The presence of chloride ions leads to steel corrosion in the concrete, resulting in cracking, spalling, delamination, and a reduction in the cross-sectional area of the steel. Consequently, the performance of the tunnels is compromised. Deterioration caused by chloride ions is a significant issue in maintenance and management because it often progresses rapidly once it becomes apparent, and effective countermeasures are often limited [1].

In addition, water leakage in shield tunnels tends to occur in joints, where the joint steel is exposed to a highly corrosive environment. Many studies have been conducted on the steel corrosion of RC segments in salt-affected environments and on the behavior of chloride ions in concrete. However, few studies [2] have examined the effects of deterioration caused by chloride ions on the mechanical behavior of segmental joints.

Shield tunnels consist of numerous joints, and the stiffness of these joints is smaller than that of the concrete sections in the main body. Therefore, if the stiffness of the joints decreases due to corrosion of the joint steel, it can affect the mechanical behavior of the tunnel lining. To ensure proper maintenance and management of shield tunnels in salt-affected environments in the future, it is necessary to understand the deterioration of joints and the associated mechanical behavior and develop analytical methods that account for these effects.

This paper proposes a modeling method of segment joints for 3D finite element analysis that can consider the effects of deterioration caused by chloride ions. The proposed method is based on the results of accelerated corrosion tests [3] conducted on specimens simulating joints. The validity of the proposed modeling method is verified using the results of loading experiments. The proposed method applies to bolt-type joints, broadly used in railway shield tunnels.

2. 3D FEM of shield tunnel

2.1 Summary of the proposed method

Since having many joints is a structural feature of shield tunnels, the method of modeling the joints is important for understanding the mechanical behavior of the tunnel. In the beam-spring model commonly used in the design, joints are modeled with rotating springs, and the response values such as bending moments of segments and joints are calculated. In addition, there are instances of detailed studies on segments using 3D FEM where the segmental linings have been modeled with shell elements and the joints with spring elements [4], as well as cases where the segmental linings have been modeled with solid elements and the joints with spring elements [5].

In this study, the joint modeling method was proposed for use in the detailed design of repair and reinforcement work for shield tunnels. The outline of the method is as follows: first, the segmental linings are modeled with solid elements to understand the response of the members in three dimensions. The joints are modeled with bolt-type joints, which are broadly used in existing railway shield tunnels. In this modeling approach, the steel plate of joints is modeled with shell elements, and the bolts and anchor bars with joint springs. The effect of deterioration caused by chloride ions is then expressed by reducing the stiffness of the joint springs. The proposed method focuses on the behavior when the stress of the joint steel is smaller than the yield stress since it is generally considered that response values should remain below the yield stress of the joint steel for normal use of shield tunnels.

2.2 Modeling method of the shield tunnel

The proposed modeling method of the shield tunnel is shown in Table 1 and Fig. 1. This method is an analysis method using solid and shell elements, which is characterized by modeling the joint behavior with two types of springs.

In the proposed method, the segment bodies are modeled with solid elements, and the steel plate of joints is modeled with shell elements, referring to the previous study [4]. The boundaries between the solid and shell elements are rigidly connected as double nodes. Since the shell element has three rotational degrees of freedom which are not included in the solid element, rigid

body elements, one type of functional element, are used to constrain the shell element. The bolt boxes are modeled with finite elements whose shape matches real ones.

In addition, the joint steel was modeled with joint springs, and the interaction of concrete surfaces between segments is modeled with contact springs. The joint spring is a composite spring, modeling the joint bolt and the anchor bar. According to the accelerated corrosion test results [3] for specimens simulating joints, it was shown that chloride ions penetrated along the joint steel, and defects occurred in the anchor bar along with corrosion of the bar tip. This suggests that the corrosion of the anchor bars decreased the bond strength to the concrete and affected the mechanical behavior of the lining. For this reason, the joint springs are modeled with springs having composite springs including joint anchor bars, and installed in the bolt position.

Compression springs are used as contact springs to simulate the interaction between the concrete surfaces of the segments. These springs are modeled with springs having equivalent stiffnesses that consider the effect of cracks in the segment body and placed on the entire concrete surface of the joints, and contact springs are effective only in compression.

Table 1 Modeling method in the proposed method

Modeling object	Element type (Designation)	Remarks
Segment body	Solid element	Linear elasticity model
Steel plate of joints	Shell element	Linear elasticity model
Coupling bolt	Spring element (Joint spring)	Joint bolt and anchor bar
Joint anchor muscle		Composite spring
Interaction of concrete surfaces	Spring element※ (Contact spring)	Compression spring considering nonlinear behavior with equivalent stiffness

*In the case of the tensile condition, rigidity is set to 0.

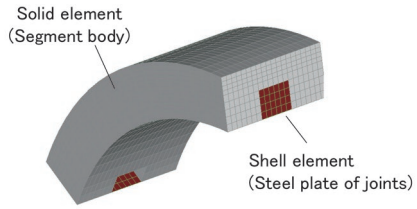

(a) Modeling of segment body and steel plate of joint

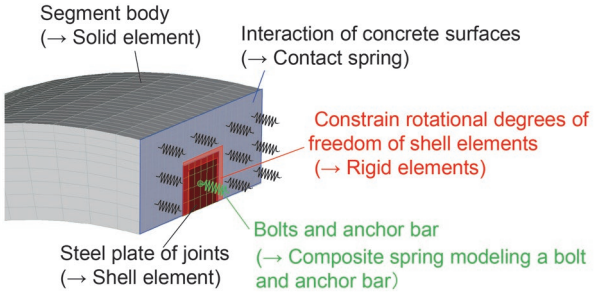

(b) Modeling of joints

Fig. 1 Shield tunnel modeling method

2.3 Modeling of joints

2.3.1 Contact springs between segments

When tunnels are loaded, reaction forces are generated by contact and compression behavior between segments. To simulate these forces, contact springs are modeled on the concrete surfaces between the segments. It was assumed that the joints show complex behaviors, including the nonlinear behavior of concrete caused by compressive and tensile stress, and contact/separation behavior caused by the discontinuity between segments, which came not only from material nonlinearities but also member and structural nonlinearities. In the proposed method, these behaviors are modeled collectively with contact springs. Then, taking the length of the contact spring as a parameter, the non-linear stiffness is calculated assuming them as springs having equivalent stiffness as the segment. The stiffness of the contact springs is calculated by (1). The length of the contact spring is discussed later in the next chapter.

$$k = \frac{E_c A}{L} \tag{1}$$

where E_c = static modulus of elasticity of concrete;
A : Cross-sectional area of concrete between segments;
L : Equivalent length of the contact spring that expresses the non-linear behavior of the segment.

2.3.2 Joint spring

In the proposed method, the steel plate of joints is modeled with shell elements, and the bolt and eight anchor bars, the other main components of the bolt-type joints, are modeled with spring elements. Since tensile and bending force occur on the anchor bars and bolts during service, their spring stiffness is defined by (2), considering the tensile behavior (Fig. 2) and bending behavior (Fig. 3) of joints.

To consider the tensile behavior, the springs are modeled with a composite spring (referred to as 'joint spring') as shown in Fig. 2, following the calculation method of the tensile spring constant of one-pass joints [6]. The calculated stiffness of this spring is used as the stiffness of the joint spring in the circumferential direction of the tunnel.

To consider the bending behavior, the joint spring stiffness in the radial direction of the tunnel is set using the joint spring stiffness in the tunnel radial direction (3), assuming that the anchor bar is a fixed-tip-cantilever beam under bending moment. This assumption was based on the deformation state of the anchor bar at the joints after the segmental lining loading tests [3]. For simplicity, the analysis does not consider any of the restraints around the anchor bar, non-linearity resulting from fracture progression of the concrete around the anchor bars, and the effect of corrosion on the bending stiffness of the anchor bar, which was confirmed to have low sensitivity in the analysis. In addition, since this analysis focuses on the behavior in the transverse direction, the joint spring stiffness is assumed to be constant in the tunnel axial direction.

The results of accelerated corrosion tests [3] on specimens simulating joints suggested that the presence of chloride ions in the concrete strongly affected the joint anchor bars. Based on these results, the effects of corrosion on joint steel materials such as anchor bars and joint bolts are considered by multiplying the joint spring stiffness in the tunnel circumferential direction (k_2) by the spring reduction factor α.

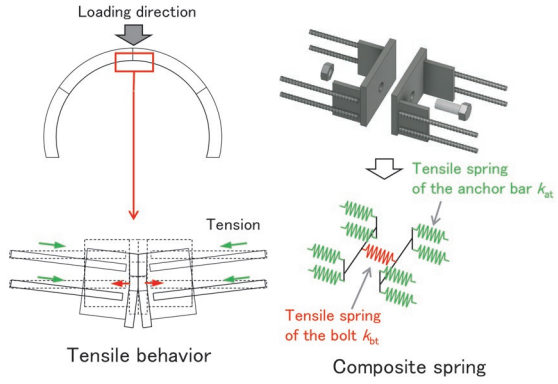

Fig. 2 Tensile behavior of bolts and anchor bars

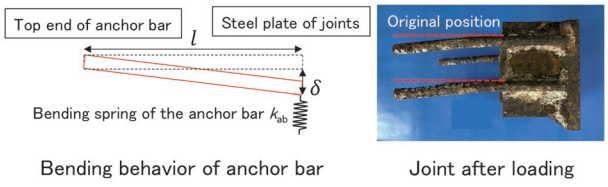

Fig. 3 Bending behavior of anchor bar

$$[k_1, k_2, k_3] = \left[8k_{ab}, \frac{k_{at}k_{bt}}{k_{at} + 2k_{bt}}, 8k_{ab} \right] \quad (2)$$

where k_1 : joint spring stiffness in tunnel radial direction;
k_2 : joint spring stiffness in tunnel circumferential direction;
k_3 : joint spring stiffness in the direction of tunnel depth;
k_{ab} : spring stiffness due to bending of one joint anchor bar. According to (3) (8 anchor bars per joint),

$$k_{ab} = \frac{3E_s I}{l^3} \quad (3)$$

k_{at} : tensile spring stiffness of joint anchor bar;
k_{bt} : tensile spring stiffness of the joint bolt;
α : spring reduction factor due to corrosion (α = 0 to 1.0);
E_s : static modulus of elasticity of anchor bars;
I : sectional secondary moment of anchor bar.

3. Validation of the proposed method by loading tests of segmental lining specimens

3.1 Summary

We verified the validity of the proposed analysis method through loading tests of segmental linings [3]. The purpose of the tests was to understand the joint behavior of the segmental lining at load levels below the yield stress. Currently, railway shield tunnels have been designed using the allowable stress design method. Therefore, the validation of the analytical method was conducted in the range of less than 10 mm vertical displacement of the loading plate, where the stresses that occurred on the segmental linings were below allowable stresses.

3.2 Loading tests of segmental lining specimens

The verification of the proposed method was conducted through a loading test using the large-scale model tunnel lining test unit [7] shown in Fig. 4. In the loading tests, all reaction springs were activated to simulate ground reaction forces. The loads were applied vertically downwards to the segmental linings using the loading hydraulic jacks installed at the crown of the testing unit. The segmental linings were assembled by joining four segmental specimens shown in Fig. 5 with the bolt-type joints shown in Fig. 6. The following three lining specimens were fabricated: the lining specimen deteriorated by chloride ions (referred to as the deteriorated lining), the lining specimen with loss of bond between concrete and anchor bars (referred to as the unbonded lining), and the sound lining specimen (referred to as the sound lining).

The deteriorated lining was subjected to accelerate corrosion of segment specimens conducted before the loading test. Then, those specimens were set at the crown of the segmental lining [3] because the joint at the crown was considered to rotate the most during the loading tests. The segment specimens were connected with M20 bolts. It was noted that to maintain the required strength for connection, the bolts were excluded from the accelerated corrosion test.

The unbonded lining was made based on the result of the accelerated corrosion test [3], by changing the anchor bar from D10 to φ8 round steel (SR-24) for the bolt-type joints and by bonding butyl rubber tape to the anchor bar, before casting the mortar to remove the bond between anchor bar and mortar.

The sound lining was fabricated for comparison with the other lining specimens.

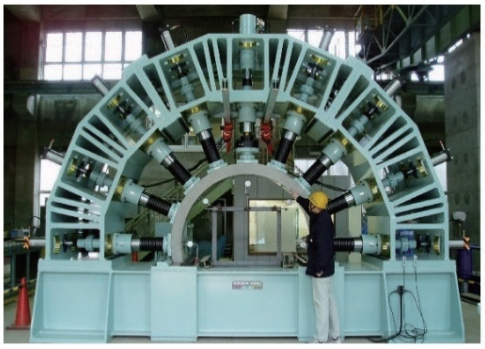

Fig. 4 Large-scale model tunnel lining testing unit

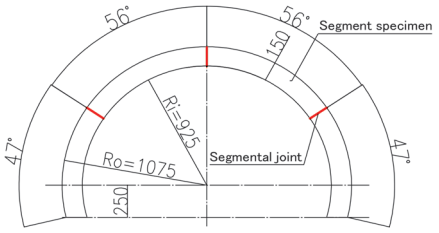

Fig. 5 Segmental lining specimen

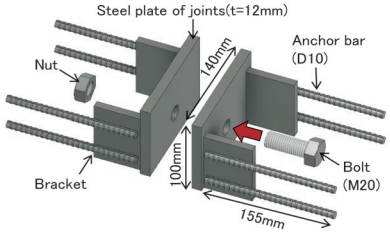

Fig. 6 The bolt-type joint

3.3 Analysis conditions

The finite element model used in the analysis is shown in Fig. 7. The segment bodies are modeled with 8-node solid elements, and the steel plate of the bolt-type joint is modeled with 4-node shell elements. Rigid elements are modeled at the boundary between the solid and shell elements. The FEM model comprises 14,702 nodes and 11,736 elements.

The boundary conditions of this analysis are shown in Fig. 8. For the bottom of the segmental lining specimen, the nodes at the end of the ground side are fixed in both the vertical and horizontal directions, while the other nodes are fixed in the vertical downward direction. The reaction plates of the testing unit, which simulate the interaction with the ground, are modeled with ground springs, and the coefficient of subgrade reaction is assumed to be 16 MN/m^3 based on the previous study [8].

Table 2 shows the physical properties used in this analysis. In this analysis, the length of the contact spring (L) is defined as the range of compressive stress that occurred on the ground side near the crown, and the same value is applied to all joints. This is due to the following reasons. First, because the crown of the segmental lining model is loaded in the vertically downward direction, the behavior of the joints at the crown is considered to significantly affect the behavior of the linings. Second, because the contact spring is used to represent the compression and contact behavior between segments, and the joint at the crown is bent to generate compressive stresses on the ground side.

Specifically, according to the result of the previous beam-spring analyses [9] shown in Fig. 9, since the range where compressive stress occurs with increasing load converged to a constant value, the convergence value of the circumference length of the positive bending section near the crown is defined as the length (L) of the contact spring. In the loading tests, it was observed that the slope of the load-displacement curve did not change due to cracking at the displacement level at which the cracking of the concrete occurred. Therefore, the length of the contact spring (L) is determined based on a linear beam-spring analysis.

For obtaining the spring reduction factor α due to corrosion, two cases were conducted: $\alpha = 1$ for the sound lining and $\alpha = 0$ for the unbonded lining. In order to take into account the change in spring stiffness as the loading progresses, step analyses were used in which load increments were given.

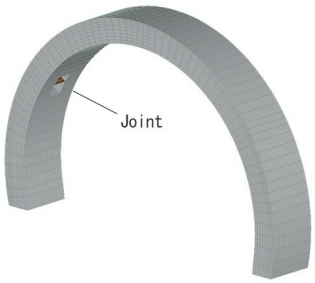

Fig. 7 Finite element model

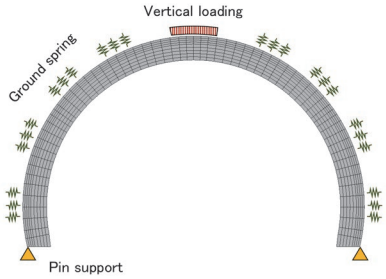

Fig. 8 Boundary conditions

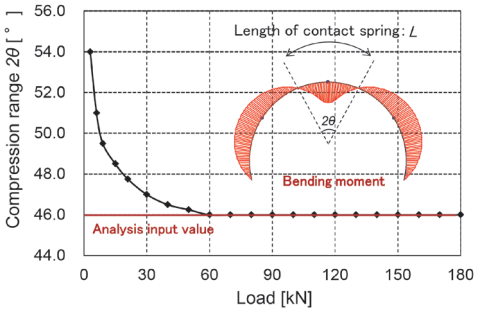

Fig. 9 Compression range estimated by beam-spring analysis

Table 2 Physical properties used in the analysis

Component	Item	Value
Segment body	Static modulus of elasticity E_c*	22.5 kN/mm^2
	Poisson's ratio ν_c	0.2
	Unit volume weight γ_c*	24.5 kN/m^3
The steel plate of joints	Static modulus of elasticity E_s	200 kN/mm^2
	Poisson's ratio ν_s	0.3
	Unit volume weight γ_s	77.0 kN/m^3
Joint spring	Radial direction stiffness k_1	1.9 kN/mm
	Circumferential direction stiffness k_2	379.5 kN/mm
	Depth direction stiffness k_3	1.9 kN/mm
	Spring reduction factor α	1 (sound) 0 (loss of bond)
Contact spring	Circumferential direction stiffness	0.03 kN/mm

* Experimental value

3.4 Analysis Result

3.4.1 Load-displacement

The load-displacement curves at the crown of the lining specimens obtained from model tests and analyses are shown in Fig. 10. In the range of 10 mm vertical displacement of the loading plate, the case with no reduction in spring stiffness (spring reduction factor $\alpha = 1$) accurately represented the test results for the sound lining. The results indicated the validity of the proposed method, in which the segment bodies were modeled with a linear elastic body, and the effects of nonlinearity were modeled with contact springs between segments.

Also, the case where the spring stiffness was reduced (spring reduction factor $\alpha = 0$), approximately represented the test results for the unbonded lining. However, the discrepancy emerged after a 10 mm displacement. When considering for the loss of bond between concrete and reinforcement, the degree of reduction in stiffness relative to the sound lining was greater in the analysis than in the model test. This result may arise from the assumption made in the analysis that the bond was entirely lost, while in the test, the residual resistance force remained due to the bond of the bracket and other factors. This result indicated the validity of the proposed

method within the targeted deformation range.

3.4.2 Opening of joints and stress distribution

Figure 11 shows the vertical displacements and von Mises stresses for two cases: $\alpha = 1$, assuming the sound lining, and $\alpha = 0$, assuming the unbonded lining. The $\alpha = 0$ case indicated a vertical displacement larger than the $\alpha = 1$ case due to the reduction of rotational stiffness of the joints. Consequently, the vertical displacement at the crown was correspondingly larger in the $\alpha = 0$ case. The opening of joints for the unbonded lining was approximately 2.8 mm larger than the $\alpha = 1$ case, which was qualitatively consistent with the test results. The analysis results showed a larger amount of opening of joints compared to the model test. This difference could be due to the concentration of resistance forces of the anchor bars and the bolts in the joint springs at the bolt position and the assumption made in the analysis of a complete loss in bond, as mentioned above.

Elements of which the von Mises stresses exceed the shear strength (6 N/mm^2) were colored in Fig. 11 as the expected damage range. Where the shear strength was assumed to be equivalent to 1/5 of the compressive strength (30 N/mm^2) of the concrete used in the model tests. In the case of $\alpha = 1$, the areas of high von Mises stress were concentrated inside the bolt box and around the joints. In the previous loading tests [3], cracks were observed at the same locations, which were in general agreement with the analytical results.

In the case of $\alpha = 0$, the stress concentration near the joints at the crown was not observed. The stress around the joints decreased due to the reduction of the stiffness of joint springs and the increase of the opening of joints. This result showed that the results were qualitatively consistent with the bending moment distribution obtained from the loading tests and the cracking state of the lining specimens [3]. This suggests that the proposed method can be valuable in understanding the response of a lining with changed joint characteristics.

3.5 Study on Case of Lining Deteriorated by chloride ions

This section presents an example of the procedure to estimate the state of deterioration of lining by chloride ions using the proposed method, through parametric analyses. The relationship between the spring reduction factor α and the slope of the load-displacement curve (referred to as the stiffness of the lining) derived from parametric analyses is shown in Fig. 12. The figure also shows the initial lining stiffness for each test case. In the case of deteriorated lining, the segment specimens were corroded assuming the accelerated stage of deterioration. Pitting corrosion was visually observed on the joint anchor bars of this lining [3], and it was expected that the bond properties would deteriorate significantly. The lining stiffness in the FEM was about $\alpha = 0.14$, which was consistent with the test, and it was estimated that the spring reduction factor of the bond properties was small. Under the conditions of this study, it was observed that the reduction in lining stiffness tended to be large when the spring reduction factor was below approximately $\alpha = 0.2$.

4. Conclusion

This study proposes a numerical analysis method for shield tunnels that is able to consider the effect of corrosion on joint steel. The proposed method is intended to be used for the detailed design of repair and reinforcement works in the maintenance and management of shield tunnels deteriorated by chloride ions in waterfront areas or near tidal rivers. In the proposed method, the contact between segments and the compression of concrete is modeled with contact springs. In addition, the joint steel, except for the steel plate of the joints, are modeled with joint springs, and the effect of corrosion is taken into account by reducing the spring stiffness. The proposed method was applied to the analysis of the loading test of the lining specimens, and consistent results were obtained in terms of load-displacement, opening of joints, and stress distribution.

In the future, we plan to examine the method in actual tunnels

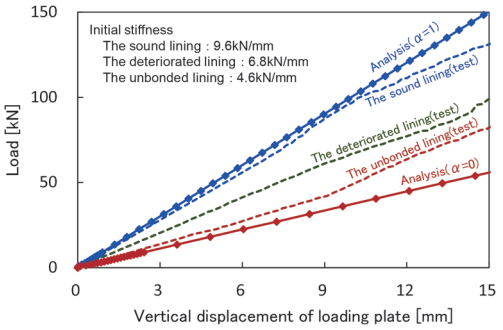

Fig. 10 Comparison of load-displacement curves

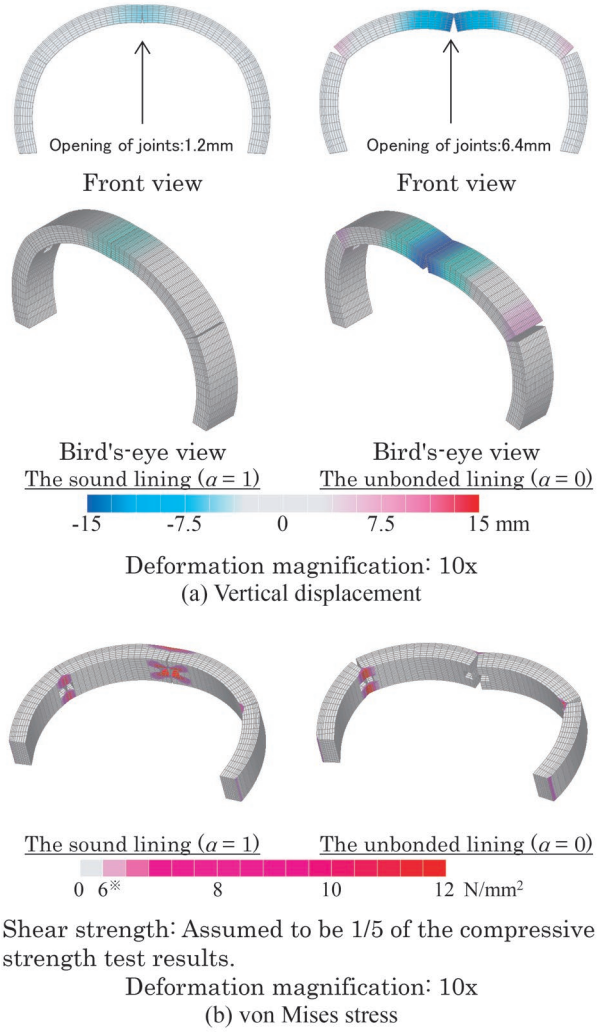

Fig. 11 Analysis results (Loading with 54 kN)

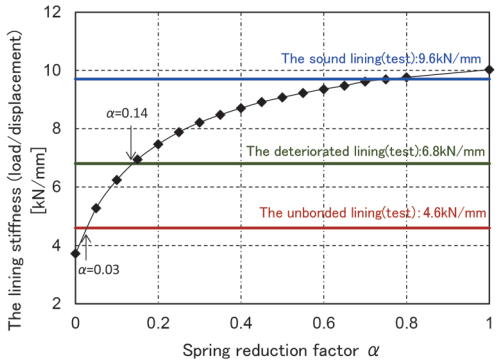

* Initial lining stiffness (5 to 10 mm load plate displacement) is described for the test.

Fig. 12 Relationship between lining stiffness and spring reduction factor

and to further develop the method by organizing the relationship between the data obtained from visual inspections and the state of corrosion of the joints.

References

[1] Japan Society of Civil Engineers, *Standard Specifications for Concrete Structures [maintenance part],* 2018 (in Japanese).

[2] Enya, Y., Anan, K., Ootsuka, M. and Koizumi, A., "Study of maintenance of shield tunnel for underground transmission," *Journal of JSCE F1,* Vol. 67, No. 2, pp. 108-125, 2011 (in Japanese).

[3] Kinoshita, K., Ushida, T., Tsuno, K. and Hosoda, A., "Finite element analysis method for shield tunnel considering influence of corrosion of segment joint," *Journal of JSCE F1,* Vol. 78, No. 1, pp. 88-101, November 2022 (in Japanese).

[4] Ishimura, T., Mashimo, H. and Morimoto, S., "A study on shield tunnel construction loads using a three-dimensional shell model," *Proceedings of tunnel engineering of JSCE,* Vol. 22, pp. 303-308, 2012 (in Japanese).

[5] Koyama, Y., Okano, N. and Shimizu, M., "3-dimensional FEM analysis of segment joint in shield tunnel," *Proceedings of tunnel engineering of JSCE,* Vol. 5, pp. 397-402, 1995 (in Japanese).

[6] Japan Shield Segment Engineer's Association, *Cone connecter segment one-pass joint,* 2014 (in Japanese).

[7] Takahashi, M., Tsuno, K. and Kojima, Y., "Development of testing machine with a large tunnel lining model," *Abstract of 2006 JSCE annual meeting,* III, pp. 139-140, 2006 (in Japanese).

[8] Yashiro, K., Kojima, Y., Arai, Y., Okano, N. and Takemura, J., "A study on numerical simulation method for plain concrete tunnel lining considering softening due to compression failure," *Journal of JSCE C,* Vol. 65, No. 4, pp. 1024-1038, December 2009 (in Japanese).

[9] Kinoshita, K., Tsuno, K., and Ushida, T., "A study on numerical analysis method for segmental lining," *Abstract of 2019 JSCE annual meeting,* III-26, 2019 (in Japanese).

Authors

Kaho KINOSHITA
Researcher, Tunnel Engineering Laboratory,
Structures Technology Division
Research Areas: Urban Tunnel

Takashi USHIDA, Dr.Eng.
Senior Researcher, Foundation &
Geotechnical Engineering Laboratory,
Structures Technology Division
Research Areas: Urban Tunnel

Effects of Impact Loads from Train Wheel Passing Rail Joints on Fatigue at Deck System of Steel Box Girder

Yusuke KOBAYASHI
Steel and Hybrid Structures Laboratory, Structures Technology Division

Taro INOUE
Steel and Hybrid Structures Laboratory, Structures Technology Division (Former)

Impact loads from train wheels passing rail joints tend to cause fatigue cracks in steel bridges near the rail joints. In order to evaluate the effects of impact load on the fatigue of the deck system of a steel box girder, we carried out stress measurements on steel girders on an existing bridge. The results showed that the impact loads at rail joints generate two types of high frequency natural mode vibrations of around 40 Hz, and around 350 Hz. It was also shown that these vibrations lead to an increase in the range and cycle of stress at the welded joints of the deck system.

***Key words*:** *impact load, rail joint, fatigue, steel box girder*

1. Introduction

Rail joints (Fig. 1) are one of the factors that accelerate the initiation of fatigue cracks in steel railway bridges [1]. This is because the impact load at the rail joint when train wheels pass on it excites vibrations in the whole bridge and in the local area of the bridge member, and in fact, many fatigue cracks have occurred due to impact loads at the rail joints. Replacing rails on bridges with long rails is an effective countermeasure against fatigue cracks caused by the impact because rail joints are eliminated. However, for existing steel bridges, this is often difficult from a cost-effectiveness point of view, as the long rail may require reinforcement of the bridge bearings and piers to resist the increased longitudinal load due to the long rail.

Since the impact load at rail joints is due to the interaction between the rails and the wheels of the train, the influence of impact is considered to be particularly high in bridge members which directly support the tracks. An example of a track-supporting member is a deck system such as transvers ribs of a steel box girder. On the other hand, since the inside of a box girder cannot be visually observed from above or below the girder, it is difficult to check for fatigue crack initiation during daily inspection. Therefore, it is important to clarify the members which are easily excited by vibration due to the impact load at the rail joints, the degree and extent of influence of the impact load at rail joints, in order to improve the inspection accuracy of the steel box girders.

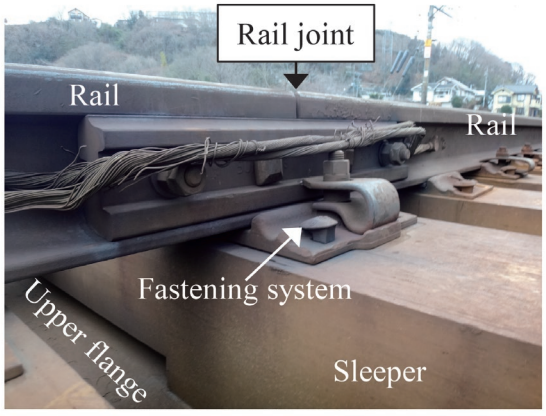

Fig. 1 Rail joint on the bridge

In this study, vibration-induced members and their vibration modes due to impact load at rail joints were estimated for longitudinal and transverse rib intersections in a steel box girder deck system, and their effects on fatigue were evaluated [2]. The effects of several factors such as train speed and distance from the rail joint on the stresses induced by the impact at the rail joint were also evaluated [2].

2. Outline of evaluation

The effects of impact load at rail joints were evaluated by stress measurements on a real bridge. In addition, the results of eigenvalue analysis were also used to estimate the members and their modes of vibration excitation due to the impact load. This chapter outlines those evaluations.

2.1 Target bridge

The target bridge is located on a conventional railway line and was constructed in the 1965s. The structure of the rail joint is shown in Fig. 1, and the track structure is of the bridge sleeper type. The rail joints are supported directly on the sleepers via a fastening system and rail pads. A side view, plan and cross section of the bridge are shown in Fig. 2.

The structural type of the target bridge is a 3-continuous deck girder with box section supporting a single track, and the height and width of the box section are 2,600 mm and 2,000 mm respectively. The upper flange has transverse ribs at an interval of 1.4 to 1.8 m in the longitudinal direction. In this study, the stress of the transverse ribs was measured as shown in Fig. 2 (c).

2.2 Target welded joint

Figure 3 (a) shows the detail of the welded joint of the transverse and longitudinal rib intersection. The transverse and longitudinal ribs are made of flat steel plate, with a plate thickness of 12 mm and 14 mm, respectively. The transverse ribs did not have a bottom flange and were slit to allow the longitudinal ribs to penetrate. The transverse and longitudinal ribs were joined by fillet

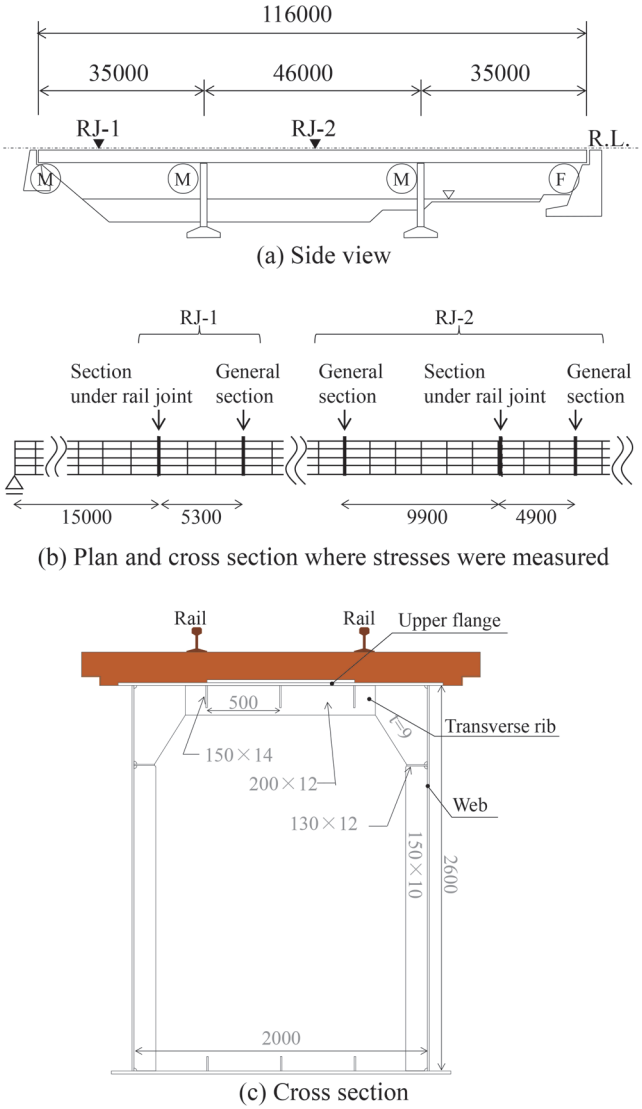

Fig. 2 Target Bridge (Unit: mm)

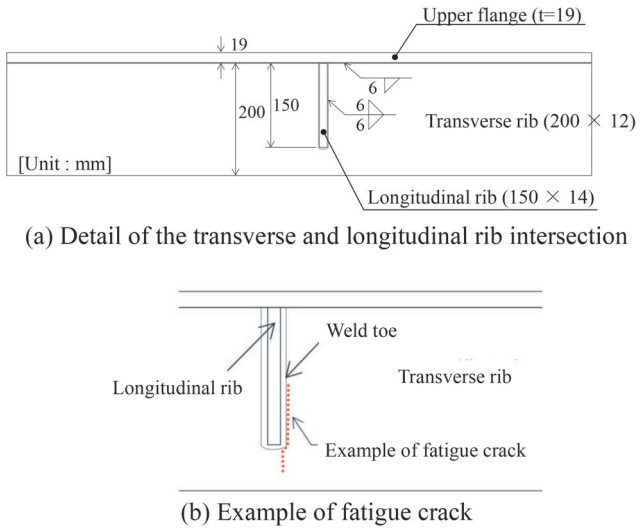

Fig. 3 Detail of transverse and longitudinal rib intersection and example of fatigue crack

welding, and there were no scallops on the upper and lower portions of the slit on the transverse rib. Fatigue cracks were observed at some of the transverse and longitudinal rib intersections near the rail joints. Those cracks initiated from the weld toe at the lower end of the intersection and propagated in the vertical direction, as shown in Fig. 3 (b).

2.3 Stress measurements

Stress measurements on the target bridge were conducted at the cross sections [RJ-1] and [RJ-2] which consist of the section directly under the rail joint, and the general sections approximately 5 to 10 m away from the rail joint, as shown in Fig. 2 (b). Figure 4 shows the location of measured stress for the transverse and longitudinal rib intersection. The horizontal direction of the stress at the intersection was measured on the transverse rib because the crack propagates in the vertical direction, and the sampling frequency of the measurement was set to 1 kHz.

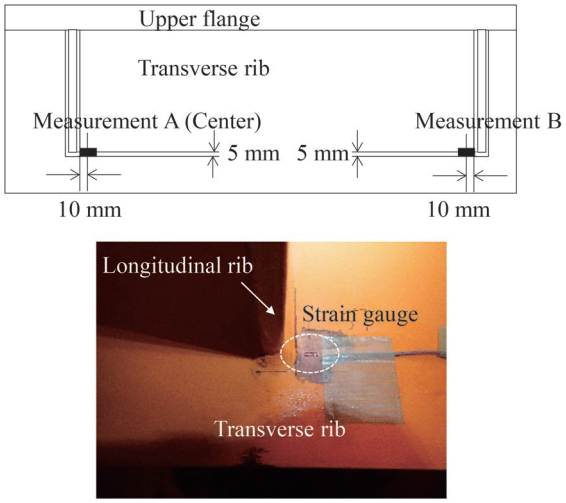

Fig. 4 Location of stress measurement

2.4 Eigenvalue analysis

An eigenvalue analysis was conducted to estimate the members and their modes of vibration excitation due to the impact load at the rail joint. Figure 5 shows the analytical model. NX Nastran was used as the analysis code and Femap 11.4.0 as the pre-post processor for the eigenvalue analysis. Only the side span of the target bridge was mathematically modeled, and in this model the boundary condition was simple support, and the 4-node shell elements were basically used, and 2-node beam elements were used for some beam members such as a sway bracing. The element division is shown in Fig. 5, with 38266 nodes and 38880 elements. The track, including rails and sleepers, is not modeled, and the weight of the vehicle is not considered.

3. Stresses at transverse and longitudinal rib intersections and their causes

This chapter presents the results of the stresses induced at the transverse and longitudinal rib intersections near the rail joints by the moving loads of the train wheels, and the results of the estimation of the deformation modes responsible for the generation of each

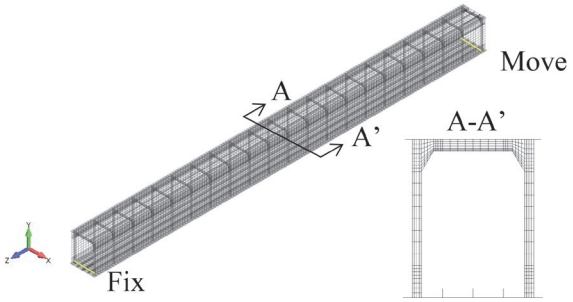

Fig. 5 Model in Eigenvalue analysis

component of stress, by comparing the stresses at the section near the rail joint with the general section without a rail joint.

3.1 Measured stress

Figure 6 shows the stress history at the intersection of the longitudinal and transverse ribs (measurement A shown in Fig. 4) at the rail joint section and the general section of RJ-1 when a train (12 cars) passes, and Fig. 7 shows the enlarged stress history of Fig. 6 when two bogies pass. Figure 6 and Fig. 7 show that the stresses at the section under the rail joint and the general section occur several times during the passage of a train, and the number of stress peaks is the same as the number of bogies (24 bogies). In other words, the stress is considered to be amplified each time a bogie passes through each section.

The stress at the section under the rail joint appears to have a high-frequency component superimposed on the stress of each bogie. The high-frequency component occurs twice in each wave of the bogie stress, and the number of peaks and peak intervals are consistent with the number of axles (48 axles) and the axle distance (2.1 m), respectively. Therefore, the high-frequency component is considered to be caused by the impact load at the rail joint, since the high-frequency component occurs at each axle, and can only be seen at the section under the rail joint.

3.2 Vibration excited by impact load at rail joint for each axle

We estimated the vibration member and the vibration mode excited by the impact load at the rail joint for each axle.

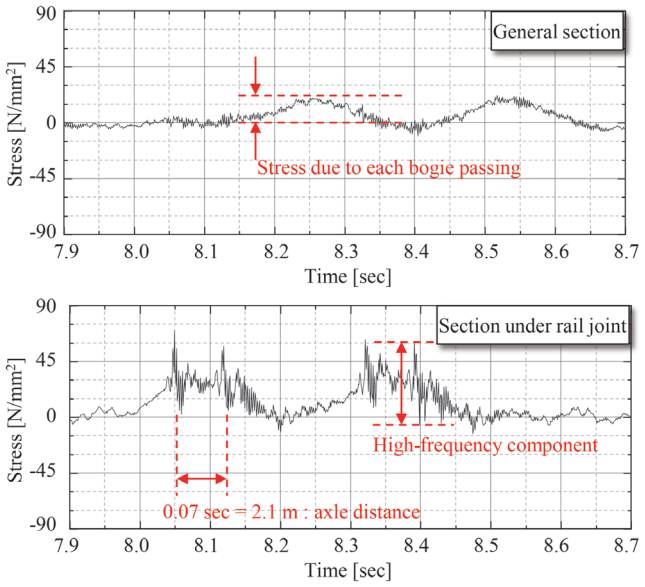

Fig. 7 Stress history of 2 bogie passing

3.2.1 Frequency of stress excited by impact load

Figure 8 shows the Fourier spectrum obtained from the stress history during the passage of a train. From Fig. 8, the dominant frequencies can be broadly classified into three components. The first is the component below 10 Hz (hereinafter referred to as component (a)), the second is the component with a peak at 44.0 Hz (hereinafter referred to as component (b)), and the third is the component with a peak at 353.8 Hz (hereinafter referred to as component (c)).

Among the above three components, component (a) is considered to be a quasi-static stress component caused by the deflection of the transverse ribs due to the passage of each bogie (hereinafter referred to as "quasi-static component") because the amplitudes of component (a) are similar in the general section and the rail joint section, and the frequency is consistent with the stress frequency generated by each bogie calculated from the train speed and bogie-to-bogie distance. On the other hand, components (b) and (c) have small amplitudes in the general section and relatively large amplitudes in the rail joint section, suggesting that they are predom-

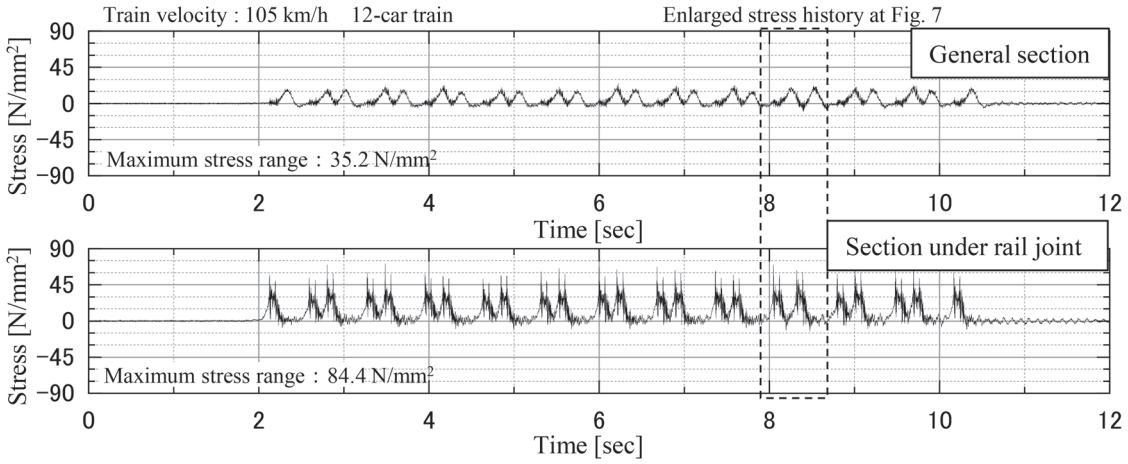

Fig. 6 Stress measured at point A shown in Fig. 4

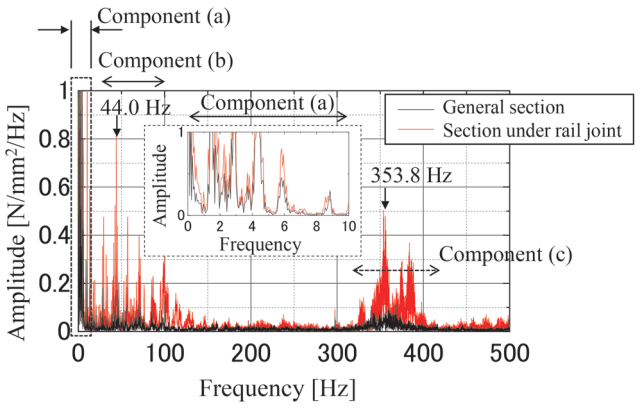

Fig. 8 Fourier spectrum of stresses at the passage of one train

inant stress components due to the vibration excited by the impact load at the rail joint.

3.2.2 Vibration component (b)

The peak frequencies of component (b) shown in Fig. 8 were similar to the deflection vibration mode of the deck system coupled with the deformation of the box section (hereinafter referred to as vibration of the box section), which was obtained from the eigenvalue analysis shown in Fig. 9. Therefore, the main vibration that generates the component (b), which is excited by the impact load at the rail joint, is presumed to be the vibration of the box section. The reason for the relatively large number of spectral peaks in the vibration component of the box section can be attributed to the existence of multiple natural vibration modes in a relatively narrow frequency band, which are different deformation orders of the web panel and deformation areas of the deck system in the longitudinal direction, as shown in Fig. 10.

3.2.3 Vibration component (c)

Component (c) shown in Fig. 8 is significantly higher in frequency than the general natural frequency of the vibration mode of the entire structural system of a steel bridge, and is therefore inferred to be caused by the vibration of the local bridge member. Assuming that the member excited by this high-frequency vibration is a transverse rib, the natural frequency of the out-of-plane vibration mode was calculated using the following equation, considering the transverse rib as a rectangular plate supported by the longitudinal rib and the upper flange.

$$f_{mn} = \frac{\pi}{2}\sqrt{\frac{d}{\rho}}\left(\frac{m^2}{a^2}+\frac{n^2}{b^2}\right) \quad (1)$$

where m and n are the vibration orders, ρ is the mass per unit area, a and b are the lengths of the long and short sides, and D is the bending stiffness of the plate.

Calculating the natural frequency from (1), the natural frequency of the out-of-plane vibration of the transverse rib is 336.5 Hz. This is approximately the same as the peak frequency of component (c) measured on the actual bridge shown in Fig. 8. The peak frequency of the actual bridge was also similar to the natural frequency of the out-of-plane vibration obtained from the eigenvalue analysis shown in Fig. 11. From these, it can be inferred that the main vibration of component (c) excited by the impact at the rail joint is the out-of-plane vibration of the transverse ribs.

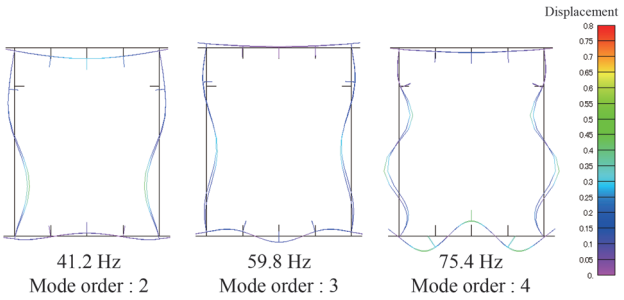

Fig. 10 Natural vibration modes of box cross section (Black line : Original shape)

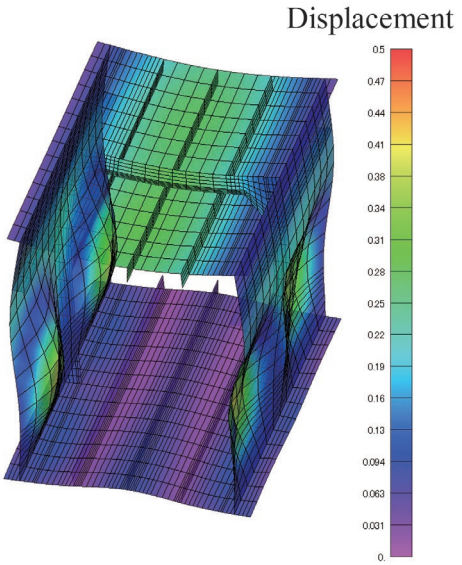

Fig. 9 Vibration mode of box section [41.2 Hz]

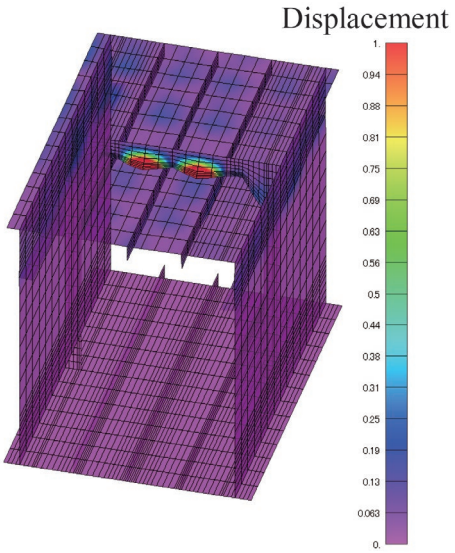

Fig. 11 Vibration mode of transvers rib [361.3 Hz]

4. Effect of impact load at rail joints on fatigue

This chapter presents the results of the evaluation of the impact load effect at rail joints on the fatigue of the box girder deck system, focusing on the vibration excited by the impact load, using the sum of the cubes of the stress range ($\Sigma\Delta\sigma^3$) (hereinafter referred to as the cumulative fatigue damage) [3] as the evaluation index. The stress range $\Delta\sigma$ included in the stress history during the passage of a train was analyzed by a rainflow method, and each vibration component excited by the impact load was extracted by filtering in the frequency domain.

Figure 12 shows the increase rate of cumulative fatigue damage at the intersection of longitudinal and transverse ribs (measurement B in Fig. 4) measured at the sections under the rail joints of RJ-1 and RJ-2 compared to the general sections. Figure 12 also shows the increase rate for each of the vibration components described in 3.2.1 to 3.2.3.

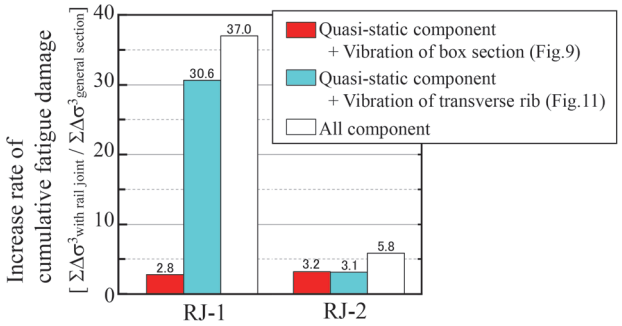

Fig. 12 Increase rate of cumulative fatigue damage

Focusing on RJ-1, the increase rate of cumulative fatigue damage of all vibration components was 37.0, which indicates that fatigue accumulates to a very large extent due to impact load at the rail joint. The increase rate of cumulative fatigue damage due to the vibration mode of the transverse ribs shown in Fig. 11 was 30.6. This indicates that the vibration component of the transverse ribs is the primary factor that significantly increased the cumulative fatigue damage due to the impact load at the rail joint.

On the other hand, focusing on RJ-2, the increase rate of cumulative fatigue damage is 5.8, which is much smaller than that of RJ-1. In other words, it can be said that the impact load effect at the rail joint on fatigue varies greatly from rail joint to rail joint. In addition, the fact that the impact load effect was small in RJ-2 was probably due to the positional relationship between the sleeper supporting the rail joints and the transverse rib, since the vibration mode component of the transverse rib was also small.

5. Factors affecting impact load at rail joint

Factors affecting the stress caused by impact load at the rail joint were evaluated, focusing on the maximum stress range at the intersection of the longitudinal and transverse ribs.

5.1 Train velocity

Figure 13 shows the relationship between the maximum stress range and train velocity at measuring points A and B in RJ-1 and RJ-2. The maximum stress range is the difference between the maximum stress and the minimum stress during the train passage. The maximum stress range at the section under the rail joint tends to increase as the train velocity increases. On the other hand, the maximum stress range in the general section increases at a smaller rate with increasing train velocity. This means that train speed has a significant effect on the impact load at rail joints.

Next, the vibration modes affected by the increase in train velocity are discussed. Figure 14 shows the relationship between the maximum stress range measured at the section under the rail joints of RJ-1 and RJ-2 and the train velocity for the box section vibration and the transverse rib vibration components. Figure 14(a) shows that the vibration component of the box section remains constant even as the train velocity increases, but Fig. 14(b) shows that the transverse rib vibration component tends to increase as the train velocity increases. In other words, the increase in train velocity easily affects the increase in the transverse rib vibration component at the intersections of the longitudinal and transverse ribs, and as a result, the maximum stress range at the intersections of the longitudinal and transverse ribs of this bridge is considered to have increased.

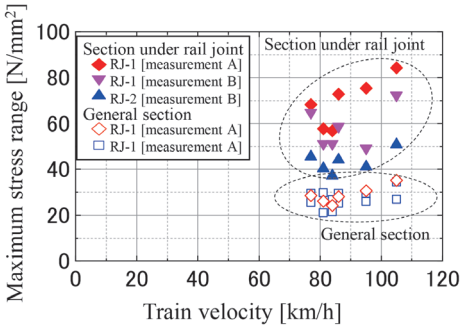

Fig. 13 Effect of train velocity

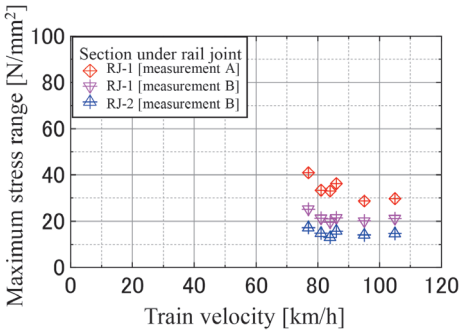

(a) Vibration component of box section

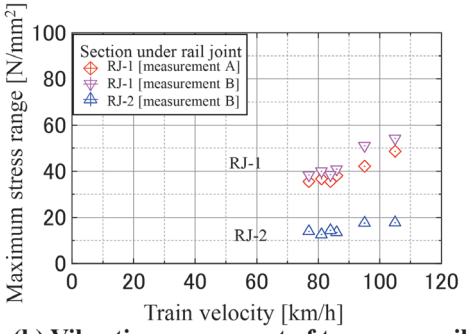

(b) Vibration component of transverse rib

Fig. 14 Effect of train velocity on vibration component

5.2 Distance from rail joint

Figure 15 shows the relationship between the maximum stress range for point A and the distance from the rail joint in the direction of the bridge axis for RJ-1 and RJ-2. The maximum stress range is greater in the section under the rail joint than in the general section, and tends to decrease with distance from the rail joint.

Next, the influence range of vibration is discussed. Figure 16 shows the maximum stress range for each vibration component. The maximum stress ranges are shown at the positions just below the rail joint, at 5 m, and at 10 m, respectively. The box-section vibration and transverse rib vibration components tend to decrease as the distance from the rail joint increases, and the rate of decrease becomes smaller when the distance from the joint exceeds 5 m. In other words, the range of influence of the impact load at the rail joints in this bridge is considered to be about 5 m.

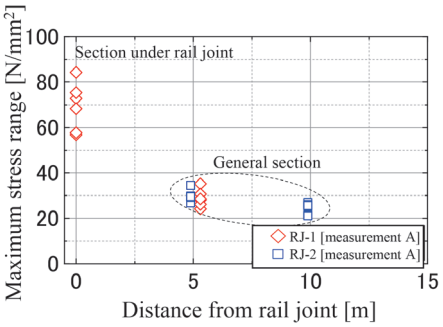

Fig. 15 Effect of distance from rail joint

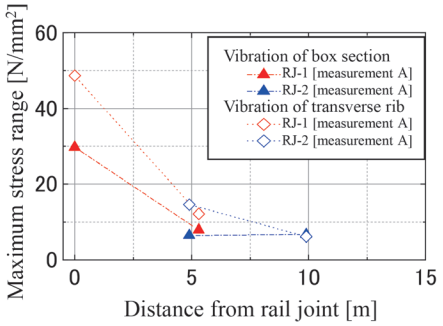

Fig. 16 Effect of distance from rail joint (vibration)

6. Conclusions

In this paper, field stress measurements were conducted on a box girder used on a conventional railway line to evaluate the effect of impacts at rail joints on the fatigue of the deck system of box girders by comparing the stress properties of the section under the rail joint and the general section. In addition, the effects of factors such as train speed, and distance from the rail joint on the stress caused by the impact load at the rail joint were also evaluated.

The following are the results obtained in this study.

(1) In the deck system of a box girder, stresses are generated by the deflection of the transverse ribs as bogies pass, but the presence of rail joints superimposes stresses caused by vibration excited by impact load.

(2) There are two main vibration modes that can be excited by impact load at rail joints: one is the out-of-plane vibration of the transverse ribs, and the other is the vibration mode in which the box section is deformed.

(3) The degree of fatigue damage at the intersection of longitudinal and transverse ribs increases up to 37.0 times in the section under the rail joint compared to the general section, and the main cause is considered to be the transverse rib vibration. In addition, the impact load of the rail joints on fatigue damage varies greatly from section to section.

(4) As train velocity increases, the effect of impact load at rail joints increases due to the excitation of vibrations in the transverse ribs.

(5) The influence of the rail joints decreased with distance from the rail joints, and on this bridge the range of influence was approximately 5 m from the rail joints.

References

[1] Kaneshima, A., Inoue, T., Kamohara, K., Matsuoka, K., Kobayashi, Y., "Influence of impact load at rail joint on stress at the top and bottom end of the stiffener of deck girder," *Journal of structural engineering*, Vol. 67A, pp. 566-577, 2021 (in Japanese).

[2] Inoue, T., Kobayashi, Y., "Effects of impact load caused by wheel passing rail joint on fatigue at the deck system of a steel box girder," *Journal of structural engineering*, Vol. 67A, pp. 555-565, 2021 (in Japanese).

[3] Japanese Society of Steel Construction, "Fatigue design recommendations for steel structures," Gihodo Shuppan Co.,Ltd., 2012 (in Japanese).

Authors

Yusuke KOBAYASHI, Dr.Eng.
Senior Chief Researcher, Head of Steel and Hybrid Structures Laboratory, Structures Technology Division
Research Areas: Bridge Engineering

Taro INOUE
Researcher, Steel and Hybridge Structures Laboratory, Structures Technology Division (Former)
Research Areas: Bridge Engineering

Prediction Equations for Shrinkage Strain of Concrete with Mixed Cement

Ken WATANABE **Mami NAKAMURA**
Concrete Structures Laboratory, Structures Technology Division

Tetsuya ISHIDA
Department of Civil Engineering, The University of Tokyo

Tadatomo WATANABE
HRC Research Institute Co., LTD (Former)

The authors developed a prediction equation for the shrinkage strain of concrete to cope with various design conditions of concrete structures. The developed equation allows input of the effects of cement types, aggregate shrinkage strain, and the application of liquid water, in addition to the conventionally indicated mix proportion of concrete and ambient relative humidity. The equation is formulated using a 3D material-structure interaction analysis system (DuCOM-COM3). The equation can explain the phenomena that is considered to be caused in part by concrete shrinkage, such as strain of concrete in prestressed concrete girders in service using blast furnace cement concrete.

***Key words*:** *concrete, shrinkage, mixed cement, aggregate shrinkage strain, DuCOM-COM3, rainfall*

1. Introduction

It is very important to reliably manage concrete bridges such as ensuring running safety of vehicles. Therefore, it is becoming increasingly important to estimate the response of bridges, which are expected to have a variety of ratio of spans, and increased span lengths, during their design service life. In addition, there are concerns that the availability of good quality aggregates will become more difficult in the future. To address this concern, there have been reports of cases in which fly ash or blast furnace slag fine powder are mixed into concrete to ensure the durability of structures, so that its effect should be considered in structural calculations [1].

The objective of this study is to develop a prediction equation for shrinkage strain of concrete used to predict long-term displacement and deformation, especially for the design of prestressed concrete (PC) bridges. In order to respond to various design conditions of concrete structures, this study presents a prediction equation that can be applied to the material properties and relative humidity of the outside air (*RH*) that have been highlighted in the past. This equation can be applied to cement mixed with fly-ash and blast furnace slag fine powder, and can introduce regional characteristics such as water exposure and shrinkage strain of aggregate while ensuring applicability to long-term age of the concrete. In this study, unreinforced concrete was analyzed using a 3D material-structure interaction analysis system (DuCOM-COM3). In the analysis system, structures of a scale that is difficult to determine based on experimental results of a few years or less were considered over the design service period of 100 years. The results of the analysis were used to formulate the equation.

2. Analysis with DuCOM-COM3

2.1 Modeling of concrete

DuCOM-COM3 integrates a material physicochemical analysis system, DuCOM, and a structural analysis system, COM3. The DuCOM models and traces the curing process of cementitious composites on the nano- to micrometer-scale, and the COM3 handles cracking and damage after steel bar yielding in reinforced concrete structures [2][3].

Figure 1 shows the analytical model using a member thickness *H* of 400 mm as an example [4]. The target model is a quarter-symmetric model with analytical symmetry planes in the X- and Y-directions. The prediction equations to be constructed are assumed to be applied to PC girders. Therefore, the boundary conditions for weather were set to be the two exposed surfaces at the top and bottom, while the other surfaces were assumed to be sealed. To ensure plane retention in the cross section, the width and depth of the analytical model were set to three times the member thickness in the direction of moisture deviation (Z-axis direction). $\varepsilon'_{cs}(t, t_0)$ is the output strain in the X-axis direction for one row of elements from the analytical symmetry plane where plane retention is approximately established in the cross section, and the average of these values was used.

2.2 Selection of influencing factors

Table 1 shows the influencing factors considered. The mineral composition ratio of ordinary Portland cement was set with refer-

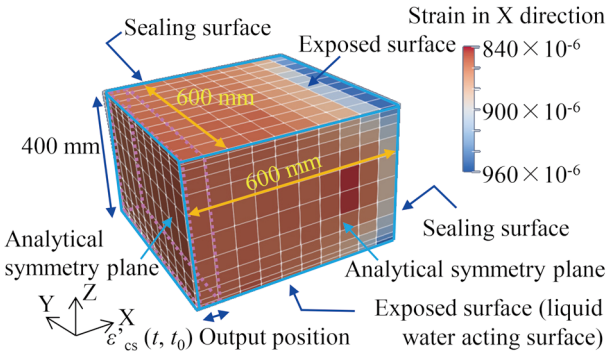

Fig. 1 Quarter-symmetry model and strain distribution in X direction (ex. *H* =400 mm)

ence to catalog values. As the physical properties of the aggregate, ε'_{ag} can be entered in the analysis. The water absorption of the aggregate was set to 1.61%.

As a characteristic of the climatic conditions in Japan, the annual average value of relative humidity was generally 60% to 80%, and the annual average monthly precipitation time was generally 1.5 to 4 days [5]. Therefore, in the analysis, the relative humidity (*RH*) acting on the two exposure surfaces was set to the same value as between 55% to 85%, which encompasses the annual average humidity. The effect of water exposure was assumed to be mainly due to precipitation, with liquid water acting on only one of the two exposed surfaces, as shown in Fig. 1.

2.3 Analytical results with dryness (t_{pre}=0 days)

Figure 2 shows the shrinkage strain $\varepsilon'_{cs}(t, t_0)$ as a result of the analysis under "always drying" conditions. Here, $\varepsilon'_{cs}(t, t_0)$ is the amount of change in strain from the beginning of drying at age t_0 to age t. Shrinkage is expressed as a positive value.

As shown in Fig. 2, $\varepsilon'_{cs}(t, t_0)$ changes over a long period of time as the member thickness H increases, and $\varepsilon'_{cs}(t, t_0)$ decreases at the end of the analysis. This will be due to the following reasons: since the central part is less affected by drying, the hydration reaction develops relatively unimpeded as H increases, and then the microstructure becomes denser, resulting in smaller drying shrinkage strain.

Near the exposed surface, the combination of external drying and self-drying due to hydration results in a significant decrease in the relative humidity h in the pores. When the H is large, the interior is less affected by external drying, so that moisture is compensated from the interior for external moisture loss and self-drying at the surface. On the other hand, when H is small, the rate of compensation by moisture absorption from the outside air has a significant effect on the decrease in H, so that $\varepsilon'_{cs}(t, t_0)$ tends to decrease, as shown in Figs. 2(c) and (f) for H = 200 mm.

At the end of the analysis, $\varepsilon'_{cs}(t, t_0)$ increases as the water-binder ratio W/B increases. This indicates that the stiffness of the concrete decreases as W/B increases, the force to control the volume change due to water loss becomes smaller, and finally the effect of water loss is more dominant than self-drying due to the increase in the unit water content in the cement paste. The increase in the unit water content in the cement paste causes the effect of water evaporation to be more dominant than self-drying. The increase in initial age-related shrinkage strain slows as W/B increases. This is because the dominant mechanism for shrinkage behavior in young lumber shifts from self-drying due to hydration to moisture loss to the open air as W/B increases.

In the case of large H, the strain tends to decrease for concrete with a low water-binder ratio (Fig. 2(a)). This is because the self-drying associated with the progress of hydration becomes more pronounced. Then, the relative humidity inside the member, which is less sensitive to environmental influences, is significantly lower than the external environment, and long-term moisture absorption causes a shift from shrinkage to swelling.

Table 1 Analysis Factors (* denotes the base case)

Influence factor		Rage of analysis
Type of cement		N*, BB, FB
W/B: water-binder ratio		0.35, 0.40, 0.50
W: unit water content	(kg/m^3)	145, 160*, 175
RH: relative humidity	(%)	55, 60, 70, 85
H: member thickness	(mm)	100, 200, 400, 600, 1000
ε'_{ag}: aggregate shrinkage strain	($\times 10^{-6}$)	0, 400, 800*, 1200
t_0: age at start of drying	(day)	1, 3, 7*, 14, 28, 90, 365
t_{pre}: Liquid Water Action Duration	(day)	0*, 1, 4, 12 (per 28 days)

N: ordinary cement, BB: blast furnace cement (45% replacement ratio), FB: fly ash cement (15% replacement ratio)

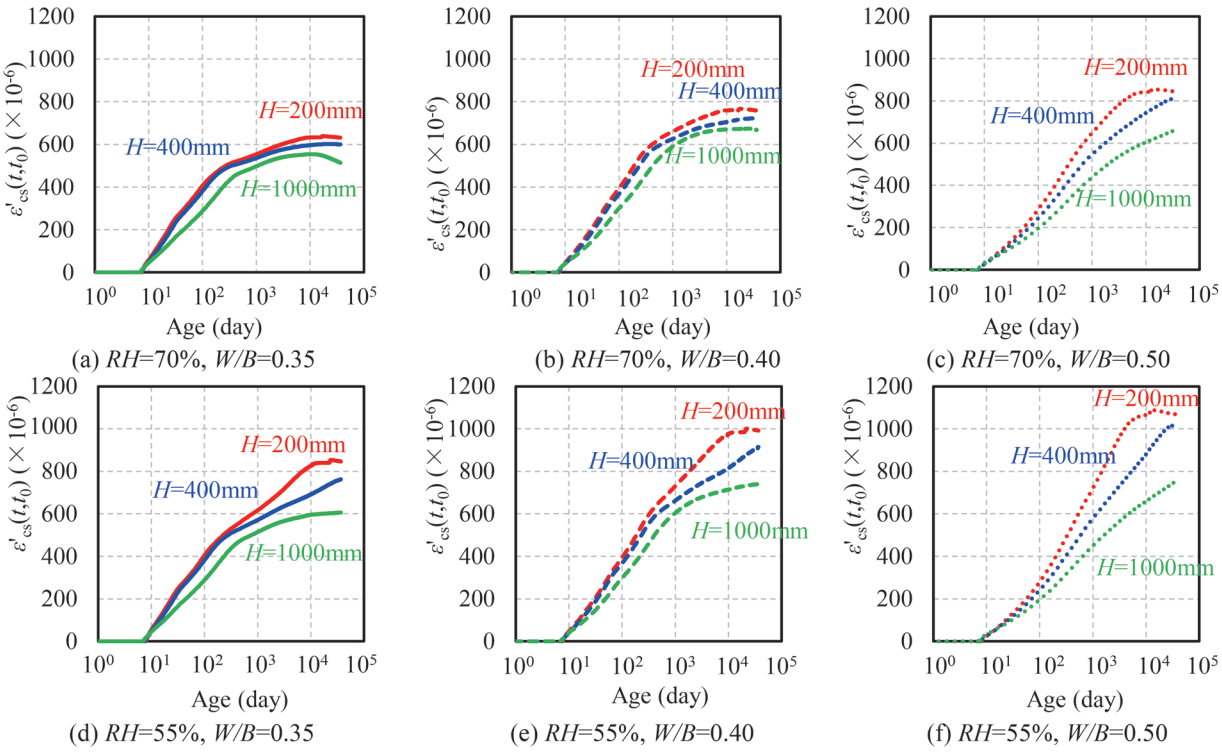

(a) *RH*=70%, *W/B*=0.35 (b) *RH*=70%, *W/B*=0.40 (c) *RH*=70%, *W/B*=0.50

(d) *RH*=55%, *W/B*=0.35 (e) *RH*=55%, *W/B*=0.40 (f) *RH*=55%, *W/B*=0.50

Fig. 2 Shrinkage strain over time (N, *W*=160 kg/m^3, t_0=7 days, always dry)

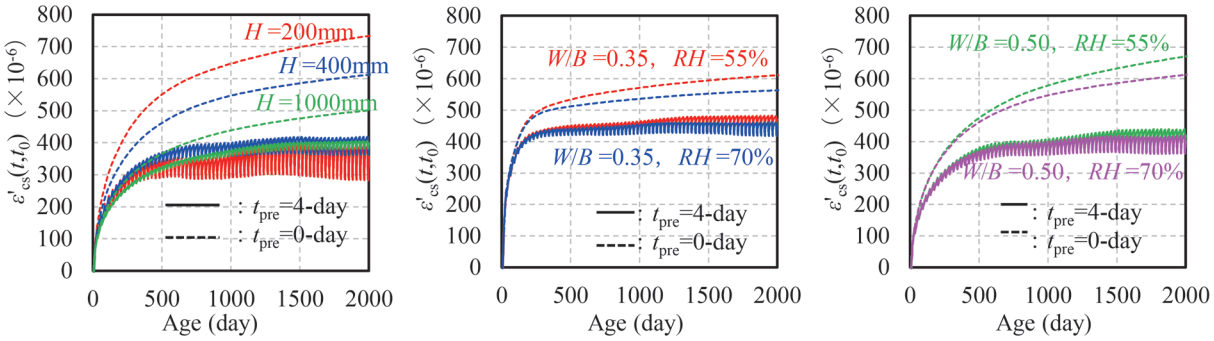

Fig. 3 Change over time of shrinkage strain under repeated wet and dry conditions

2.4 Analysis results for wet and dry cycles

Figure 3(a) shows the effect of H on the increase of $\varepsilon'_{cs}(t, t_0)$ with increasing age for concrete with t_{pre}=0 and 4 days as H decreases. This can be understood to be due to the increase in the percentage of wetted area by moisture supply relative to H, although the moisture that has penetrated by moisture supply moves into the interior.

Figure 3(b)(c) shows the effect of W/B and RH on $\varepsilon'_{cs}(t, t_0)$ of concrete with t_{pre}=0 day. It is found that $\varepsilon'_{cs}(t, t_0)$ of case W/B=0.50 is slightly larger than W/B=0.35. The pore structure becomes coarser as W/B increases, which allows moisture that has penetrated by precipitation to move easily within the member. Therefore, this is thought to be related to the relatively large area that remains wet under the influence of precipitation. The ratio of $\varepsilon'_{cs}(t, t_0)$ at t_{pre}=4 days to t_{pre}=0 days is similar for both W/B at RH=55% and 70%.

3. Development of prediction equation of shrinkage strain

3.1 Basic concept of prediction equation

The prediction equation for the shrinkage strain to be developed calculates the shrinkage strain $\varepsilon'_{cs}(t, t_0)$ that occurs from the age at the start of drying, t_0, to any age, t. Considering the construction process of the structure, the age at which curing is completed and drying begins for PC bridges differs from the age at which shrinkage begins to be considered in structural analysis, such as in the calculation of prestressing loss.

In this study, it was decided to use a hyperbolic function, which has only one term that expresses the change over time, can handle the influence of each variable comprehensively, and makes it easier to understand the structure of the prediction equation. The prediction equation for shrinkage strain using the hyperbolic function is expressed in (1).

$$\varepsilon'_{cs}(t, t_0) = \varepsilon'_{cs\infty} \times [(t-t_0)/\{\beta+(t-t_0)\}] \quad (1)$$

where $\varepsilon'_{cs}(t, t_0)$: shrinkage strain of concrete occurring from t_0 to t ($\times 10^{-6}$), $\varepsilon'_{cs\infty}$: final value of shrinkage strain ($\times 10^{-6}$), and β: term representing the aging characteristics of shrinkage strain.

3.2 Prediction equation for shrinkage strain for normal drying (t_{pre}=0 days)

3.2.1 Final value of contraction strain $\varepsilon'_{cs\infty}$

The final value of $\varepsilon'_{cs}(t, t_0)$, $\varepsilon'_{cs\infty}$, can be expressed by (2).

$$\varepsilon'_{cs\infty} = k_r \times \varepsilon'_{cs\infty k} \times g_{\infty 1}[H/H_k] \times g_{\infty 2}[(W/B)/(W/B)_k] \times g_{\infty 3}[RH/RH_k] \times g_{\infty 4}[t_0/(t_0)_k] \times g_{\infty 5}[\varepsilon'_{ag} - (\varepsilon'_{ag})_k] \quad (2)$$

where $\varepsilon'_{cs\infty k}$: standard value of final value of shrinkage strain, $g_{\infty i}[X_i/X_{ik}]$: function normalized by each parameter X_{ik}.

The parameters X_{ik} corresponding to $\varepsilon'_{cs\infty k}$ are assumed to be H_k=400 mm, $(W/B)_k$=0.50, RH=60%, $(t_0)_k$=7 days, and $(\varepsilon'_{ag})_k$=400 $\times 10^{-6}$, assuming the conditions of a typical structure.

Figure 4 shows the relationship between $g_{\infty i}[X_i/X_{ik}]$ and X_i/X_{ik} obtained from the DuCOM-COM3 analysis as the effect of each factor on $\varepsilon'_{cs\infty}$ and β. The figure also shows the predicted values by a dotted line.

Figure 4(a) shows the effect of H on $\varepsilon'_{cs\infty}$. In this case where H=100 to 1000 mm and the age of wood is 100 years, $\varepsilon'_{cs\infty}$ decreased as H increased.

Figure 4(b) shows the effect of W/B on $\varepsilon'_{cs\infty}$. For W/B=0.35 to 0.50, $\varepsilon'_{cs\infty}$ increased in proportion to $W/B^{1/2}$. It was similar for BB and slightly smaller for FB relative to concrete with N.

Figure 4(c) shows the effect of RH on $\varepsilon'_{cs\infty}$. $\varepsilon'_{cs\infty}$ increased with decreasing RH. Prediction in the figure was formulated using data from RH=55% to 70%, prioritizing prediction accuracy at standard outdoor relative humidity, but a function proportional to RH^{-1} was used to account for the results of the analysis at RH=85%.

Figure 4(d) shows the effect of age t_0 at the start of drying on $\varepsilon'_{cs\infty}$. $\varepsilon'_{cs\infty}$ decreased as t_0 increased. The later the start of drying, the lower the H at the age at the start of drying due to the hydration reaction progressing under the sealed condition before the start of drying. In addition, the densification of the microstructure reduces the rate of moisture transfer, which is thought to be due to a decrease in the amount of moisture lost to the atmosphere after the start of drying.

Figure 4(e) shows the effect of coarse aggregate shrinkage strain ε'_{ag} on $\varepsilon'_{cs\infty}$. $\varepsilon'_{cs\infty}$ increased monotonically with increasing ε'_{ag}.

3.2.2 Shrinkage strain aging characteristic β

Using the main influencing factors H and W/B, β can be expressed by (3).

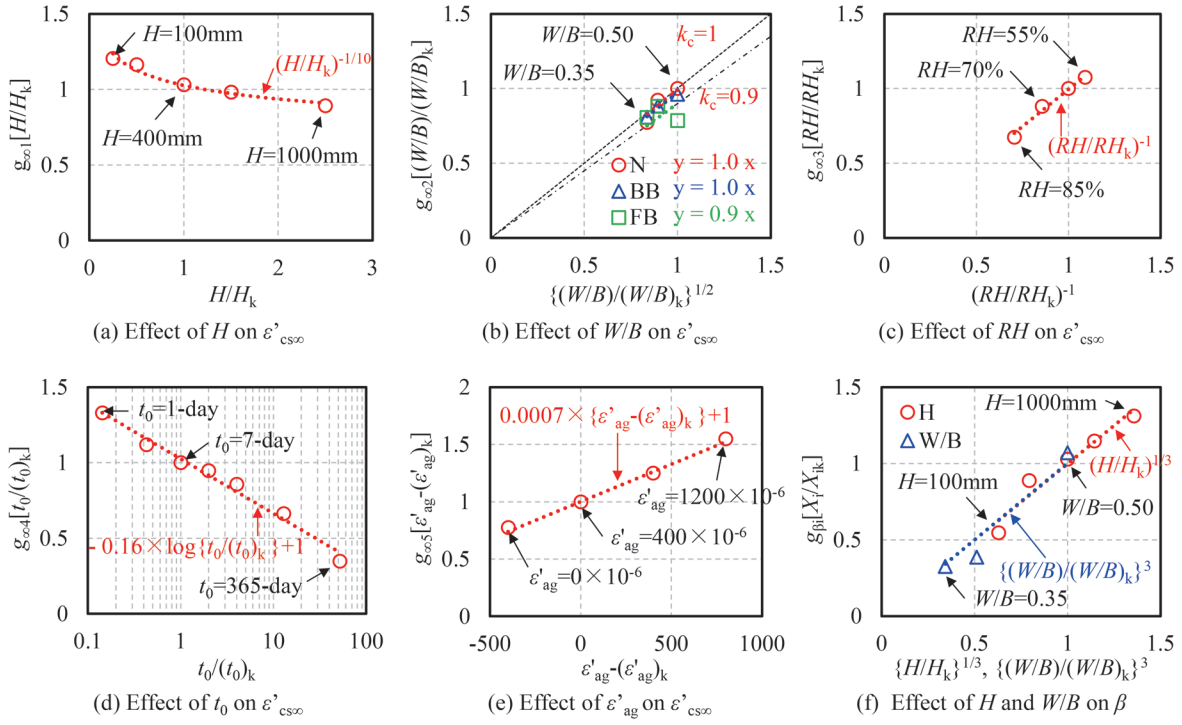

Fig. 4 Effect of each factor on $\varepsilon'_{cs\infty}$ and β

$$\beta = A_\beta \times g_{\beta 1}[H/H_k] \times g_{\beta 2}[(W/B)/(W/B)_k] \quad (3)$$

where A_β: constant (=720), $g_{\beta i}[X_i/X_{ik}]$: function normalized by each parameter X_{ik}.

Figure 4(f) shows the relationship between $g_{\beta 1}[H/H_k]$ and H/H_k, $g_{\beta 2}[(W/B)/(W/B)_k]$ and $(W/B)/(W/B)_k$ and the predicted values using the DuCOM-COM3 analysis results.

When W/B is small, the increase in $\varepsilon'_{cs}(t, t_0)$ with age tends to be relatively large in young lumber when autogenous shrinkage is predominant (Fig. 2). To represent this trend, β was set smaller for smaller W/B (Fig. 4(f)). The coefficients and constants of the functions were determined so that $g_{\beta 1}[H/H_k]$ and $g_{\beta 2}[(W/B)/(W/B)_k]$ are set to be 1 respectively for parameter corresponding to the standard values of shrinkage strain.

3.3 Consideration of the effect of water entrainment in the prediction equation

Since the effect of water exposure is assumed for only one of the two exposed surfaces, so that the boundary conditions for moisture supply are asymmetric, the trend is different from the effect of RH on $\varepsilon'_{cs}(t, t_0)$. Therefore, the coefficient k_r in (2), which expresses the effect of water exposure, is expressed as the function of the ratio between the shrinkage strain at the age of 2000 days with and without supplied liquid water.

3.4 Prediction equation and its characteristics

Substituting the equation in Fig.4 into (2)(3) with the respective parameters$(W/B)_k$=0.50, RH_k=60%, $(t_0)_k$=7 days, and $(\varepsilon'_{ag})_k$=400 ($\times 10^{-6}$) corresponding to the standard values of $\varepsilon'_{cs\infty}$, (4)-(10) are obtained.

$$\varepsilon'_{cs}(t, t_0) = \varepsilon'_{cs\infty} \times [(t - t_0)/\{\beta + (t - t_0)\}] \quad (4)$$

$$\varepsilon'_{cs\infty} = k_r \times 600 \times (H/H_k)^{-1/10} \times k_c \times (W/B)^{1/2} \times (RH/100)^{-1} \times k_{t0} \times k_{ag} \quad (5)$$

$$k_r = 1.0 \text{ (always dry)}$$
$$= 0.8 \text{ (wet and dry, } H = 1000 \text{ mm)}$$
$$= 0.6 \text{ (wet and dry, } H = 400 \text{ mm)} \quad (6)$$
$$= 0.5 \text{ (wet and dry, } H = 200 \text{ mm)}$$

$$k_c = 1.0 \text{ (N, BB)}$$
$$= 0.9 \text{ (FB)} \quad (7)$$

$$k_{f0} = -0.16 \times \log(t_0 / 7) + 1 \quad (8)$$

$$k_{ag} = 0.0007 \times (\varepsilon'_{ag} - 400) + 1 \quad (9)$$

$$\beta = 2700 \times (H / H_k)^{1/3} \times (W/B)^3 \quad (10)$$

where $\varepsilon'_{cs}(t, t_0)$: shrinkage strain of concrete from age t_0 to t ($\times 10^{-6}$), t: age of concrete (days), t_0: age of concrete at start of drying (days) ($1 \le t_0 \le 365$), $\varepsilon'_{cs\infty}$: final value of shrinkage strain ($\times 10^{-6}$), k_r: coefficient of influence of degree of water exposure, RH: relative humidity of the air (%), ($55\% \le RH \le 85\%$), k_c: coefficient of influence of cement type, H: member thickness (distance between exposed surfaces) (mm) ($100 \le H \le 1000$), H_k: standard member thickness (mm) (=400), k_{t0}: coefficient of influence of age at start of drying, k_{ag}: coefficient for the effect of coarse aggregate shrinkage, ε'_{ag}: shrinkage strain ($\times 10^{-6}$) ($0 \le \varepsilon'_{ag} \le 1200$) in the dry state of aggregate, β: term for the aging characteristic of shrinkage strain, W/B: water-binder ratio ($0.35 \le W/B \le 0.50$). Equation (4) is based on the analysis results for a unit water content of W = 160 kg/m^3 and dry conditions on two surfaces. The effect of water-holding is considered only on one of the two surfaces, and the liquid water action time t_{pre} per 28 days is less than about 4 days.

Figure 5 shows an example of the comparison of the predictions by (4) with the analytical results from DuCOM-COM3. Note that ε'_{ag}=800×10^{-6} is used here. Since the analytical values increase or decrease linearly with ε'_{ag} and it is clear that this relationship is not affected by the age of the wood or W/B, the comparison is omit-

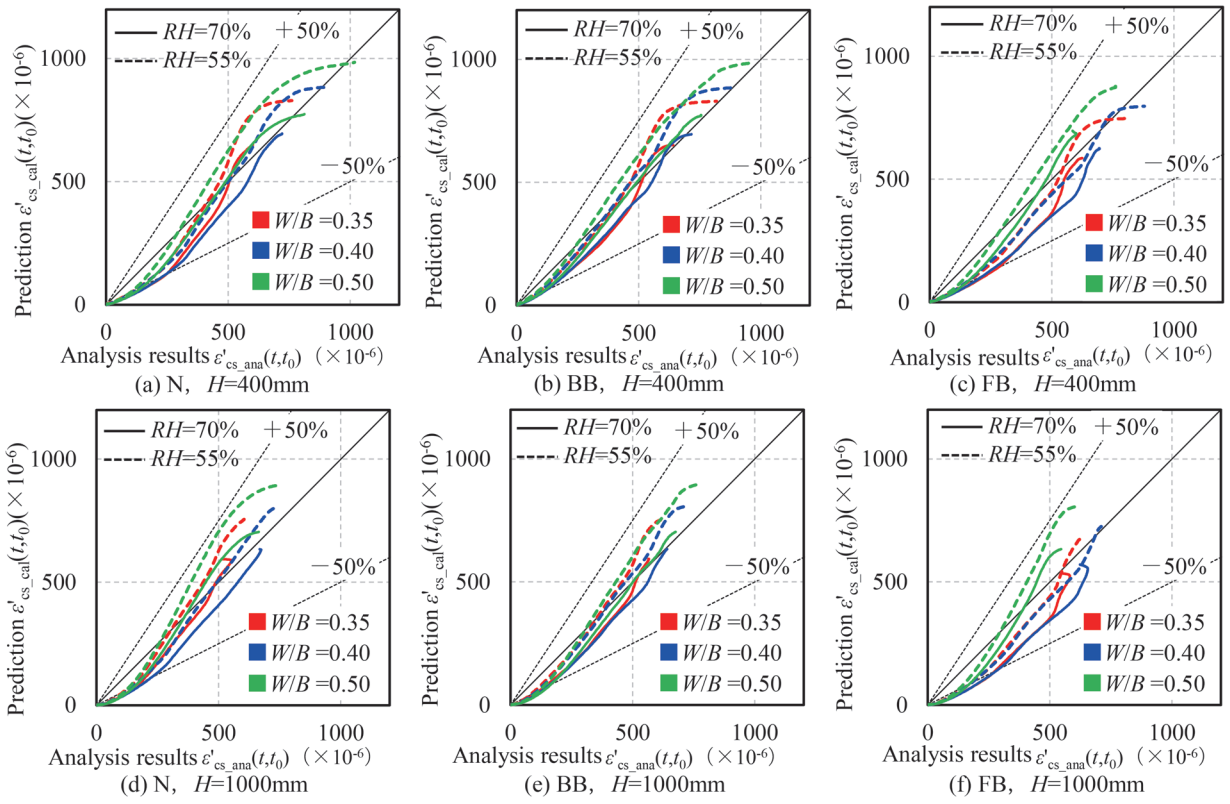

Fig. 5 Comparison of predicted and analyzed values using (4) (base case, always dry, ε'_{ag} = 800 (×10^{-6}))

ted in Fig. 5. Equation (4) is formulated for H=400 to 1000 mm, RH=70%, and W/B=0.40, which is common for prestressed concrete (PC) structures. In particular, shrinkage strains are captured for BB and FB, member thickness H (=1000 mm) and low water-binder ratio W/B (=0.35).

Equation (4) is formulated to capture the deformation of the structure over a long period of time so that the accuracy of the calculation does not depend on each influence factor. Then, (4) is calculated to approach the final value of shrinkage strain, $\varepsilon'_{cs\infty}$, at a slightly earlier age than the analytical value, especially for $H \geq 400$ mm. Even in that case, $\varepsilon'_{cs\infty}$ was formulated to capture the analytical value.

In the analytical values of DuCOM-COM3, for example, when H=1000 mm and W/B is small, the shrinkage strain turns to decrease as the age of the lumber increases. This is due to the fact that FB and BB have a high degree of self-drying due to hydration. (4) does not faithfully reproduce this decrease in strain, but ε'_{cs} is formulated to approximately capture the analytical values.

4. Comparison of measured and predicted values for PC bridges

The subject structure was one of two simple PCT-type main girders (38.25 m in span). BB was used as the cement of which the nominal strength of the concrete was 45, W/B=0.352, and W=154 kg/m^3. The annual mean normal values of air temperature and relative humidity near the measurement points were 18.6°C and 69.3%, respectively.

Figure 6 shows the strain in the concrete measured by the stress-free meter placed on the top flange and web of the PC girders, as well as the predicted values. As shown in Figs. 6(c) and 6(d), despite the small H, the increase in the measured values of the upper flange with age is smaller than that of the web. From this result, it is confirmed that the shrinkage strain is suppressed mainly due to the effect of water exposure.

The upper flange and the web were assumed to be the two exposed surfaces, and their thicknesses were defined as H. The thickness of the upper flange and the web were assumed to be the two exposed surfaces, and their thicknesses were defined as H. In modeling the climatic conditions, the web was assumed to be always dry, and the upper flange was assumed to be wet-dry cyclically, assuming that the exposed surface on the top of the girder is affected by water exposure.

The predicted values using (4) demonstrate the characteristics of the site-dependent (top flange, web) effect of water exposure on the measured BB values up to about 2000 days of age and the increase in shrinkage strain with increasing age of the material.

5. Conclusions

Prediction equations for shrinkage strain of concrete for use in the design of concrete structures were developed based on the analytical values of DuCOM-COM3. The prediction equation using hyperbolic functions corresponds to BB and FB in addition to the previously indicated mix proportion of concrete and the relative humidity. Furthermore, it allows the input of regional effects such as relative ambient humidity, the effect of water exposure, and aggregate shrinkage strain. The applicability of shrinkage strain to long-term age is ensured, including concrete with large member thicknesses or low water-binder ratios.

It is confirmed that the proposed prediction equation can explain the increase in strain in in-service pc girders with BBs, which appears to be due in part to shrinkage of the concrete.

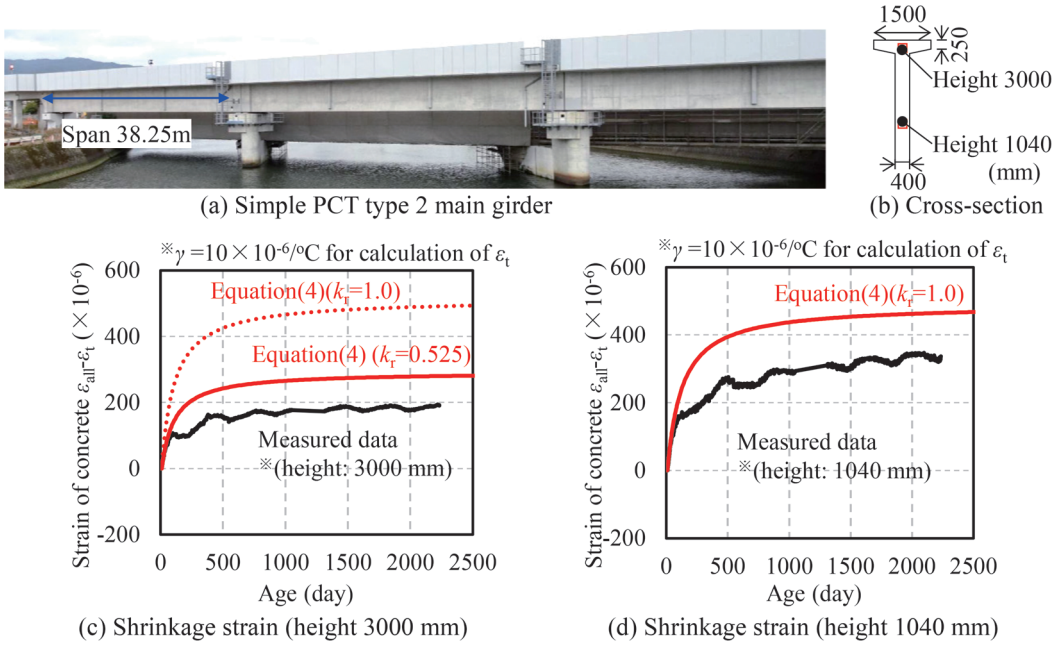

(a) Simple PCT type 2 main girder

(b) Cross-section

(c) Shrinkage strain (height 3000 mm)

(d) Shrinkage strain (height 1040 mm)

Fig. 6 Comparison of predicted and analyzed values using (4) (base case, always dry, ε'_{ag} = 800 (×10⁻⁶))

References

[1] Watanabe, K., Ohno, Y., and Nakamura, M., "Prediction for long-term behavior of railway PC girders affected by creep and shrinkage of concrete," *12th World Congress on Railway Research*, OP_10_5, 2019.

[2] Maekawa, K., Ishida, T. and Kishi, T., "*Multi-Scale Modeling of Structural Concrete*," Taylor and Francis, 2008.

[3] Ohno, M., Chijiwa, N., Suryanto, B. and Maekawa, K., "An Investigation into the Long-term Excessive Deflection of PC Viaducts by Using 3D Multi-scale Integrated Analysis," *J. of Advanced Concrete Technology*, Vol. 10, pp. 47-58, 2012.

[4] Watanabe, K., Nakamura, M., Ishida, T., and Watanabe, T., "Prediction equation for shrinkage strain of concrete considering the effect of mixed cement and supplied water," *J. of JSCE E2 (Material and Concrete Structures)*, Vol. 78, No. 1, pp. 105-120, 2022 (in Japanese).

[5] Meteorological Agency: http://www.jma.go.jp/jma/index.html (Reference date: November 4, 2020) (in Japanese).

Authors

Ken WATANABE, Ph.D.
Senior Chief Researcher, Head of Concrete Structures Laboratory, Structures Technology Division
Research Areas: Design and Maintenance of Concrete Structures

Tetsuya ISHIDA, Dr.Eng.
Professor, Department of Civil Engineering, The University of Tokyo
Research Areas: Multi-scale and Multi-chemo-physics Modeling of Structural Concrete

Mami NAKAMURA
Researcher, Concrete Structures Laboratory, Structures Technology Division
Research Areas: Design and Maintenance of Concrete Structures

Tadatomo WATANABE, Dr.Eng.
(former President, HRC Research Institute Co.,LTD)
Research Areas: Railway Engineering, Concrete Structures

Test Method for Loading Tracks Composed of a Single Set of Rail Fastening Systems for Rail Joints

Shingo TAMAGAWA **Tadashi DESHIMARU**
Track Structures & Components Laboratory, Track Technology Division

Tomoyuki YAMAMOTO
Track Structures & Components Laboratory, Track Technology Division (Former)

This study aims to establish a test method for loading test tracks composed of a single set of rail fastenings for rail joints. The authors of this paper constructed FEM models for railway tracks which represent rail joint parts accurately and performed an FEM analysis. The FEM results are in good agreement with the results of a load test on a test track composed of multiple sets of rail fastenings. On the basis of the FEM model, the authors proposed a test method for loading test tracks composed of a single set of rail fastenings and compared the test results of a single set of rail fastenings with those of multiple sets of rail fastenings. The results show that rail head displacements and rail tilting angles obtained by a single set of rail fastenings are in good agreement with those obtained by multiple sets of rail fastenings. Therefore, it is concluded that the proposed method based on the FEM model is able to evaluate the performance of rail fastening systems for rail joints.

***Key words*:** *rail joints, rail fastening systems, test method, FEM*

1. Introduction

Rail fastening systems are required to ensure safety against fatigue fractures. The Japanese design standard for railway structures (Track structure) [1] requires the safety to be verified by either of the following two load tests:

(a) Load test for tracks composed of multiple sets of rail fastenings
(b) Load test for tracks composed of a single set of rail fastenings

Figure 1 shows examples of the two load tests. The load test (a) is a test using a test specimen more similar to actual railway tracks than (b). When the load test (a) is selected, the design loads shown in Table 1 are generally used as the test loads [2]. On the other hand, the load test (b) is normally selected because the test can be performed by using a smaller number of components, simpler constitution, and less manpower than those of (a). When selecting the load test (b), the test load must be applied to the rail after considering the load dispersion by the tracks. As shown in Fig. 2, the dispersed vertical loads, lateral loads, and rail tilting moments should be applied to a single set of rail fastenings. Vertical and lateral loads refer to the dispersed forces that act on a single set of rail fastenings when the wheel loads and lateral loads act on the tracks. Rail tilting moments refer to the moments by rail tilting that act on a single set of rail fastenings. These dispersed loads depend on the structures and spring coefficients of rail fastenings, and so they should be calculated according to the types of rail fastenings and the support condition of sleepers.

The dispersed vertical loads, lateral loads, and rail tilting moments have been calculated so far by the beam theory on an elastic support [3] and the practical solution based on the torsion theory [4]. However, a recent study has reported that the calculation values based on these theories do not agree well with the experimental values [5]. In order to improve the accuracy of calculation, the authors constructed FEM models of tracks to calculate the dispersed loads and proposed a method to determine load conditions [6]. However, these models are intended for a section without rail joints.

This study aims to construct FEM models of tracks with rail joints and establish a method for load testing for tracks composed of a single set of rail fastenings for rail joints [7].

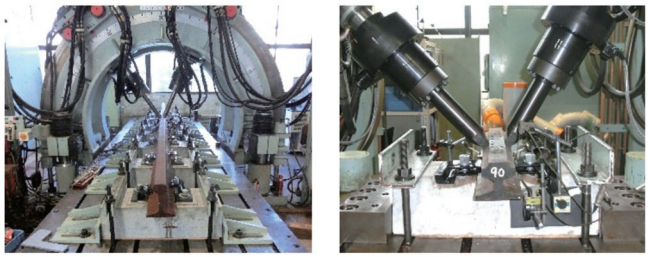

(a) Load test on a test track composed of multiple sets of rail fastenings (b) Load test on a test track composed of a single set of rail fastenings

Fig. 1 Two types of load tests to evaluate the performance of rail fastening systems

Table 1 Design loads of rail fastenings for meter-gauged line

Loads	Alignments	Design loads A	Design loads B
Wheel load	Tangent and curved line	97.5 kN	86 kN
Lateral load	$R < 600$ m	60 kN	30 kN
	600 m $\leq R <$ 800 m	45 kN	22 kN
	800 m $\leq R$, Tangent line	30 kN	15 kN

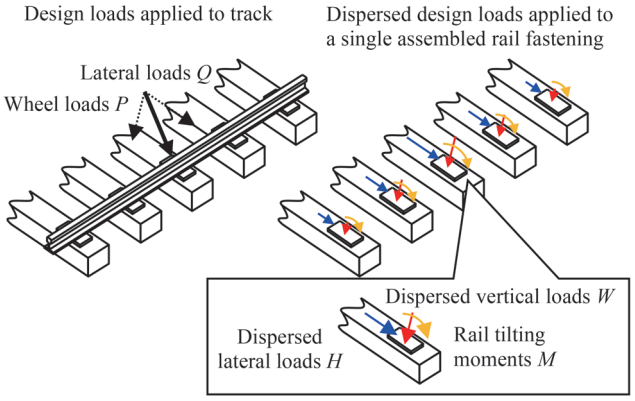

Fig. 2 Dispersed loads applied to a single set of rail fastenings

2. FEM models of tracks with rail joints

This study focuses on the standard rail joints. Figure 3 shows FEM models of track with standard rail joints. In order to analyze various types of rail fastenings, the track components have been simplified as much as possible in the FEM model. The rails are modeled by solid elements in order to simulate its bending and torsion deformation. Fish plates and joint bolts are modeled using solid elements. The contacting surface between fish plates and rails is modeled using gap elements. Axial tensile forces of joint bolts are simulated by decreasing the temperature of joint bolts. The vertical supporting effect of rail clips is modeled by nonlinear elastic spring elements called tip elements. The lateral supporting effect of rails is modeled by nonlinear elastic spring elements called lateral elements. Lateral elements are divided into two types: effect of rail clips and effect of base plates. Rail pads and ballast are also modeled using nonlinear elastic spring elements called springs under rails and springs under sleepers. Sleepers are modeled by plate elements. It is possible to set the spring coefficients or the connection position of spring elements. Furthermore, it is possible to arbitrarily set total number of sleepers and sleeper spans.

FEM analyses executed in this study are nonlinear elastic analyses using NASTRAN software.

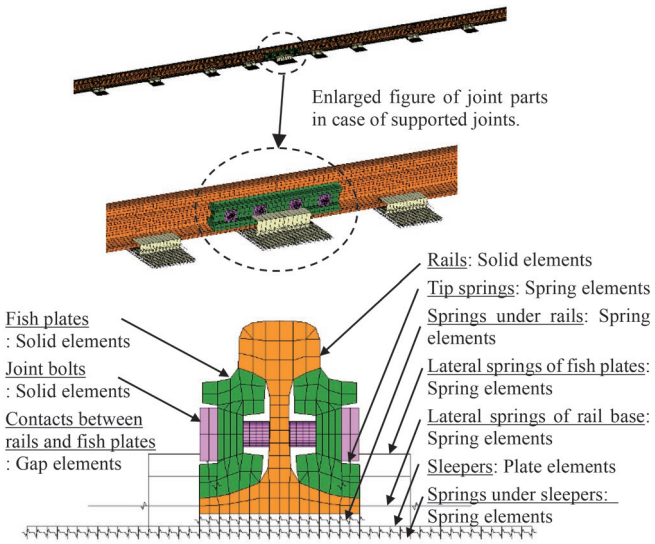

Fig. 3 FEM analytical model of rail joint parts

3. Validity of the FEM models

3.1 Spring coefficients

Spring coefficients were measured and incorporated into the FEM models. This chapter focuses on the type-H rail fastening system as shown in Fig. 4, which is typically used in rail joints of ballasted tracks in Japan.

Figure 5 shows the tests states of coefficients of springs under rails, tip spring and lateral springs. These tests were performed in the same way as the tests shown in reference [6].

Figure 6 shows relationships between loads and displacements obtained from the tests. The test results are approximated by multi-linear shapes to reflect on the FEM models. Loads shown in Fig. 6 are converted into the values per spring by dividing by the total number of springs under rails, tip springs and lateral springs. As the test results of tip springs, the clamping force P_0 is 9.7 kN. The frictional forces between rail clips and rail joints are expressed by lateral springs and are estimated by multiplying the clamping force

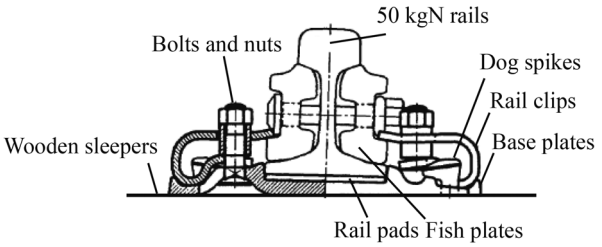

Fig. 4 Type-H rail fastening systems for 50 kgN rails

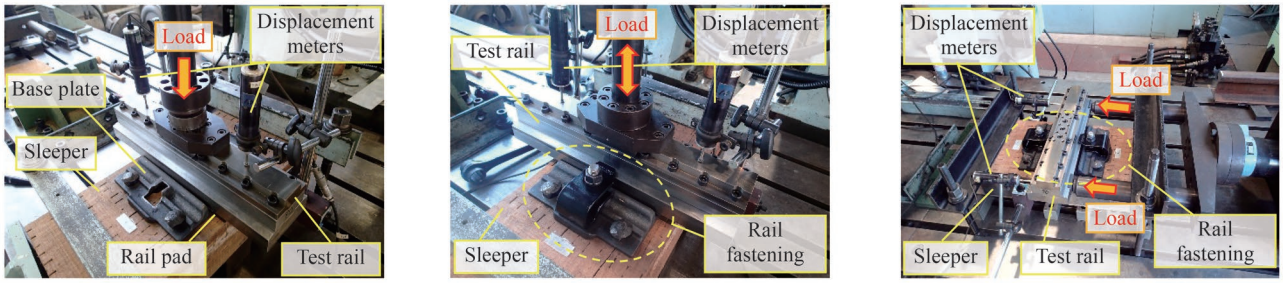

(a) Measurement of springs under rail (b) Measurement of tip springs (c) Measurement of lateral springs of rail base

Fig. 5 Measurements of spring coefficients of type-H rail fastening systems

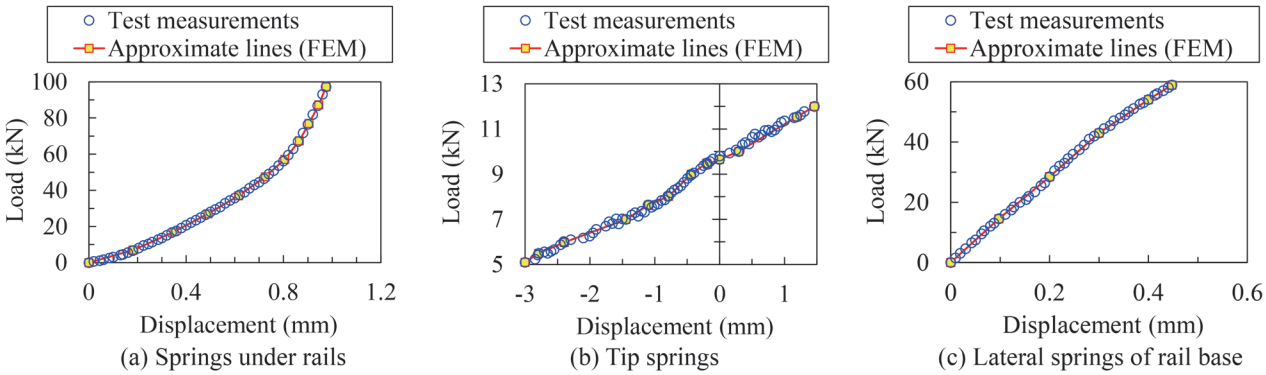

Fig. 6 Relationships between loads and displacements obtained from the measurement

P_0 by frictional coefficient 0.3. The value of the springs under the sleepers is 41.4 kN/mm. This value is the spring coefficient of the rubber pads which simulate the ballast and soil roadbed. The rubber pads are set under sleepers and compose the test track mentioned in the next section.

3.2 Load test of test track

In order to check the validity of the FEM model, load tests on the test track were carried out and the test results were compared with the FEM results. Figure 7 shows the configuration of test track. The test track is composed of a jointed rail with the total length of 5 m, a wooden sleeper, type-H rail fastenings, PC sleepers, type-9 rail fastenings and rubber pads.

Figure 8 shows the status of the load test. A maximum load of 100 kN was applied to the side of the rail head at angles of 45° to 65°. The relationships between loads and lateral rail displacements and between loads and rail tilting angles were measured.

In order to compare FEM results with test results, analyses using the FEM model shown in Chapter 2 were performed. The components of the FEM model were the same as the test tracks and the total length of the FEM model was 5 m. The spring coefficients of type-H rail fastenings used in the FEM model were given using the results of Section 3.1. The temperature reduction of joint bolts for clamping fish plates was -300.4 ℃. This value was determined such that the axial force of joint bolts is 127 kN (tightening torque 500 Nm) and was calculated by FEM analyses using temperature reduction of joint bolts as parameters. A rail gap of joint parts of the model was 6 mm and was the same as test tracks.

Figure 9 shows rail head displacements, rail base displacements and rail tilting angles obtained from the FEM and load test. A comparison of the rail head displacements obtained in the FEM with those obtained in the test, showed that FEM values are 0.98-1.14 times those obtained in the test. This shows that FEM results are in

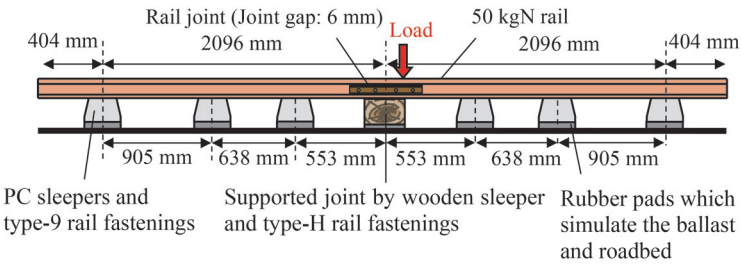

Fig. 7 Configuration of test track

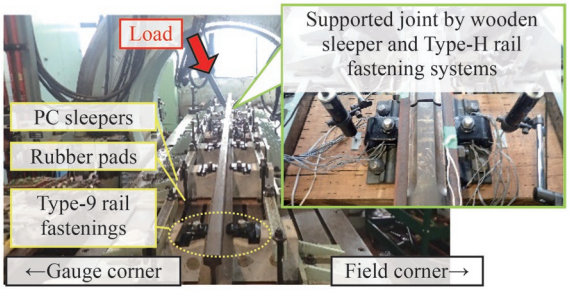

Fig. 8 View of test apparatus

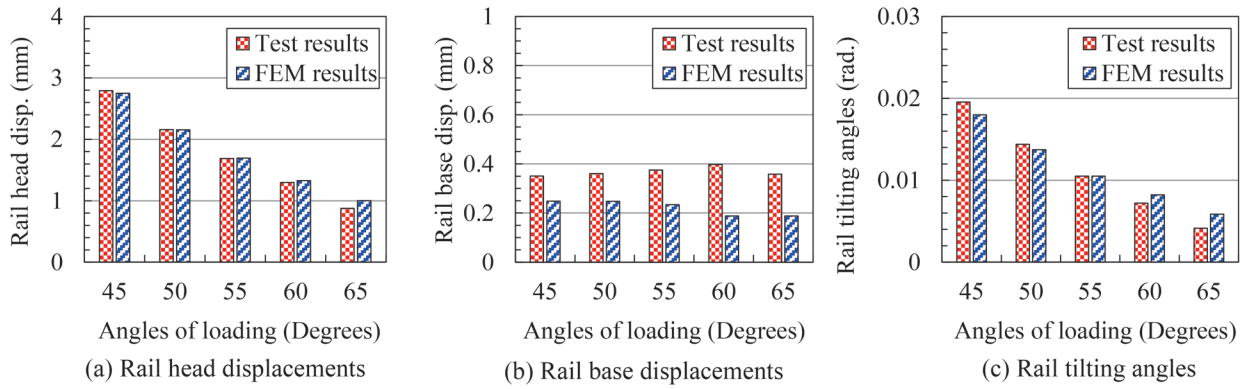

Fig. 9 Comparison between Test results and FEM results

good agreement with test results. Comparing the rail tilting angles by FEM with those obtained in tests when the loading angles were 45° to 60°, showed that FEM values are 0.92-1.41 times those in the test. This demonstrates that FEM results are in good agreement with test results. However, in the case of rail base displacements, the FEM results are 0.47-0.71 times of those from the tests. This indicates that FEM results do not agree well the test results. However, the differences between FEM and the test values of the rail base displacements are 0.2 mm. This means that the influence of the differences on the behavior of the rail and the rail fastenings is small.

The FEM model properly reproduces the test results such as rail head displacements and rail titling angles which are important to evaluate the performance of rail fastenings. Therefore, it should be concluded that the FEM model is an appropriate tool for predicting the reaction of rail and rail fastenings at rail joints.

4. Load test method for a single set of rail fastenings for rail joints and validity of the method

4.1 Test method for a single set of rail fastenings

Generally, the design loads A (the extreme loads) of rail fastenings for rail joints are determined [8] by multiplying the values of load A shown in Table 1 by the coefficient k defined by equation (1). The design loads B (the typical loads) of rail fastenings for rail joints are the same values as those of rail fastenings for general section shown in Table 1.

$$k = (1 + 0.5\,v / 100) / 1.3 \tag{1}$$

where, v is train speed (km/h). The value of the coefficient k is more than 1.0 ($v \geq 60$ km/h).

The dispersed loads such as dispersed vertical loads, dispersed lateral loads, and rail tilting moments that apply on a single set of rail fastenings can be calculated by the FEM model. When design loads A which are composed of wheel loads P_A and lateral loads Q_A apply to the FEM model, dispersed vertical loads W_A, dispersed lateral loads H_A and rail tilting moments M_A can be estimated by calculating the sum of reaction forces of spring elements of the FEM model as shown in the following equations (wherein each symbol is as defined in Fig. 10).

$$W_A = \sum_{i=-n}^{n} (W_i) - (P_L + P_R) \tag{2}$$

$$H_A = R_L + R_R + F_L + F_R \tag{3}$$

$$M_A = \sum_{i=1}^{n} (W_i \cdot b_i) - \sum_{i=-n}^{-1} (W_i \cdot b_i) + (P_L \cdot d_L - P_R \cdot d_R) + (R_L + R_R) \cdot c + (F_L + F_R) \cdot f \tag{4}$$

When load test of a single set of rail fastenings is performed, dispersed vertical loads W_A, dispersed lateral loads H_A, and rail tilting moment M_A calculated by equations (2), (3) and (4) should be applied to the rail. When dispersed vertical and lateral loads are applied to a regular height rail, a moment exceeds the value of M_A calculated above. In order to prevent the occurrence of the excessive moment, a low-height rail (hereafter, test rail) should be used.

Figure 11 shows the test rail with newly produced rail joints. The test rail is composed of a head, a web and a base. The head and base are common members while the web is used to adjust the height of the loading points.

When the dispersed design loads A and loads B obtained from equations (2) to (4) are applied to the test rail alternately from the gauge corner and the field corner of rail, the test loads L_A and L_B, the angles of load application θ_A and θ_B, and the height of load application h are expressed by the following equations.

$$L_A = \sqrt{(W_A - L_0 \sin\theta_B)^2 + (H_A + L_0 \cos\theta_B)^2} \tag{5}$$

$$L_B = \sqrt{(W_B - L_0 \sin\theta_A)^2 + (H_B + L_0 \cos\theta_A)^2} \tag{6}$$

$$\theta_A = \tan^{-1}\left(\frac{W_A - L_0 \sin\theta_B}{H_A + L_0 \cos\theta_B}\right) \tag{7}$$

$$\theta_B = \tan^{-1}\left(\frac{W_B - L_0 \sin\theta_A}{H_B + L_0 \cos\theta_A}\right) \tag{8}$$

$$h = \frac{M_A + e\,(W_A - 2L_0 \sin\theta_B)}{H_A} \tag{9}$$

$$h = \frac{M_B + e\,(W_B - 2L_0 \sin\theta_A)}{H_B} \tag{10}$$

The definition of each symbol in the above equations is described in Fig. 12. The minimum loads L_0 is applied in the opposite direction to L_A or L_B and is set at 5 kN in consideration of stability of the test. The distance e is determined by the width of the test rail and is set at 30 mm. The height h can be selected by the height of test rail 60 mm to 110 mm and is set to satisfy equations (9) and (10).

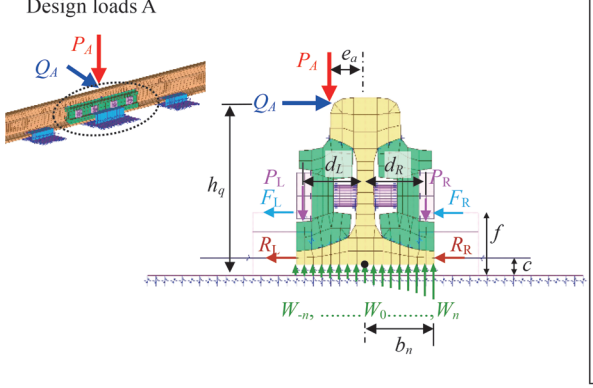

P_A: Wheel load (Design loads A), Q_A: Lateral load (Design loads A)
e_a: Distance between P_A and center of rail
h_q: Distance between Q_A and bottom surface of rail
P_L: Reaction force of tip spring (Gauge corner)
P_R: Reaction force of tip spring (Field corner)
d_L: Distance between tip spring and origin (Gauge corner)
d_R: Distance between tip spring and origin (Field corner)
W_i: Reaction force of springs under rail No.i (i= -n to n)
b_i : Distance between springs under rail No.i (i= -n to n)
F_R: Reaction force of lateral spring of fish plates (Field corner)
F_L: Reaction force of lateral spring of fish plates (Gauge corner)
f : Distance between lateral spring of fish plates and origin
R_L: Reaction force of lateral spring of rail base (Gauge corner)
R_R: Reaction force of lateral spring of rail base (Field corner)
c : Distance between lateral spring of rail base and origin
W_A: Dispersed vertical load, H_A: Dispersed lateral load, M_A: Rail tilting moment

Fig. 10 FEM model balanced under wheel load and lateral load

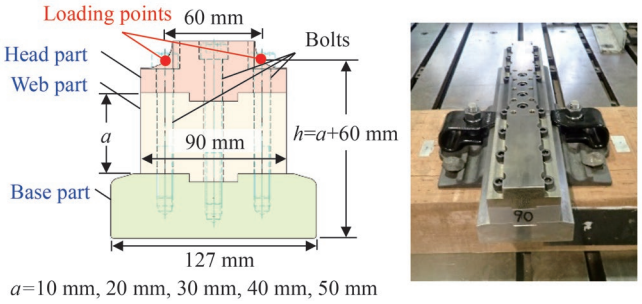

Fig. 11 Test rail for rail fastening systems of rail joints (50 kgN rails)

L_A: Test load (Gauge corner) L_B: Test load (Field corner)
θ_A: Angle of load application (Gauge corner)
θ_B: Angle of load application (Field corner)
L_0: Minimum load applied during the test
h: Height of loading points
e: Distance between L_A or L_B and center of test rail (30 mm)

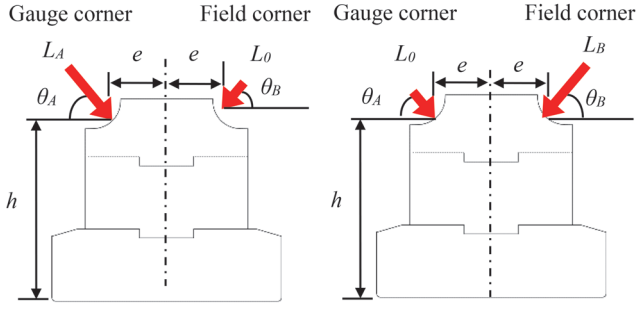

(a) Design loads A (b) Design loads B

Fig. 12 Bi-axial loading condition

4.2 Calculation of loading conditions and its verification

This section shows the calculation of loading conditions for tracks composed of a single set of type-H rail fastenings and the verification of the calculation. In the calculation, the radius of curvature of rail tracks was less than 600 m, and the train speed was 100 km/h. By referring to Table 1 and equation (1), wheel load P_A was 112.5 kN, lateral load Q_A was 69.2 kN; wheel load P_B was 86 kN and lateral load Q_B was 30 kN.

Applying P_A, Q_A, P_B and Q_B to the FEM model shown in Chapter 2, the dispersed loads were calculated from equations (2) to (4). Then, the loading conditions were calculated using equations (5) to (10). Table 2 shows the calculated results for the loading conditions.

Based on the loading conditions shown in Table 2, a loading test was carried out on a test track composed of a single set of rail fastenings. Figure 13 shows the state of the test. A test rail and a single set of type-H rail fastenings were assembled on a sleeper, and the test loads L_A and L_B were alternately applied to a test rail from gauge corner and field corner. In the test, the rail head displacements, rail base displacements and rail tilting angles were measured.

A load test was then carried out on a test track composed of multiple sets of rail fastenings. The test track was assembled in the same way as described in section 3.2. The design load A (the resultant load L_A' of wheel load P_A=112.5 kN and lateral load Q_A=69.2 kN) and the design load B (the resultant loads L_B' of wheel load P_B=86 kN and lateral load Q_B=30 kN) were applied to the test track, and then the rail head displacements, rail base displacements and rail tilting angles were measured.

Table 2 Calculation results of loading conditions

Item		values
Test load (Gauge corner)	L_A	68.2 kN
Angle of load application (Gauge corner)	θ_A	38.5°
Test load (Field corner)	L_B	39.2 kN
Angle of load application (Field corner)	θ_B	50.2°
Minimum load	L_0	5 kN
Heigh of loading points	h	70 mm
Horizontal distance	e	30 mm

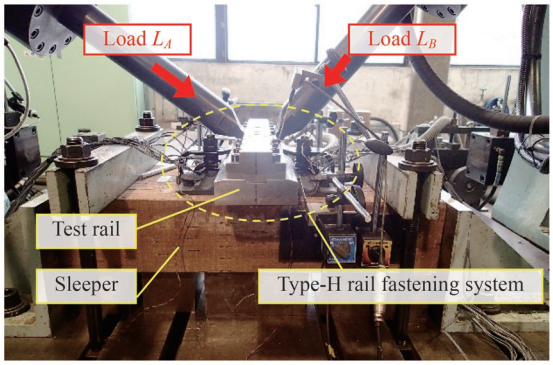

Fig. 13 State of test for test track composed of a single set of rail fastenings

Figure 14 shows the comparison of the rail head displacements, rail base displacements and rail tilting angles obtained in both load tests. Regarding rail head displacements, the result of a single set of rail fastenings was 1.08 times of the results of multiple sets of rail fastenings when L_A was applied and was 0.85 times of that when L_B was applied. As regards rail base displacement, the result of a single set of rail fastenings was 3.15 times the results obtained for multiple sets of rail fastenings when L_A was applied and was 0.54 times of that when L_B was applied. As for rail tilting angles, the result of a single set of rail fastenings was 0.78 times the result obtained with multiple sets of rail fastenings when L_A was applied, and 0.99 times of that obtained when L_B was applied.

From the above results, although there is room for improvement in rail base displacements under loading L_A, a comparison of the rail head displacements and rail tilting angles obtained from both load tests, which are important to evaluate the performance of rail fastenings, shows good agreement.

Therefore, it is concluded that the validity of load test method for a single set of rail fastenings for rail joints based on the FEM model is verified and that the proposed load test method can be used for verification of safety against fatigue fractures in rail fastenings of rail joints.

5. Conclusions

This study aimed to establish a test method for loading test tracks composed of a single set of rail fastenings for rail joints. The obtained results obtained in this study can be summarized as follows:

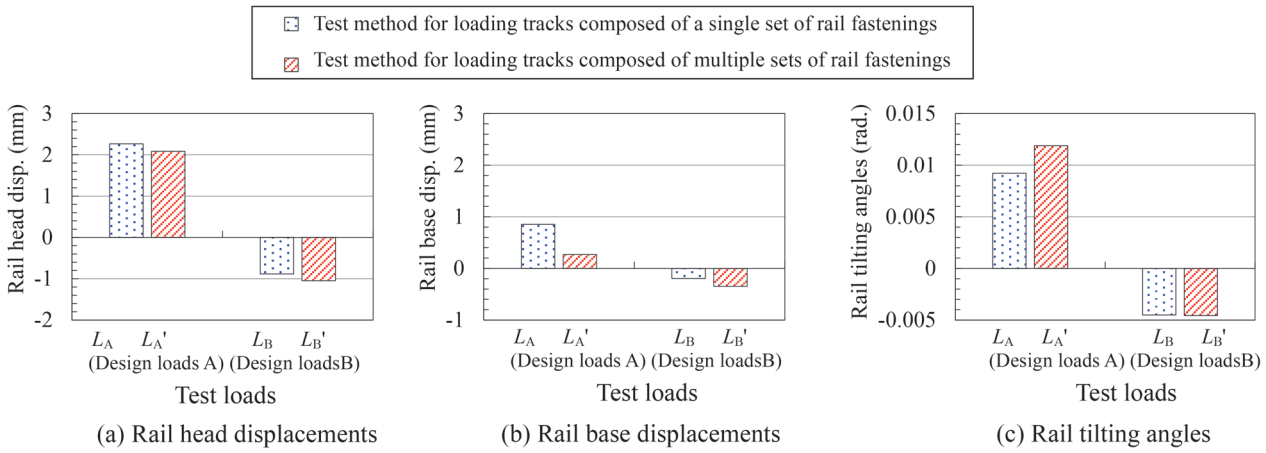

Fig. 14 Load test results of the test track composed of multiple sets of rail fastenings and the test track composed of a single rail fastening

1) The FEM model was proposed which can represent rail joint parts accurately and simplify the various types of rail fastenings and rail supporting structures.
2) The rail head displacements and rail tilting angles obtained by the FEM model were in good agreement with that obtained by the load test on a test track composed of multiple sets of rail fastenings.
3) The method of determining loading condition based on the FEM model was proposed for the load test of a single set of rail fastenings. Furthermore, height adjustable test rail of rail joints was newly produced.
4) It is concluded that the validity of load test method for a single set of rail fastenings for rail joints based on the FEM model is verified, and that the proposed load test method can be used for verification of safety against fatigue fractures in rail fastenings of rail joints.

References

[1] Railway Technical Research Institute, *Design Standards for Railway Structures and Commentary (Track Structures)*, pp. 31-78, Maruzen, 2012 (in Japanese).
[2] Miura, S., *Kidou Zairyou (Track structures & components)*, Tetsudo Gengyosha, pp. 283-284, 2011 (in Japanese).
[3] Kato, Y., *Rail*, Japan Railway Civil Engineering Association, pp. 124-170, 1987 (in Japanese).
[4] Yamamoto, T., Umeda, S. and Kanamori, T., "Relationship between Spring Coefficient of Fastening Device and Rail Overturning Angle," *Quarterly Reports*, Vol. 22, No. 4, pp. 153-156, 1981.
[5] Deshimaru, T., Shono, S., Kataoka, H. and Furukawa, A., "Experimental study on the response of rail fastening clips to the application of train load," *Journal of Railway Engineering*, Vol. 18, pp. 95-102, 2014 (in Japanese).
[6] Tamagawa, S., Kataoka, H. and Deshimaru, T., "Practical model for rail tilting and its application to performance test of rail fastening system," *Journal of JSCE*, Vol. 7, pp. 1-14, 2019.
[7] Tamagawa, S., Deshimaru, T. and Yamamoto, T., "FEM models for jointed railway tracks and a loading test method on test tracks composed of a single rail fastening system at rail joints," *Transactions of the JSME*, Vol. 88, No. 910, pp. 1-13, 2022 (in Japanese).
[8] Deshimaru, T., "Improvement on estimating method of loading conditions for performance test of rail fastening systems," *Newsletter of structural research*, No. 322, pp. 3-4, 2017 (in Japanese).

Authors

Shingo TAMAGAWA, Ph.D.
Senior Researcher, Track Structures & Components Laboratory, Track Technology Division
Research Areas: Rail Fastening Systems, Continuous Welded Rails

Tadashi DESHIMARU, Ph.D.
Senior Researcher, Track Structures & Components Laboratory, Track Technology Division
Research Areas: Railway Rails, Rail Fastening Systems

Tomoyuki YAMAMOTO
Researcher, Track Structures & Components Laboratory, Track Technology Division (Former)
Research Areas: Rail Fastening Systems, Switch & Crossing

Development of a Method for Detecting Track Irregularity Anomalies by Cluster Analysis

Mami MATSUMOTO
Track Geometry & Maintenance Laboratory, Track Technology Division

Masashi MIWA
Tokyo Keizai University

Tatsuo OYAMA
National Graduate Institute for Policy Studies

When a train repeatedly runs on a track, track irregularities, which are distortions of the track, gradually increase with repetition of wheel load. Tracks are normally inspected periodically so that maintenance can be carried out when a large track irregularities are detected. However, in rare cases, the magnitude of a track irregularity may rapidly increase locally. To ensure the safety of train operations, preventive maintenance is required to detect the signs of such rapid increases in the magnitude of irregularities and to perform maintenance before large irregularities occur. In this study, to identify in advance locations where large track irregularities are likely to occur, we developed a mathematical model that applies cluster analysis to historical data for track irregularities and maintenance records.

Key words**:** *anomaly detection, cluster analysis, track irregularity, historical data, track maintenance*

1. Introduction

When trains run repeatedly on ballasted track, the ballast and roadbed settle due to the train load, and track irregularities, which are distortions of the track, gradually increase. Therefore, periodic track inspections are usually performed to restore track geometry through systematic maintenance [1]. However, unusual circumstances, such as a large cave-in caused by a cavity beneath the roadbed or an initial settlement caused by the insufficient recovery of support after maintenance due to ballast deterioration, can result in rapidly developing localized track irregularities. Because such anomalies can threaten the safety of running trains and lead to accidents and transport disruptions, it is desirable to detect the signs of such anomalies, identify their locations and trends, and perform track maintenance in advance to ensure the stability of train services.

It may be possible to detect signs of rapidly developing track irregularities by analyzing temporal changes in the track measurement data at wavelengths of about 5-m, which is shorter than the 10-m wavelengths used for general track irregularity management [2]. A track maintenance model has been developed to minimize the amount of maintenance needed by predicting future track irregularities based on historical track measurement data and performing maintenance at the optimal time [3, 4]. In addition, compact, high-precision track inspection devices [5] have recently been developed and installed on commercial trains to collect data multiple times per day, and calculation models [6] have been developed to predict the development of local track irregularities by utilizing this high-frequency inspection data. However, where it is difficult to obtain high-frequency inspection data, such as some railway operators or for certain line sections, such models cannot be applied. Even for railroad operators who are able to obtain high-frequency measurement data, these models predict track irregularities based on recent track irregularity trends and do not consider abnormalities that have occurred in the past.

In this paper, we introduce a track management method that uses cluster analysis with a large amount of historical data to detect anomalies of track irregularities [7, 8].

2. Sampling methods for data collection

To develop the anomaly detection method, the following assumptions were made about the characteristics of the target line segment to be analyzed: i) the annual passing tonnage is approximately 17 to 25 million tons; ii) the total track length is 558.9 km; iii) it is a high-speed line with no freight traffic (Shinkansen); and iv) the track inspection period of frequency is once every 10 days. The data were collected from 2015 to 2020. In other words, data for 168 inspection days were obtained.

Among the possible irregularities, this study focuses on longitudinal level irregularities, which represent vertical distortion. This irregularity is generally measured by placing a reference string on the rail and measuring the distance between the center of a straight line connecting the two ends of the string and the rail at the center of the string. The irregularity obtained in this manner when the length of the reference string is 10 m is called a 10-m-chord irregularity, which is widely used by Japanese railway operators as an indicator for track maintenance. However, the 5-m-chord irregularity, which is obtained when the reference string length is 5 m, is known to detect anomalies caused by the defects of ballast or roadbed more accurately than the 10-m-chord irregularity [2]. Therefore, the 5-m-chord irregularity was mainly utilized in the analyses performed in this study. The total track length of 558.9 km was divided into lots of 100 m each, and the maximum value of the 5-m-chord irregularity was determined for each lot. Moreover, the set of 5,589 lots is referred to as the total lots.

In this analysis, 500 lots, which we call the sample lots, were selected out of the total set of 5,589 lots. In the sampling, we selected the sample set of lots such that their characteristics were as similar as possible to the total set. Accordingly, we considered the following eight categories of characteristics related to track structure, type of rail length, train operations, etc.: i) for the rails, we considered unit length rail, and long rail with glued joints; ii) for the track

bed, we considered the concrete slab, ballast, direct connection to the sleeper, and boundary lot; iii) we classified the linear and curve radii into straight lines and curves. Curves were classified into three categories according to the curve radius, and the composites and joints connected to these curves were added; iv) structure; v) speeds above 170 km/h were classified as high-speed; vi) turnout; vii) expansion joints; and viii) glued-insulated joints of rails were selected so that the percentages of the total and the selected lots compose as similar as possible. It is well known that concrete slabs are widely used on high-speed lines because the occurrence of a track irregularity is unlikely, and the track conditions inside a tunnel tend to be stable because the tracks are less affected by temperature changes at this location than at the mine-head of the tunnels. Moreover, the boundary lots of rails and structures, as well as expansion joints and glued-insulated joints, tend to be weak points; thus, large track irregularities are more likely to occur because those points are difficult to maintain. Figure 1 shows the percentage distribution of the characteristics of the total and sample sets of lots. It can be observed that their percentage distributions are almost identical.

3. Applying cluster analysis to detect anomalies in track irregularities

The following describes an anomaly detection method that uses cluster analysis, which is a statistical method for grouping data based on similarity, where a grouping of data is called a cluster. In this analysis, the k-means method of non-hierarchical clusters was used due to the large amount of data.

3.1 Definition of variables

Table 1 lists the variables used in this analysis; these variables are related to the track irregularity data. MXIL, STDV, and MXDV denote the maximum value, standard deviation, and maximum deviation of the measured track irregularities for the 5-m-chord in the 100 m lot. The NIMP indicates the number of times that the track irregularity improvement was 1 mm or more on consecutive days during the measurement period. NRAD indicates the number of times that the track irregularity development was 2 mm or more on consecutive measurement days. For each of the MXIL, STDV, and MXDV variables, we know that the larger the values, the worse the track condition is likely to be. The NIMP indicates the number of maintenance cycles, whereas MXDV and NRAD are considered to indicate the tendency of the track condition to deteriorate rapidly (or to improve significantly after a single maintenance cycle). In general, the worse the track condition, the higher the maintenance frequency. Therefore, there is a high correlation between MXIL, STDV, and MXDV. The NIMP is defined to be consistent with the maintenance frequency calculated from the maintenance results. In defining NRAD, we set the development to 2 mm because the difference between the operative maintenance target value and the extreme irregularity value of the control indices was 2 mm. Therefore, these indicators effectively represent the line segment characteristics considered in this analysis; it is necessary to consider appropriate values when applying the variables to line segments under different conditions.

3.2 Results of applying cluster analysis technique

We present the numerical results of the cluster analysis on the set of 500 sample lots for the five variables in Table 1. The data were classified into five clusters, assuming the following three patterns: (1) the three levels of control indices depend on the magnitude of the track irregularities, (2) the conditions of the track are stable, and (3) track structures such as slab track are unlikely to occur some

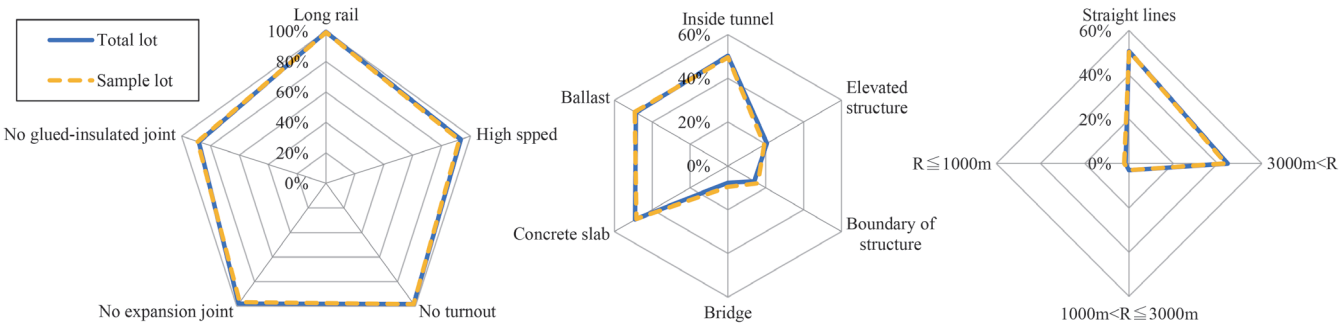

(i) Rail structure **(ii) Structure** **(iii) Linear and curve radii**

Fig. 1 Percentage distribution for characteristics of the total and sample sets of lots

Table 1 Variables list

Variables	Details
MXIL	Maximum irregularity during the measurement period
STDV	Standard deviation during the measurement period
MXDV	Maximum deviation during the measurement period
NIMP	Number of improvements during the measurement period
NRAD	Number of rapid advances during the measurement period

track irregularities.

Table 2 shows the center-of-gravity coordinates, which are the averages of all corresponding values for the variables contained in each cluster, and it also shows the number of lots in the sample lots included in each cluster. Clusters {1, 2, …,5} are denoted as {C1, C2, C3, C4, C5}. In Table 2, the center-of-gravity coordinates of C1 are the largest for almost all variables {MXIL, STDV, MXDV, NIMP, and NRAD} in other clusters. We can see that the variable values for C1, C2, C3, C4, and C5 decrease in the same order, except in the case of variable NIMP, where the magnitudes of the values for C2 and C3 are reversed. This suggests that the magnitudes of the irregularities follow the order of C1, C2, C3, C4, and C5, and that the sample lots in C4 and C5 represent the majority of the sample lots, at approximately 90% of the sample lots, and have the irregularities with the smallest magnitude. Furthermore, the results in Table 2 show that almost 70% of the 500 sample lots were in C5, where the center-of-gravity coordinates had the lowest irregularity.

Table 3 lists the distances of the center-of-gravity coordinates from one of the five clusters to another. From this result, it can be seen that cluster 5 is farther away from C4, C3, C2, and C1, in the given order. Moreover, the result shows that among the five clusters, C1, C2, and C3 are quite close to each other, whereas C4 and C5 are much farther from these three than they are from each other. Thus, we see that they can be divided into two groups, {C1, C2, C3} and {C4, C5}. We propose that the lots in the first group {C1, C2, C3} obtained are those that should be targeted for detection as anomaly irregularity lots. We know that the shorter (longer) the distance between the lot and the center-of-gravity coordinates of the cluster, the more (less) similar it is to the center. Thus, we find that clusters {C1, C2, C3} contain lots with large track irregularity fluctuations and high maintenance frequencies, whereas {C4, C5}, which represent the majority of lots, contain lots with small and stable irregularities. Hence, these lots have insignificant improvement frequencies.

We aim to determine the track structure characteristics of each lot in the cluster. Table 4 shows the percentage of lots in each cluster based on track structure characteristics. The characteristics found in the lots contained in each of the clusters {C1, C2, C3} in the first group defined above are as follows.

All lots in C1 recorded large values of approximately 10 mm for MXIL during the inspection period. In this line section, if the irregularity of the 10-m-chord exceeds 10 mm, it is considered to have an "extreme value" and maintenance work must be performed immediately. Moreover, all lots in C1 were ballasted, showed a large fluctuation in MXIL, and had several NIMP cycles. In addition, half of the lots were located at the boundaries of the structures, and many of them included expansion joints or glued-insulated joints, which tend to deteriorate the track condition. Therefore, C1 was the group that required the most maintenance because it included lots that were maintained at a high-frequency and had large NIMP and NRAD values. In addition, all lots were located in sections with curve radii of 3,000 m or more, or in straight sections with other high-speed lots. This may be due to the fact that the more high-speed lots in this line are more likely to deteriorate track conditions. Moreover, C2 contains lots with MXIL values that are close to the extreme values. Compared with C1, C2 tended to have more lots with a lower maintenance frequency, even though the track condition was poor. This is because C2 contained several lots that were difficult to maintain on a routine schedule and required relatively difficult maintenance work such as track structures, structure boundary areas, and bridges. Such lots often require some preparation before maintenance can be performed. The lots in C2 also belonged to a group that required attention to rapid advances. Lots in C3 also occasionally had a large MXIL with a large NIMP. Although several lots included turnouts, expansion joints, and glued-insulated joints—which are either difficult to maintain or easily return to their original state even after maintenance—they were maintained comparatively regularly. This may be because most lots were managed on site, as they were easily affected by the MXIL.

When we studied the characteristics found in the lots in each of the clusters {C4, C5}, we found C4 mainly contained lots with relatively stable track conditions, although there were some lots that had some MXIL fluctuations and some NIMP. This is due to the fact that many of the lots had curves with small radius than the lots in the other clusters, which resulted in a slower irregularity development due to slower train running speeds and comparatively less impact to the track by the trains. C5, which contained more than half of the sample set of lots, showed the least fluctuation in MXIL of all the clusters. Most lots had no record of maintenance during the measurement period, as the MXIL remained close to 0 mm without fluctuation. More than half of the lots were located slab track, where irregularities did not occur, or in tunnels, which were less affected by temperature changes. Therefore, this group show a relatively

Table 2 Center-of-gravity coordinates by variables and number of lots by cluster

Cluster	MXIL	STDV	MXDV	NIMP	NRAD	n
C1	11.370	1.837	9.607	11	2	6
C2	9.436	1.746	7.696	4	0	27
C3	8.112	1.374	6.024	8	0	19
C4	5.843	1.026	4.070	2	0	116
C5	2.481	0.206	0.957	0	0	332

Table 3 Distances between the cluster centers-of-gravity

Cluster	C1	C2	C3	C4	C5
C1		7.168	5.598	11.739	16.381
C2	-		4.685	5.598	10.591
C3	-	-		6.951	11.192
C4	-	-	-		5.025
C5	-	-	-	-	

consistent track condition.

4. Validation of the method for detecting track irregularity anomalies

In this chapter, we describe the results of our verification of the accuracy in detecting anomalies in track irregularities. Specifically, we analyzed the clusters that contained lots in which large longitudinal level irregularities had occurred or developed in the past.

4.1 Definition and selection of anomaly lots

First, in detecting track irregularity anomalies, we attempted to find lots in the set of sample lots for which a large irregularity or its development had actually occurred. Here again, the control indices based on the value of the 10-m-chord irregularities were applied. In selecting the anormal lots, the following three indicators were used: (i) lots exceeding 10 mm, (ii) lots with 4 mm/10 days advance, and (iii) lots with an extreme irregularity value. Indicator (i) is a lot in which the 5-m-chord MXIL exceeds the extreme value of 10 mm. The operative maintenance target value used as a guide value was 6 mm before the extreme value of 10 mm was reached in the control indices for the 10-m-chord irregularity. Therefore, Indicator (ii) is a lot whose MXIL has reached the operative maintenance target value of 6 mm, and whose maximum value reaches the extreme irregularity value by the next inspection, which is 10 days later. Indicator (iii) is a lot for which 11.2 mm has actually occurred on the 10-m-chord irregularity and the extreme value is exceeded owing to rapid advancement. Among the lots in the sample lot, nine lots were selected as anomaly lots according to Indicator (i), and one lot each were selected according to Indicators (ii) and (iii), for a total of 11 lots. Figure 2 shows examples of longitudinal level irregularities of the anomaly lots for each of the three indicators.

Table 4 Percentages of track structures in each cluster (%)

Track	Item	C1	C2	C3	C4	C5
Rail	Long rail	100	96.3	100	97.4	100
	Unit length rail	0	3.7	0	2.6	0
Track bed	Concrete slab	0	0	5.3	16.4	66.9
	Ballast	100	81.5	84.2	81	32.5
	Boundary	0	18.5	10.5	2.6	0.6
Liner and curve radius R (m)	Straight lines	83.3	70.4	52.6	50.9	48.5
	R >3000	16.7	29.6	47.4	41.4	46.1
	1000< R≤3000	0	0	0	3.4	3.3
	R ≤1000	0	0	0	4.3	1.8
Structure	No structure	16.7	3.7	15.8	10.3	1.2
	Inside tunnel	16.7	7.4	10.5	21.6	65.7
	Mine-head	0	0	5.3	4.3	0.6
	Elevated structure	0	29.6	21.1	26.7	16
	Bridge	16.7	33.3	26.3	16.4	4.2
	Boundary	50	25.9	21.1	20.7	12.3
Speed	High speed	100	96.3	100	89.7	92.2
	Low speed	0	3.7	0	10.3	7.8
Turnout	No turnout	100	96.3	89.5	96.6	99.4
	With 1 turnout	0	3.7	10.5	3.4	0.6
Expansion joint	No expansion joint	83.3	88.9	84.2	92.2	99.7
	Included	16.7	11.1	15.8	7.8	0.3
Glued-insulated joint	No glued-insulated joint	66.7	85.2	78.9	89.7	89.8
	Included	33.3	14.8	21.1	10.3	10.2

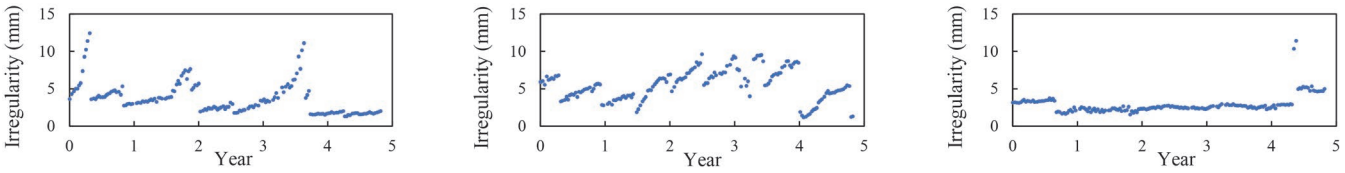

Fig. 2 Examples of longitudinal level irregularity of the anomaly lots

4.2 Cluster characteristics and anomaly lots

Table 5 shows classification result of anomaly lots. The distribution of the 11 lots with anomalies was five lots in C1 and six lots in C2. Thus, all of the anomaly lots were in either C1 or C2. The lots in C1 tended to have a consistently large irregularities among the anomaly lots and needed to be maintained to reduce track irregularity frequently, which implies that these lots had been repeatedly maintained. In C1, five of the six lots were the anomaly lots, but the remaining lot also had an MXIL value of 9.6 mm and a large NIMP value, thus the lot showed a behavior similar to that of Indicator (i). On the other hand, C2 included lots with steady periods of irregularity progression but that tended to occasionally suffer from rapid advances. As can be seen from the cluster analysis results, the distance between the center-of-gravity coordinates for C2 and C3 was small, and both the irregularity data characteristics and the structural characteristics were found to be similar. Furthermore, the lots in C3 also had a large number of NIMP, and large irregularities occurred occasionally. Moreover, C3 has more lots that need maintenance frequently than C2. These lots tended to include lots that are maintained relatively regularly and managed in the field as locations where large irregularities are likely to occur.

Based on these verification results, we conclude that the lots included in C1 or C2, where a large irregularity or rapid advance had actually occurred, should be carefully maintained. Furthermore, even if the MXIL value is not extremely high, such as in C3, we should pay attention to lots having a large NIMP and those including turnouts, expansion joints, and glued-insulated joints. We consider that paying particular attention to the changes in the irregularities and material conditions around the lots included in C1 is effective in preventing the occurrence of extreme values and post-maintenance.

5. Track maintenance by detecting track irregularity anomalies

A cluster analysis technique was used to categorize the lots and characterize each cluster element. We developed a method to apply these classification results to track management by detecting track irregularity anomalies. Table 6 shows the characteristics of each cluster. Starting from C1, the clusters can be characterized as “Warning,” “Caution,” “Semi-Caution,” “Stable,” and “Quite stable.” Thus, the smaller the cluster number, the more these lots should be carefully monitored in terms of track condition. In addition, compared with the previous inspection, there is a possibility of detecting an anomaly lot in advance by choosing lots that have moved closer to or moved into the upper clusters that require caution.

Table 6 Characteristics of each cluster

Cluster	Characteristic
C1	Warning level
C2	Caution level
C3	Semi-caution level
C4	Stable level
C5	Quite stable level

6. Conclusions

In this study, we developed and validated an efficient method for detecting lots that indicate track irregularity anomalies from the perspective of track maintenance management.

The results obtained from this study are summarized as follows. When the cluster analysis technique using variables that were related to irregularities was applied to the 500 sample lots, the lots were classified into five clusters, C1, C2, C3, C4, and C5, in decreasing order from lots with the largest irregularities to lots with the smallest. The lots in clusters {C1, C2, C3}, which accounted for approximately 10% of the total lots, required track maintenance, whereas those in the remaining clusters {C4, C5}, which accounted for approximately 90% of the total, showed good track conditions and did not require maintenance.

Moreover, to validate the method, we analyzed the clusters that contained anomaly lots in which large longitudinal level irregularities or their advance had actually occurred in the past. The results showed that all of these anomaly lots were classified into C1 or C2. Therefore, paying special attention to lots classified as {C1, C2, C3} by this method was considered to be effective in preventing track irregularities that exceeded the extreme value and in preventing emergency maintenance.

In the future, we will focus on improving the generality and practical application of this method.

References

[1] Railway Technical Research Institute, *Handbook of track structures maintenance managements (Track maintenance)*, pp. 9-110, 2007 (in Japanese).

[2] Kimura, H., Tanaka, H., and Shimono, Y., “Detection methods for finding quickly deteriorating lots for vertical displacement irregularities in ballast tracks,” *Proceedings of the 16th Sympo-*

Table 5 Classification result of anomaly lots

Cluster	n	Classification result of anomaly lots
C1	6	lot exceeding 10 mm (4), lot with 4 mm/10 days advance (1)
C2	27	lot exceeding 10 mm (5), lot with the extreme irregularity value (1)
C3	19	
C4	116	
C5	332	

*( ) indicates the number of lots

sium on the Railway Technology Association, 2009 (in Japanese).
[3] Miwa, M., and Oyama, T., "All-integer Type Linear Programming Model Analyses for the Optimal Railway Track Maintenance Scheduling," *OPESEARCH*, Operations Research Society of India, Vol. 41, No. 3, 2004.
[4] Tanaka, H., and Miwa, M., "Modeling the development of rail corrugation to schedule a more economical rail grinding," *Proceedings of the Institution of Mechanical Engineers, Part F: Journal of Rail and Rapid Transit*, 2019. Vol. 234, No. 4, 2019.
[5] Tsubokawa, Y., Yazawa, E., Ogiso, K., and Nanmoku, T., "Development of the Car Body Mounted Track Measuring Device with the Inertial Mid-Chord Offset Method," *RTRI Quarterly Report*, Railway Technical Research Institute, Vol. 53, No. 4, pp. 216-222, 2012.
[6] Tanaka, H., Yamamoto, S., Osima, T., and Miwa, M., "Methods for Detecting and Predicting Localized Rapidly Progressing Deterioration of Track Irregularity Based on the High Frequency Measured Data," *RTRI Report*, Vol. 31, No. 12, pp. 41-46, 2017 (in Japanese).
[7] Matsumoto, M., Miwa, M., Oyama, T., "Empirical analysis of track irregularity anomaly detection model by using clustering method," *Intelligence, Informatics and Infrastructure*, Vol. 2, No. J2, pp. 67-78, 2021 (in Japanese).
[8] Matsumoto, M., Miwa, M., Oyama, T., "Multivariate Analyses for Finding Significant Track Irregularities to Generate an Optimal Track Maintenance Schedule," *American Journal of Operations Research,* Vol. 12, No. 6, pp. 261-292, 2022.

Authors

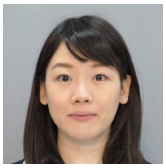

Mami MATSUMOTO
Assistant Senior Researcher, Track Geometry and Maintenance Laboratory, Track Technology Division
Research Areas: Track Geometry Management, Maintenance Support Systems

Masashi MIWA, Ph.D.
Associate Professor, Tokyo Keizai University
Research Areas: Infrastructure Planning and Management, Mathematical Informatics

Tatsuo OYAMA, Professor Emeritus
Professor, National Graduate Institute for Policy Studies
Research Areas: Operations Research, Social Systems Analysis, Quantitative Public Policy Analysis

Method for Evaluating Rail Corrugation Growth Process by Monitoring Vertical Rail Vibration

Hirofumi TANAKA **Kazuhiro KAJIHARA**
Track Geometry & Maintenance Laboratory, Track Technology Division

Rail corrugation causes noise, vibrations, and deterioration of track components, which increase the frequency of track maintenance work. However, a measurement method that efficiently evaluates the growth of rail corrugation has not been established. The authors of this paper have developed a monitoring system for rail corrugation that enables long-term remote measurement of rail vibrations by means of battery-powered accelerometers and a wireless sensor network. In this study, the relationship between vertical rail vibration characteristics and actual rail corrugation measured on commercial lines was investigated to verify the applicability of the developed system for identifying the growth process of rail corrugation.

***Key words*:** *rail corrugation, growth process, rail vibrations, monitoring system, wireless sensor, harmonic component*

1. Introduction

Rail corrugation, as shown in Fig. 1, is regular surface roughness that forms on rails as railway vehicles travel on them. Rail corrugation occurs in various alignment and track structures. When railway vehicles travel across sections with rail corrugation, noise and vibrations are generated leading to deterioration of track components and promotion of further track irregularity. Hence, railway operators work to ascertain the generation of rail corrugation and, depending on conditions, remove surface roughness, mainly by using a rail-grinding car (hereinafter, rail grinding). However, it is difficult to accurately ascertain sporadic rail corrugation on railway tracks.

Many studies and research [1-4 for example] have attempted to identify the mechanism underlying rail corrugation from a variety of viewpoints, but none have been fully successful, so no basic measures against rail corrugation have yet been proposed. The authors of this paper posit however, that it is possible to model the increasing tendency in the amplitude of rail corrugation on a growth curve from the results of regular measurements of rail corrugation on commercial lines [5] and dynamic simulation accounting for track/vehicle interaction [6]. In addition, we believe that the noise and vibrations that pose problems during actual operation actualize during the final "saturation stage" of the growth process. Consequently, more efficient track management may be expected from observing the degree of rail corrugation growth and formulating maintenance plans based on when the "saturation stage" is reached. An efficient method for measuring rail corrugation is the practical use of a portable trolley that continuously and directly measures rail surface roughness [7]. Using this trolley for regular measurement of rail surface roughness makes it possible to ascertain the growth tendency in rail corrugation [5], however high-frequency measurements are labor-intensive.

Therefore, in this study, we explored a method for constantly monitoring measurable rail vibration acceleration with relative ease and evaluating the growth process of rail corrugation from changes in vibration characteristics. We therefore constructed a measurement system using a battery-powered wireless acceleration sensor, installed it in a sharp curve on a commercial line where rail corrugation had been generated, and continuously acquired data. Thus, we analyzed the relationship between the vibration characteristics of rail vibration acceleration and rail surface roughness and verified the efficacy of the proposed method.

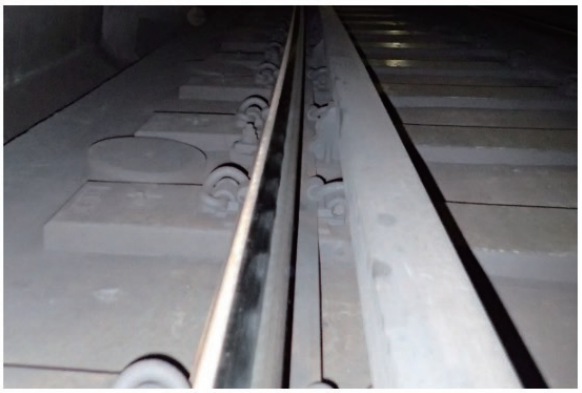

Fig. 1 Example of rail corrugation generation

2. Growth process of rail corrugation and its characteristics

Figure 2 shows a model of the growth process of rail corrugation proposed by the authors [6]. The growth process of rail corrugation has three stages – the "formation stage," "growth stage" and "saturation stage" – and the increasing tendency of rail corrugation amplitude can be modeled with a growth curve. Here, the "formation stage" is when minute irregular rail surface roughness forms, the "growth stage" is where the rail surface roughness of a specific wavelength selectively grows, and the "saturation stage" is when growth in rail surface roughness is inhibited. In the "saturation stage," the wheels of a vehicle can no longer follow rails because of growing roughness and are repeatedly in and out of contact with the rails, resulting in the roughness waveform transforming from sinusoidal to triangular. Simulations confirm that this results in components, that are integral multiples of basic spatial frequency (harmonic components), appearing in the spatial frequency components of the roughness waveform [6], and harmonic components appear in the response of tracks and vehicles [8]. Thus, it is believed that collisions between wheels and rails at the saturation stage result in the actualization of the noise and vibration posing problems during actual operation.

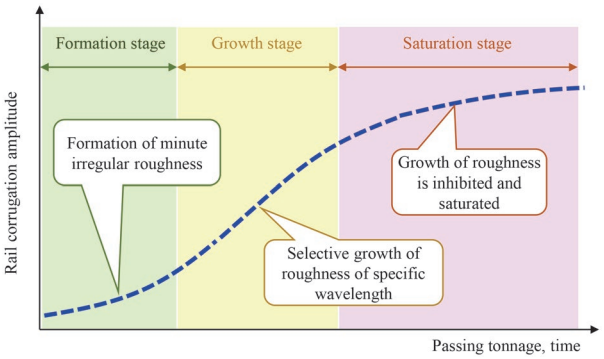

Fig. 2 Model of rail corrugation growth process

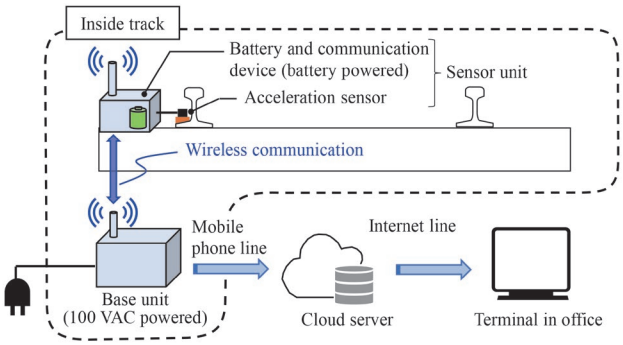

Fig. 3 Outline of measurement system

3. On-site measurement system for rail corrugation

Continuous monitoring of rail vibrations using a wireless acceleration sensor is considered an easy and inexpensive method for evaluating the characteristics of the growth process of rail corrugation described in section 2. Since rail vibrations are actually easy to measure and a consistent relationship is seen with rail corrugation generation, a method for monitoring rail corrugation using rail vibration measurements has previously been proposed [9].

Adopting a wireless acceleration sensor to evaluate the growth process of rail corrugation demands a small-sized unit that can be easily installed on a track, is durable and power-saving, is for long-term continuous measurement, and has a sufficient sampling frequency for the frequency of the vibrations excited by rail corrugation. Based on such observations, in this study, we adopted a wireless measurement system utilized in monitoring the seismic behavior of building structures and building health [10] (Sonas, Inc.: Wireless Vibrations Measurement System x02).

Figure 3 shows an outline of the measurement system. The measurement system consists of a sensor unit (acceleration sensor / battery powered) and a base unit (control and communication device / 100 VAC powered). Table 1 shows the specifications of the sensor unit. Measurement data is stored in recording media built into the sensor unit, and then transmitted from the sensor unit to the base unit by wireless communication. The data compiled in the base unit is transmitted to a dedicated ground server via a mobile phone line, and then can be browsed or downloaded from an information terminal. Furthermore, the measurement system can compile data for a certain period of time before and after the specified measurement period or use the vibrations of a passing train as a trigger. This reduces sensor unit battery consumption.

Table 1 Sensor unit specifications

Acceleration sensor used		Analog devices ADXL357
Acceleration sensor dimensions		40 x 30 x 15 mm
Performance	Measuring axes	3 axes (X, Y, Z)
	Measurement range	±40 G (±392 m/s^2)
	Filter	Low pass filter: 1 kHz High pass filter: DC
	Noise density	80 [μg/√Hz] (If measurement range ±10 G)
Battery / Communication device dimensions		75 x 120 x 100 mm
Battery		D size battery x 5
Performance	Protection class	Equivalent to IP65
	Continuous operating time (approximate)	In case of continuous measurement: 1.5 years In case of using trigger measurement: 6 years
Sampling frequency		Maximum 2 kHz

4. Measurement on commercial lines

4.1 Outline of measurement site

In this study, we performed long-term measurement of rail surface roughness, and of rail vibrations using this measurement system, in a sharp curve on a commercial line where rail corrugation had actually been generated. Rail vibrations were measured using the measurement system during daytime hours when train operation density was low in order to match operating conditions such as train speed, vehicle type, and occupancy rate as much as possible. Furthermore, although rail vibrations are measured every day, in this study, we excluded data continuously measured for a maximum of about eight months from the day after rail grinding impacted by high measurement noise and similar factors, and then selectively analyzed data for about one to two trains per day.

Figure 4 shows an outline of the measurement site. As shown in the figure, the measurement site is in the sharp curve of a commuter line (curve radius R = 185 m, cant C = 105 mm). The track structure consists of two types of ballastless track: coil spring anti-vibration track and direct fastened track with anti-vibration sleepers. The target vehicles were two types of commuter trains with an annual passing tonnage of approximately 19 million tons, and a measurement point train speed of about 40 to 45 km/h. The points for measuring rail vibrations with the measurement system were on the low rail at measurement point A (in the section of coil spring anti-vibration track) and measurement point B (in the section of direct fastened track with anti-vibration sleeper) shown in the figure. Furthermore, a friction modifier [11] was sprayed on the low rail for the purpose of reducing lateral force near measurement point B.

Figure 5 shows an example of the installation of the sensor unit. The figure shows that the acceleration sensor of the sensor unit was fixed with an epoxy adhesive to the bottom of the rail outside the gauge in the middle between the rail fastening systems. The battery and communication device were fixed with an epoxy adhesive on the upper surface of the end of the sleeper near the acceleration sensor. Furthermore, although not shown in the figure, the base unit was installed beneath the platform of a nearby station.

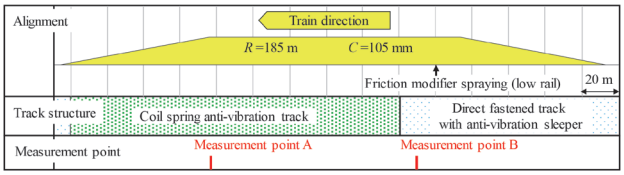

Fig. 4 Outline of measurement site

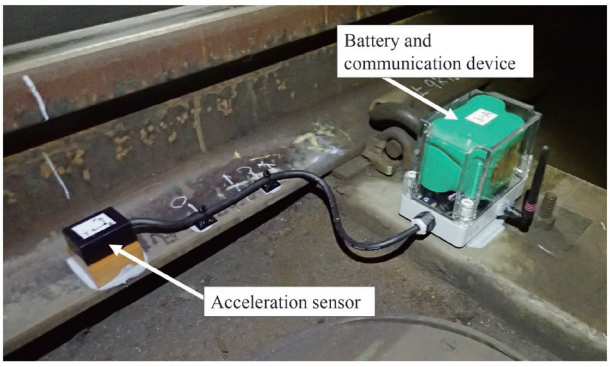

Fig. 5 Sensor unit installation

4.2 Rail surface roughness generation

In order to investigate the generation of rail corrugation near the measurement point of rail vibrations, rail surface roughness was measured at two times with different passing tonnages after rail grinding (approximately 5.05 million tons and 14.03 million tons after rail grinding). To measure rail surface roughness, we used the rail surface roughness continuous measurement trolley [7] developed by the Railway Technical Research Institute shown in Fig. 6.

Figure 7 shows rail surface roughness generation on the low rail of the curve. In addition to the rail surface roughness waveform and a spectrogram of the rail surface roughness waveform, the figure also shows track structure. The rail surface roughness waveform is obtained by subjecting the restored waveform to band pass filter processing with a wavelength of 50 to 200 mm. From the figure, we find that rail corrugation generation differs depending on track structure. Near measurement point A in the section of coil spring anti-vibration track, the rail corrugation amplitude (total amplitude) was about 0.05 mm or less when about 5.05 million tons passed after rail grinding, which increased to about 0.2 mm when about 14.03 million tons passed after rail grinding. However, near measurement point B in the section of direct fastened track with anti-vibration sleeper, no significant increase in amplitude was seen. This is believed to have been influenced by the effects of the aforementioned spraying of friction modifier, in addition to differences in track structure.

The spectrogram in the figure was obtained from a short-term Fourier transform of the restored waveform of rail surface roughness. The spectrogram shown here expresses the magnitude of the power spectral density of the amplitude in color, and shows the magnitude of rail surface roughness, the spatial frequency, and the kilometer information in a unified manner. According to the figure, no dominant spatial frequency component was observed in the spectrogram when about 5.05 million tons passed after rail grinding in the section of coil spring anti-vibration track including measurement point A. However, we found that when about 14.03 million tons passed after rail grinding and rail corrugation amplitude reached about 0.2 mm, a dominant spatial frequency component (① in the figure) was recognized, and rail corrugation of about spatial

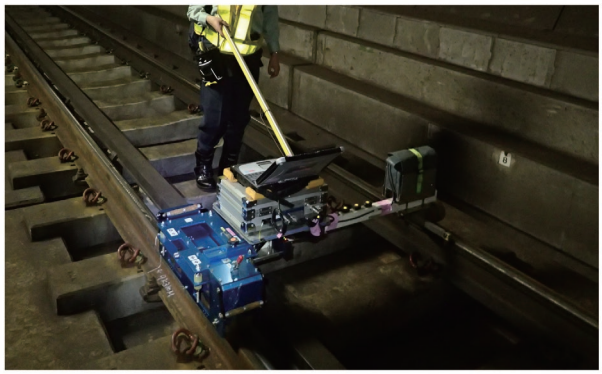

Fig. 6 Measurement with rail surface roughness continuous measurement trolley

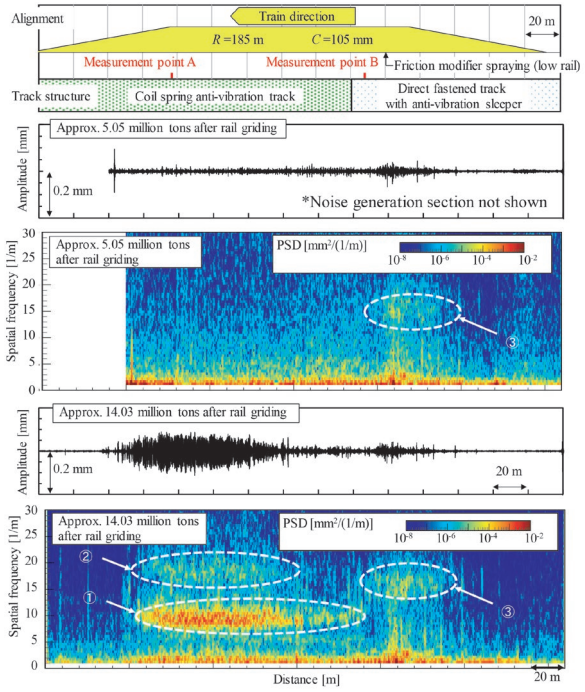

Fig. 7 Rail surface roughness generation (low rail)

frequency 10 [1/m] (wavelength 100 mm) was being generated. In addition, the dominant spatial frequency component near 20 [1/m] in this section (② in the figure) is approximately two times the aforementioned basic spatial frequency of rail corrugation and is believed to be a harmonic appearing at the saturation stage of corrugation [6]. On the other hand, we see that in the section of direct fastened track with anti-vibration sleeper including measurement point B, the component of spatial frequency 18 [1/m] (wavelength 55 mm) increased slightly as the passing tonnage increased after rail grinding (③ in the figure). Thus, differences in the basic spatial frequency of rail corrugation near both measurement points are due to differences in the growth factor of rail corrugation [12] attributable to differences in track structure.

Here, the frequency of vibrations excited by rail surface roughness existing at measurement points is calculated by the following equation.

$$f = \frac{v}{3.6 \times \lambda} \quad (1)$$

Here, f is frequency [Hz], v is train speed [km/h], and λ is the wavelength [m] of rail surface roughness [m]. Accordingly, if we assume that the train speed in this section is 40 to 45 km/h, then it may be assumed that rail vibrations are excited at about 110 to 125 Hz (corresponding to 10 [1/m]) at measurement point A and 200 to 225 Hz (corresponding to 18 [1/m]) at measurement point B due to the aforementioned roughness.

5. Time-dependent changes in vertical rail vibration acceleration

5.1 Acceleration generation

As shown in Table 1, the measurement system measures 3 axes of vibration acceleration in the rail, but in this paper, we focus only on the vertical vibration acceleration of the rail, which shows a characteristic trend. A comprehensive analysis including horizontal vibration acceleration and longitudinal vibration acceleration, can be found in the literature [13].

Figure 8 shows a waveform at measurement point A as an example of the waveform of vertical rail vibration acceleration. This waveform was obtained by subjecting the acceleration waveform recorded by the measurement system to 900 Hz low pass filter processing. In subsequent analysis, the target waveform is 30 seconds including the time when the train passes. In the figure, the time when there is an increase in acceleration amplitude corresponds to the time when the vehicle bogie is passing. The maximum value of total amplitude was less than 50 m/s^2 when about 110,000 tons passed after rail grinding but increased to about 400 m/s^2 when about 13.98 million tons passed after rail grinding.

5.2 Changes in amplitude

The amplitude of vertical rail vibration acceleration is believed to increase in accordance with the amplitude of rail surface roughness. Therefore, we computed the RMS (Root Mean Square), which can serve as an index of the mean amplitude of acceleration waveform and analyzed the changes. Figure 9 shows an example of changes in the RMS of vertical rail vibration acceleration. According to the figure, at measurement point A, the RMS remains at a small level until about 5 million tons after rail grinding, and then increases rapidly. At this time, wheels can no longer follow rail surface roughness, and rail corrugation is presumed to shift from the "growth stage" to the "saturation stage." After passing about 10 million tons after rail grinding, the RMS remained almost constant. Here, as shown in Fig. 7, a harmonic component can be seen in the rail surface roughness waveform measured at this time (when about 14.03 million tons passed after rail grinding), so it is thought the stage at which growth in the roughness is inhibited has been reached. On the other hand, at measurement point B, the RMS increases slightly with increased passing tonnage, but the RMS is small compared to measurement point A, and no clear increasing tendency is seen. This tendency, as shown in Fig. 7, conforms to no clear increase being seen in rail corrugation amplitude in the section of direct fastened track with anti-vibration sleeper. Furthermore, plot irregularities seen in these figures are thought to be influenced by train speed, roughness in the wheel tread, and differences in vehicle type.

5.3 Changes in frequency characteristics

Figure 10 shows an example of the PSD (power spectral density) of vertical rail vibration acceleration measured at times of differ-

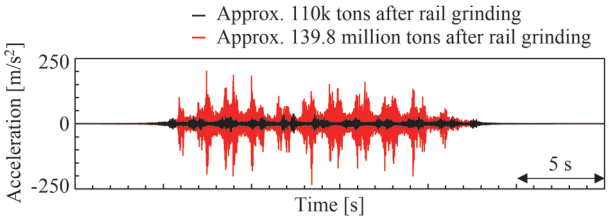

Fig. 8 Example of waveform of vertical rail vibration acceleration (measurement point A)

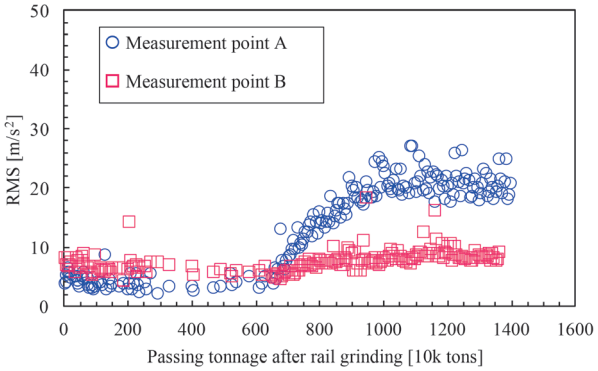

Fig. 9 Example of changes in RMS of vertical rail vibration acceleration

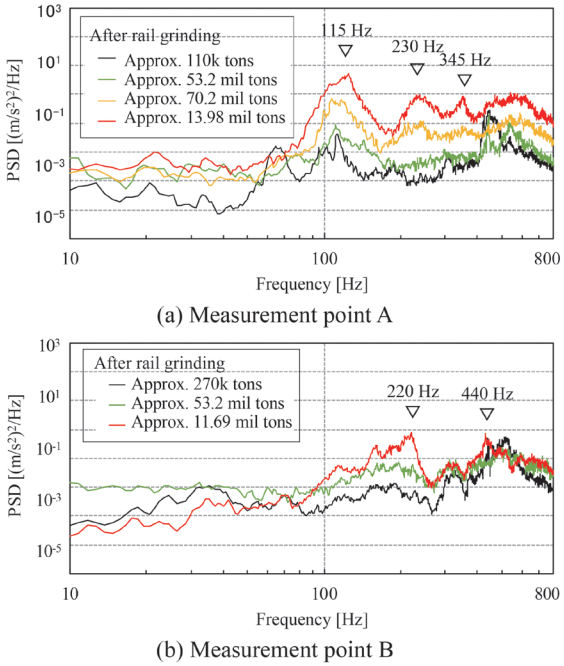

Fig. 10 Example of PSD of vertical rail vibration acceleration

ing passing tonnage after rail grinding. According to Fig. 10 (a), at measurement point A, there is a pronounced increase in power of about 115 Hz, 230 Hz and 345 Hz as passing tonnage increases after rail grinding. If we consider the wavelength of rail surface roughness (about 100 mm) and train speed (about 40 to 45 km/h) in this section, then these conform with the fundamental frequency (about 115 Hz) and harmonic thereof (about 230 Hz, 345 Hz) of vibrations excited by rail surface roughness during train passing. Furthermore,

the peak around 65 Hz seen in the PSD for about 110,000 tons after rail grinding may be a vibration component [14] attributable to the coil spring just below the track slab and minute roughness in the low rail, and the peak near 450 Hz is thought to be a vibration component attributable to periodic traces accompanying rail grinding (hereinafter, rail grinding traces).

According to Fig. 10 (b), at measurement point B, there is a tendency of the 220-Hz band power to increase as passing tonnage increases after rail grinding, but the appearance of a harmonic component (440 Hz) is not clearly seen compared to measurement point A. Furthermore, the gentle peak near 300 to 320 Hz may be derived from the intrinsic vibrations of the vertical vibration system of the track, because its magnitude is roughly the same regardless of the passing tonnage. In addition, the gentle peak near 500 Hz is thought to be attributable to rail grinding traces similar to measurement point A.

In order to evaluate the fundamental frequency of rail vibrations due to rail corrugation growth and the increasing tendency of the harmonic component, we analyzed changes in PSD per frequency band. Here, the frequency bands corresponding to fundamental frequency and harmonic thereof we focused upon were the 115-Hz and 230-Hz bands at measurement point A and the 220-Hz and 440-Hz bands at measurement point B, and we computed the mean value of the PSD in these bands.

Figure 11 shows respective examples of changes in PSD per frequency band of vertical rail vibration acceleration at measurement points A and B. According to Fig. 11 (a), there is a tendency for power to increase in each frequency band from approximately 7 million tons after rail grinding at measurement point A, and the power of the fundamental frequency band (115-Hz band) increases ahead of the second harmonic band (230-Hz band). Here, based on the characteristics of the "saturation stage" according to numerical analysis [8], increased power in the fundamental frequency band in the vertical rail vibration is attributable to increased amplitude in the "growth stage," and increased power in the second harmonic band is attributable to the collision of the rail and wheels when transitioning to the "saturation stage."

According to Fig. 11 (b), at measurement point B, a tendency is seen in which the power of the fundamental frequency band (220-Hz band) increases slightly as passing tonnage increases. However,

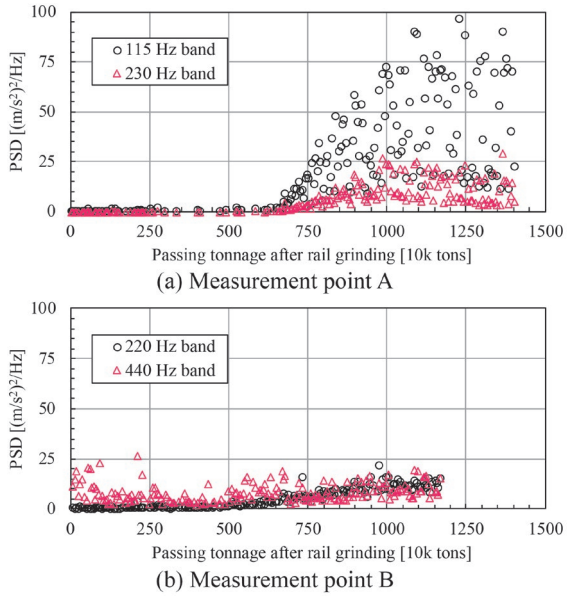

Fig. 11 Examples of changes in PSD per frequency band of vertical rail vibration acceleration

an increasing tendency in the PSD of the fundamental frequency and harmonic band as seen at measurement point A and shown in Fig. 11 (a) is not confirmed. This result conforms with no clear increased amplitude or harmonic being seen in the rail surface roughness waveform in Fig. 7, so it is presumed that the "saturation stage" of rail corrugation is not reached at measurement point B.

Based on the above, vertical rail vibration monitoring is effective in evaluating growth process based upon the characteristics of the "saturation stage" of rail corrugation [6].

6. Evaluation of growth process using vertical rail vibration

So far in this paper up to section 5, constant monitoring of vertical rail vibration has been considered effective in evaluating the growth process of rail corrugation. Therefore, we use the measurement results at measurement point A to discuss the correspondence between changes in the RMS of vertical rail vibration acceleration and the growth process of rail corrugation.

Figure 12 shows an example of the relationship between the RMS of vertical rail vibration acceleration at measurement point A and the mean value of the PSD of the second harmonic band. From the figure, if we consider that a harmonic component appears in vertical rail vibration when the "saturation stage" of rail corrugation is reached, then it may be inferred that the period where the RMS is small and no harmonic component is seen (before approximately 5 million tons after rail grinding) corresponds to the "formation stage," the period where the RMS starts to increase very gradually and no harmonic component is seen (approximately 5 to 7 million tons after rail grinding) corresponds to the "growth stage," and the period where the RMS increases rapidly and a harmonic component appears (from approximately 7 million tons after rail grinding) corresponds to the "saturation stage." However, since the boundary between the formation stage and the growth stage is not clear, further verification is still required.

Thus, using the measurement system adopted in this study to measure vertical rail vibration acceleration, and monitor changes in PSD per frequency band corresponding to the RMS and the wavelength of rail corrugation, resulted in the prospect of being able to evaluate the growth process of rail corrugation, specifically the transition from the growth stage to saturation stage.

It is assumed that the method for evaluating rail corrugation growth developed here may be used in evaluating the growth tendency of rail corrugation at individual sites and the effects of countermeasures, in predicting the remaining period until rail grinding is required and the rail grinding cycle, in evaluating the finished

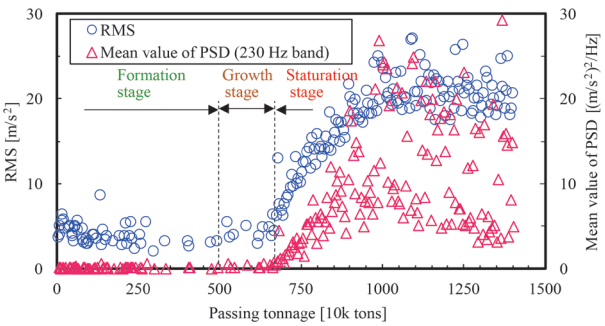

Fig.12 Example of relationship between RMS of vertical rail vibration acceleration and mean value of PSD (measurement point A)

rail grinding, and in supporting scheduling of rail grinding based on amplitude estimates. Being able to evaluate when the "saturation stage" occurs, which is when noise and vibrations are actualized, will be beneficial to actual operations. A data analysis method is required in order to realize the above uses, and the plan is to build one and verify it through field measurements.

7. Conclusion

In this study, we investigated a method to constantly monitor rail vibrations and evaluate the growth process of rail corrugation using a measurement system constructed with a battery-powered acceleration sensor and wireless sensor network. The obtained findings are shown below:

(1) Based on the results of long-term measurement using a measurement system in a sharp curve of a commercial line where rail corrugation had been generated, findings were seen in which the RMS of vertical rail vibration acceleration and the PSD per frequency band corresponding to the wavelength of rail corrugation remained small for a certain period of time after rail grinding, but then increased rapidly and reached saturation.

(2) We confirmed that power increases in order of the fundamental frequency and harmonic band of rail corrugation during the period that the RMS of rail vertical acceleration and the PSD per frequency band corresponding to the wavelength of rail corrugation rapidly increased. This tendency was thought to be an observation of rail corrugation transitioning from the "growth stage" to "saturation stage."

(3) According to (1) and (2), constant monitoring of vertical rail vibration appeared effective in evaluating the growth process of corrugation. In addition, this resulted in the prospect of being able to evaluate the growth process of rail corrugation and the period until the saturation stage is reached.

The future plan is to verify the relationship between the degree of rail corrugation growth and vertical rail vibration acceleration based upon data from regular measurements of rail surface roughness. The plan is also to construct a method for ascertaining the impact of track structure and differences in vehicles and operating conditions upon evaluation of the growth process of rail corrugation, and then automatically determine when the saturation stage has been reached.

References

[1] Grassie, S. L. and Kalousek, J., "Rail corrugation: Characteristics, causes and treatments," *Proc. IMechE, Part F*, Vol. 207, pp. 57-68, 1993.

[2] Matsumoto, A., Sato, Y., Ono, H., Tanimoto, M., Oka, Y. and Miyauchi, E., "Formation mechanism and countermeasures of rail corrugation on curved track," *Wear*, Vol. 253, Issues 1-2, pp. 178-184, 2002.

[3] Manabe, K., "A hypothesis on a wavelength fixing mechanism of rail corrugation," *Proc. IMechE, Part F*, Vol. 214, pp. 21-26, 2000.

[4] Suda, Y., Hanawa, M., Okumura, M., et al., "Study on rail corrugation in sharp curves of commuter line," *Wear*, Vol. 253, pp. 193-198, 2002.

[5] Tanaka, H. and Miwa, M., "Modeling the development of rail corrugation to schedule a more economical rail grinding," *Proc. IMech E, Part F*, Vol. 234(4), pp. 370-380, 2020.

[6] Aboshi, M., and Tanaka, H., "Dynamic characteristics and growth curve of rail corrugation at saturation stage," *Transactions of the JSME*, Vol. 87, No. 898, 2021, DOI: 10.1299/transjsme.21-00017 (in Japanese).

[7] Tanaka, H. and Shimizu, A., "Practical application of portable trolley for the continuous measurement of rail surface roughness for rail corrugation maintenance," *Quarterly Report of RTRI*, Vol. 57, No. 2, pp. 118-124, 2016.

[8] Aboshi, M., and Tanaka, H., "Simulation analyses of progress process of rail corrugation," *Transactions of the JSME*, Vol. 85, No. 878, 2019, DOI: 10.1299/transjsme.19-00051 (in Japanese).

[9] Yonehara, Y., Tanimoto, M., et al., "Development of the rail corrugation detecting system considering the observation of rail vibration and acting force in sharp curve," *Proceedings of J-RAIL 2019*, JSCM-2-3, pp. 146-149, 2019 (in Japanese).

[10] Suzuki, M., Nagayama, T., "Structural monitoring using concurrent transmission flooding," *Transactions of the Institute of Electronics, Information and Communication Engineers B*, Vol. J100-B, No. 12, pp. 952-960, 2017, DOI:10.14923/transcomj.2017ASI0002 (in Japanese).

[11] Ban, T., Fukagai, S., et al., "Development of the Track Friction Moderating System to Low-rail of Sharp Curves," *RTRI Report*, Vol. 26, No. 12, pp. 35-40, 2012 (in Japanese).

[12] Aboshi, M., and Tanaka, H., "Growth Mechanism and Evolution Process of Rail Corrugation," *Quarterly Report of RTRI*, Vol. 62, No. 1, pp. 55-60, 2021.

[13] Kajihara, K. and Tanaka, H., "Vibration-based monitoring method for identifying the growth process of rail corrugation," *Journal of Railway Engineering of JSCE*, No. 26, pp. 33-40, 2022 (in Japanese).

[14] Tanaka, H., and Hosoda, M., "Influence evaluation of track supporting stiffness given to occurrence situation of high rail corrugation using multi-body dynamics," *Journal of Railway Engineering of JSCE*, No. 20, pp. 29-36, 2016 (in Japanese).

Authors

Hirofumi TANAKA, Dr. Eng.
Senior Researcher, Track Maintenance and Geometry Laboratory, Track Technology Division
Research Areas: Track Maintenance, Rail Corrugation Management, Signal Processing

Kazuhiro KAJIHARA
Researcher, Track Maintenance and Geometry Laboratory, Track Technology Division
Research Areas: Track Maintenance

Methods for Applying Public Communication Lines to Communication-based Train Control Systems

Takayasu KITANO **Akihiro GION**
Train Control Systems Laboratory, Signalling and Operation Systems Technology Division

A method for applying public communication lines to communication-based train control systems is proposed. Applying public communication lines to train control systems differs from when applying them to conventional systems in that transmission lines which cannot be controlled by railway operators, intervene between safety devices. Therefore, this paper presents a configuration where train control function and information transmission are independent of each other in order to build a system which meets safety critical requirements without depending on transmission lines. This paper also presents threats posed by information transmission functions from the perspective of the train control function and countermeasure requirements, as well as implementation methods which meet these requirements using current techniques.

Key words: *communication-based train control (CBTC), public communication line, security, system configuration*

1. Introduction

With a declining population, it may become difficult in future for railway operators to source sufficient labor to maintain and preserve their equipment. Under these circumstances, technological developments are expected to help reduce the amount of ground equipment which needs to be maintained. One system that is expected to reduce the amount of safety equipment needed on the ground, is communication-based train control (CBTC), which is already being deployed [1], using advanced on-board equipment and wireless track-to-wayside information transmission. However, while conventional CBTC systems reduce the amount of ground equipment based on conventional technology, such as track circuits, they also require additional transmission equipment to transmit control information between the ground and the train, and increase the number of functions in on-board equipment. In some cases, the system as a whole may not necessarily reduce the amount of equipment, depending on the conditions of the line section where the system is introduced. In order to further reduce the amount of ground equipment to be maintained and managed by railroad operators, it is expected that general-purpose technologies widely used in other fields will be applied to safety equipment. In particular, the application of general-purpose communication lines such as public communication lines for the transmission of control information between the track and the train in CBTC systems, can reduce the need for dedicated radio equipment such as base stations and antennas, and save maintenance labor. Therefore, in this paper, we propose a method for constructing CBTC systems whose communication network does not depend on either a dedicated private communication line or a public communication line. We define the concept of ensuring security when public communication lines are used for CBTC systems, and propose a procedure for developing such a system, including the determination of requirements for communication lines, and a method for implementing security.

2. Concept of applying a public communication line

2.1 Outline of CBTC

(1) Outline

An overview of a CBTC is shown in Fig. 1. In this system, control information is transmitted between the ground and on-board equipment by radio, the train position is detected on-board, and the on-board equipment takes the initiative in controlling the train, thereby realizing flexible train operation and reducing the amount of ground equipment involved in operational safety [2]. The important functions of the system are: correct recognition of the train position by the on-board equipment; correct transmission of the train position, recognized by the on-board equipment, to the ground equipment; configuration of the route and setting of the movement authority, according to each train position, by the ground equipment; transmission of the set movement authority to the on-board equipment; creation of brake profiles according to the transmitted information. The ground equipment is responsible for configuring the

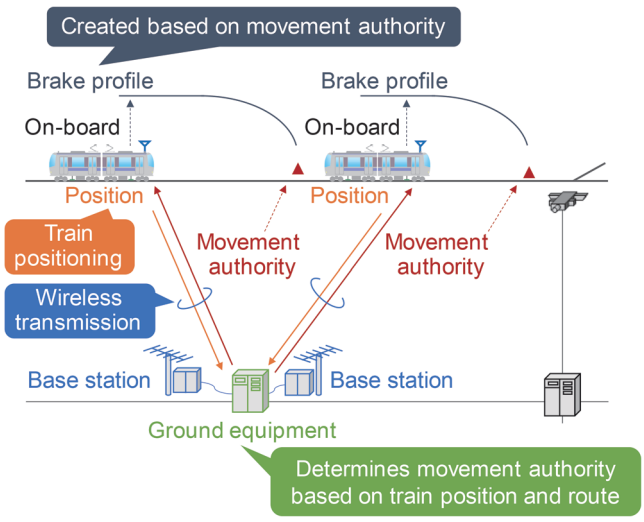

Fig. 1 Outline of CBTC system

route and setting the movement authority according to the positions of each train, communicating the set movement authority to the on-board equipment and controlling the train according to the transmitted information.

(2) Issues in reducing ground equipment

CBTC systems developed in Japan use dedicated private communication lines for information transmission between the ground and on-board equipment. Such conventional systems reduce the amount of safety equipment needed on the ground, but require transmission equipment to establish the private communication lines. As such, they do not necessarily reduce the overall amount of equipment actually used. For example, conventional systems use track circuits for train detection, whereas in CBTC systems, on-board equipment transmits the train position to ground equipment. In such cases, track circuits are not required, but new transmission equipment needs to be installed along the wayside. On low density lines, such as regional lines, there is more wayside equipment to be maintained relative to the number of trains, which increases the burden of maintenance.

2.2 Concept of system development applying public communication line

(1) Safety assurance

In CBTC systems, mechanisms are needed to ensure safety, such as stopping the train, even when information transmission between the ground and on-board equipment is not correct. As shown in Fig. 2, both ground and on-board equipment have mechanisms to check that the messages sent and received and the equipment to which they are sent are legitimate, and to stop the train if an abnormality is detected.

(2) Ensuring stable train operation

As mentioned in the previous section (1), when the train stops in the event of a transmission error, the train will stop every time the information transmission is not correct, disrupting train operations. Therefore, to ensure operational stability, two possible approaches can be adopted: (i) the use of high-quality transmission, or (ii) the design of train control systems that can be used even with unstable transmissions. CBTC systems currently in operation, which use dedicated private communication lines in order to adopt the approach described in (i). If a system uses public communication lines, it is necessary to determine the functions required to ensure safety, assuming that the communication equipment cannot be equipped with dedicated safety functions. This paper thus describes a method for applying public communication lines to train control systems, with a focus on ensuring safety.

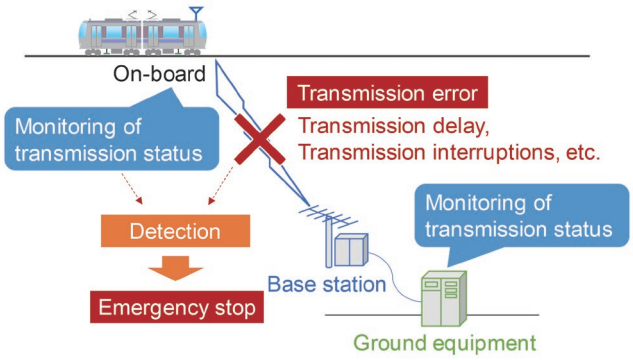

Fig. 2 Example of safety control for transmission error

(3) Issues involved in applying public communication lines

Equipment used in conventional train control systems, including the transmission equipment, has been developed for fail-safe operation based on defined safety conditions, whereas transmission devices for public communication lines have not. Therefore, when using public communication lines, it is necessary to implement measures based on IEC 62280 [3], assuming that non-fail-safe transmission devices intervene between safety devices. Therefore, in addition to conventional safety technologies, countermeasure technologies against attacks on safety by malicious third parties are important. It is necessary to have mechanisms to ensure the fail-safe role of safety equipment, independent of the transmission device, so that the safety equipment can operate in fail-safe mode even if information transmission between the safety devices is like a black box.

3. Application of public communication lines to train control systems

3.1 Procedure for determining the configuration of train control systems

Before drafting specifications, it is necessary to determine the basic functions required in the ground and on-board equipment in the train control system. The following procedure is proposed, as part of the system configuration, to determine the functions and actions of the train control system based on the purpose of introducing the system and the operating conditions of the line, and to apply elemental technologies such as train detection.

(1) System introduction policy

The most effective way to reduce the cost of using public communication lines is to use existing equipment as much as possible without modification. On the other hand, if a public communication line is applied as it is, some operational tasks such as restoration in case of breakdowns or anomalies may no longer be possible. Therefore, the direction in which the system should be structured is either to maintain the conventional operation by improving the existing equipment, even if the cost is relatively high, or to reduce the costs by changing the operation. These policies are related to the functions to be allocated to the ground and on-board equipment and have a significant impact on the final system development and implementation process, and should be decided before the specific train control and train detection methods are decided.

(2) Determination of train control system

The operations and tasks that cannot be changed due to the specific circumstances of the line sections where they are to be introduced shall be identified in advance, and the train control functions required to satisfy these requirements shall be determined. It is particularly important to identify the operational requirements. Once the functions have been determined, the functions to be allocated to the ground and on-board equipment shall be determined based on the train operation, maintenance, and renewal equipment.

(3) Determination of train detection system

In CBTC systems, train detection uses train position detected by on-board equipment, but the functional allocation of the train positioning technology and the train detection function shall be taken into account. The specific allocation of train detection functions to on-board and the ground equipment has to be determined taking into account the operational requirements of the introduced line sections extracted in the previous section (2) and the specific train control functions. Furthermore, it is necessary to determine the accuracy of the position recognition required to satisfy the train control system functions and to adopt compatible technology.

(4) Selection of communication network

The communication network responsible for the transmission of information between ground equipment and on-board equipment is selected by determining the requirements after the functions of train control and train detection have been defined. The determination of the requirements for their selection is described below in Section 3.3. Based on (1) to (4), the configuration of the CBTC system can be determined.

3.2 Configuration of train control systems

Development of transmission equipment used in public communication lines does not assume a fail-safe application and cannot be equipped with safety-related functions. Therefore, it is not possible to replace only the transmission equipment and use the same configuration as current CBTC systems: system configuration needs to be reviewed [4]. We therefore propose a train control system configuration that clearly separates the functions related to the safety of train operation (safety function) from the functions related to the transmitting of information (transmission function), thereby eliminating the dependency between the two functions (Fig. 3). In this configuration, in the transmission of messages between the ground and on-board equipment, which is the safety equipment, the functions of the ground and on-board equipment alone can ensure safety and security, without depending on the information transmission function.

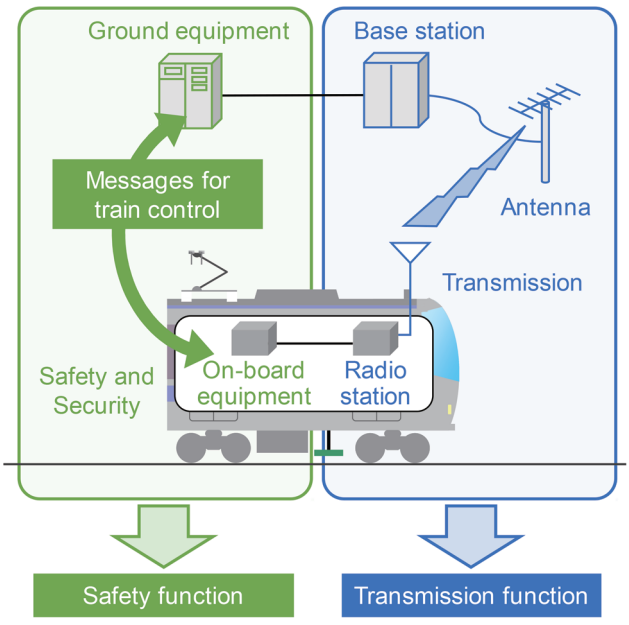

Fig. 3 Configuration of train control systems

3.3 Determining the requirements for the transmission system

It is important that the information needed to fulfil the safety-related functions can be reliably transmitted between ground and on-board equipment. Based on the requirements of the control equipment needed to fulfil the functions of the train control system and the operating conditions of the line, the amount of information, the transmission cycle, and the transmission quality (error rate, delay time) of the information needed between the equipment are defined as requirements. A transmission system that meets these requirements is used (Fig. 4). This method also corresponds to the procedure defined in IEC/TS 62773. Generalizing the transmission system by focusing on safety-related functions as shown in Fig. 5 facilitates the extraction of functions required for safety-side control and the definition of requirements for the transmission system.

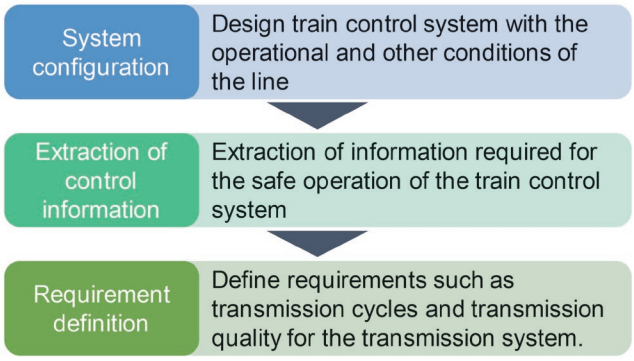

Fig. 4 Procedure for determining requirements for transmission systems

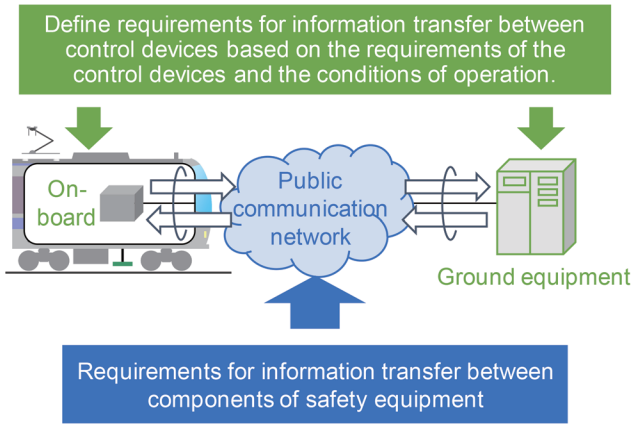

Fig. 5 Approach to determining requirements for transmission systems

4. Security measures when applying public communication lines

4.1 Threats to and requirements for transmission systems

(1) Cyber attacks

Threats to transmission systems can be categorized into cyber-attacks such as spoofing, tampering, and Denial of Service (DoS) attacks. In spoofing, spoofing of the other device and replay attacks are assumed. Spoofing of a remote device is the act of pretending that an external third party is one of the devices in the system. A replay attack is an attack in which an external third-party records messages sent by devices within the system and resends the same messages that were sent in the past at different timings. Tampering is the rewriting of information through the intervention of a third party in the process of sending or receiving messages. A DoS attack is an attack that impedes normal operation by sending a large amount of irrelevant information to the target device. The attacked device will process many transmitted messages, and there is a possibility that the processing will be delayed or that it will behave abnormally.

(2) Threats to transmission systems

IEC 62280 has been standardized as an international standard for safety-related transmissions and defines seven threats (Repetition, Deletion, Insertion, Re-sequencing, Corruption, Delay, Masquerade). These can be organized in terms of threats to the input information of on-board or ground equipment as security devices, as shown in Table 1.

(3) Countermeasures against third-party threats

Threats to the transmission systems of train control systems include "unintentional errors" caused by naturally occurring factors such as noise and "intentional errors" caused by external malicious third parties. In current train control systems, measures have been implemented according to the definition of IEC 62280. For unintentional errors, verification of messages based on sequence numbers, time stamps and safety codes and detection of transmission interruptions are used. Against intentional errors, measures focusing on confidentiality are implemented by encrypting. When public communication lines are used, verification against intentional errors is particularly important. In this regard, methods for verifying authenticity and integrity are the most promising: authenticity indicates that the device from which the information is transmitted is the correct party, and integrity verifies that the information is accurate and up-to-date (Fig. 6).

Therefore, the attack categories for intentional errors, threats to security and their countermeasures are listed in Table 2. For spoofing, the threat is the "input of incorrect information" from another device impersonating the transmitting device, which induces dangerous behavior. Countermeasures can be taken against this by verifying the authenticity of the transmitted messages. Replay attacks can be dangerous because the message itself is the same as the one transmitted between devices in the system, and the device receiving the message sent for the purpose of a replay attack will misidentify the current state and operation. In this case, both "input information contains delays" and "incorrect information is input" are threats. For tampering, the threat is "incorrect information being entered" for DoS attacks, "information disruption" and "transmission delays" occur as a result of the enormous amount of processing involved in a large number of messages. Also, when large amounts of random information are transmitted, there is a possibility of "incorrect information being entered." Against replay attacks, tampering and DoS attacks, measures can be taken by verifying the integrity of the transmitted messages. As described above, it is effective to take countermeasures against attacks from third parties based on authen-

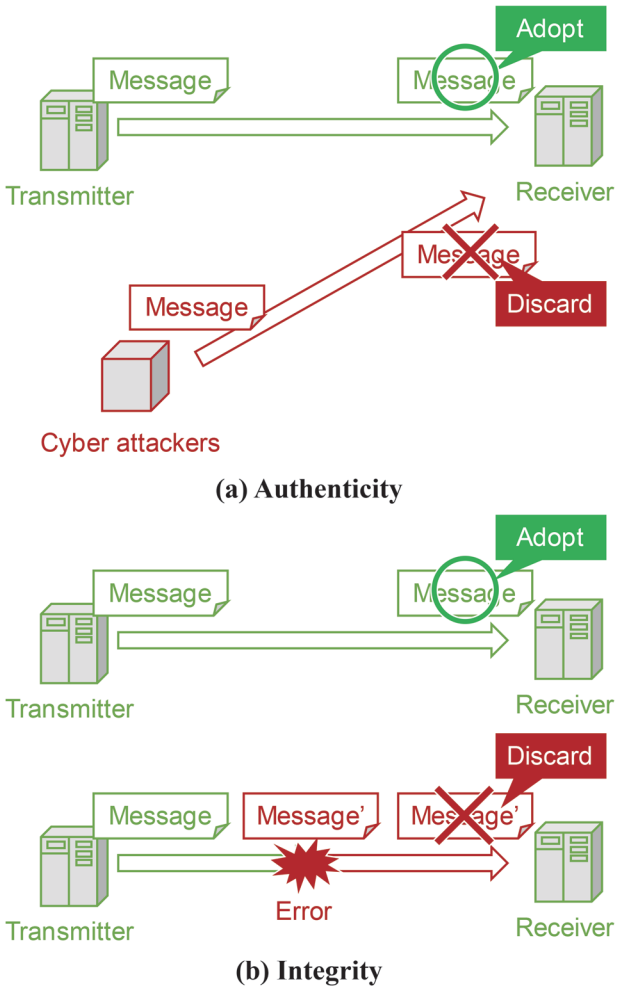

Fig. 6 Authenticity and integrity of messages

Table 1 Impact of threats on the transmission system to inputs of safety equipment

	Repetition	Deletion	Insertion	Re-sequencing	Corruption	Delay	Masquerade
Incorrect input	✔	✔	✔	✔			✔
Information interrupted					✔		
Input delay						✔	✔

ticity and integrity. When applying public communication lines to train control systems, it is important to design the system after checking that the safety control function has implemented the measures listed in Table 2.

4.2 Proposed countermeasures against threats

(1) Application of message authentication

Message authentication is an effective way of verifying the authenticity of the counterpart device and the integrity of the information. This is a technique used in anti-tampering measures, where a verification code (MAC) corresponding to a message is generated from a cryptographic key, and the message tampering by a third party is detected by hiding the cryptographic key. However, the MAC generation process is based on computational security, in which the security of a cipher is ensured by the complexity of the time required for analysis according to the processing performance, so the processing load is high and it is difficult to implement on current fail-safe CPUs. In addition, cryptographic techniques such as those used in message authentication have a fast life cycle and it is desirable to have a configuration where only the relevant functions can be replaced. Therefore, it is conceivable to assign the verification code generation process to a non-failsafe module with fast processing speed, but if the non-failsafe module is not operating normally, tampering cannot be detected and the control may be dangerous. Based on this, we propose a method in which the verification code generation is processed by the non-failsafe module and the correctness of the processing performed by the non-failsafe module is verified by the fail-safe CPU (Fig. 7).

(2) Advantages and considerations of the proposed configuration

Although the life cycles of security devices for railway signalling and transmission devices used in public communication lines are different, the combination with a general-purpose non-fail-safe module facilitates the response to updates in information security technology. However, when transmitting security information using public communication lines, it is important to consider the safe side behavior of the system as a whole, including the analysis and extraction of items to be verified by the fail-safe modules installed in the safety equipment.

5. Summary

This paper proposes a method for applying public communication lines to CBTC systems. It differs from current train control systems in that it uses uncontrollable transmission equipment and communication networks to transmit information between pieces of safety equipment. Therefore, we proposed a system configuration in which the safety functions and transmission functions are functionally independent. By separating the functions, the train control sys-

Table 2 Cyber-attack methods in transmission systems

	Spoofing		Tampering	DoS attacks	
	Spoofing	Replay attack		Interruption	Mass messages
Incorrect input	✔	✔	✔		✔
Information interrupted				✔	
Input delay		✔		✔	
verifying	Authenticity	Integrity			

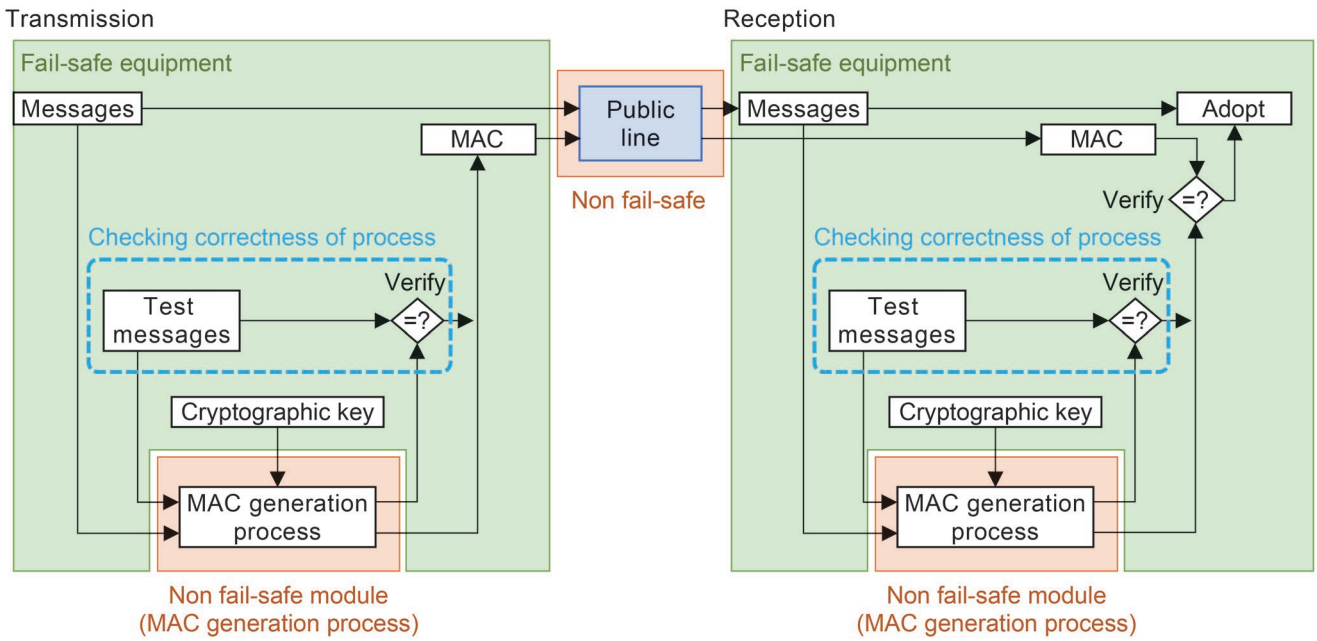

Fig. 7 Processing and verification in message authentication

tem that does not depend on communication networks can be configured. This paper also presents third-party threats to the system and the requirements for countermeasures which would need to be applied when using public communication lines. Finally, this paper proposes a configuration that meets these requirements at the current technological level. Future work will focus on the drafting of specifications and construction of a prototype of the system with a view to bringing this train control system, which uses a public communication line, into practical use.

References

[1] Yamaguchi, T. and Yagi, K., "Adoption of Wireless Advanced Train Administration and Communications System (ATACS)," *Japanese Railway Engineering*, Vol. 51, No. 2, pp. 10-12, April 2017.

[2] Kitano, T., "Radio-based train control," *RRR*, Vol. 73, No. 4, pp. 28-31, 2016 (in Japanese).

[3] IEC 62280:2014: Railway applications-Communication, signalling and processing systems-Safety related communication in transmission systems, 2014.

[4] Kitano, T., "Utilization and Perspective of Radio Communication Technology for Train Control Systems," *Technical report of IEICE*, Vol. 119, No. 244, pp. 45-50, 2019 (in Japanese).

Authors

Takayasu KITANO, Ph.D.
Senior Researcher, Train Control Systems Laboratory, Signalling and Operation Systems Technology Division
Research Areas: Communication-based Train Control System, Wireless Communication System

Akihiro GION
Senior Researcher, Train Control Systems Laboratory, Signalling and Operation Systems Technology Division
Research Areas: Signalling Systems, Safety Engineering

Roller-rig Test of Instrumented Wheelset Utilizing Shear Strains on Wheel Web

Takatoshi HONDO
Vehicle Mechanics Laboratory, Railway Dynamics Division

Instrumented wheelsets are widely utilized in the railway industry to measure wheel-rail interaction force. In a conventional instrumented wheelset, the measurement accuracy of the lateral force is reduced due to the bending moment induced by the wheel load. The author has proposed a new configuration for an instrumented wheelset to reduce the influence of the wheel load on the measurement of the lateral force. This proposed configuration utilizes the shear strains of a wheel web as a measure of the lateral force. This paper describes the accuracy verification of the proposed configuration under a wheel rotating condition. Tests using a single-wheelset roller-rig were carried out and the test results show that the proposed method can reduce the influence of the wheel load even under a rotating condition.

Key words: *running safety, measurement of wheel-rail interaction force, derailment quotient, 3-axis strain gauge, bending moment*

1. Introduction

Measurement of a wheel load and lateral force between wheels and rails is important for assessing running safety and evaluating the curve passing performance of railway vehicles. A wheel load (P) is the vertical force that acts between a wheel and a rail, and lateral force (Q) is the force in the lateral direction. The value Q/P obtained by dividing the lateral force by the wheel load is known as the derailment quotient and is used as an indicator for evaluating running safety. One method for measuring wheel loads and lateral forces continuously when vehicles travel on actual tracks, is to use an "instrumented wheelset" (Fig. 1) which has multiple strain gauges on a wheel surface [1]. Although there are several ways to construct an instrumented wheelset, the common measurement principles in instrumented wheelsets used in Japan are as follows: the wheel load is measured using the vertical strain generated on the side surface of holes, and the lateral force is measured using the bending strain on the side surfaces of wheels [2, 3].

In the lateral force measurement method using the bending strains (hereinafter referred to as the 'conventional method'), when a contact position between a wheel and a rail moves in the lateral direction, measurement accuracy may decrease due to the influence of the bending moment induced by the wheel load (Fig. 2). Specifically, the measured lateral force of wheels on the outer rail side of a curve, which come into contact near the flange while passing through a curve, may exceed the real force due to the influence of the wheel load. This sometimes leads to an assessment that is harder than the reality. In previous work, the author proposed a novel method for measuring lateral force that utilizes the shear strains of a wheel web and it was confirmed that the proposed method is less affected by the wheel load than the conventional method through finite element analyses and static load tests [4]. In this paper, roller-rig tests were carried out to verify the proposed method under a wheel rotating condition.

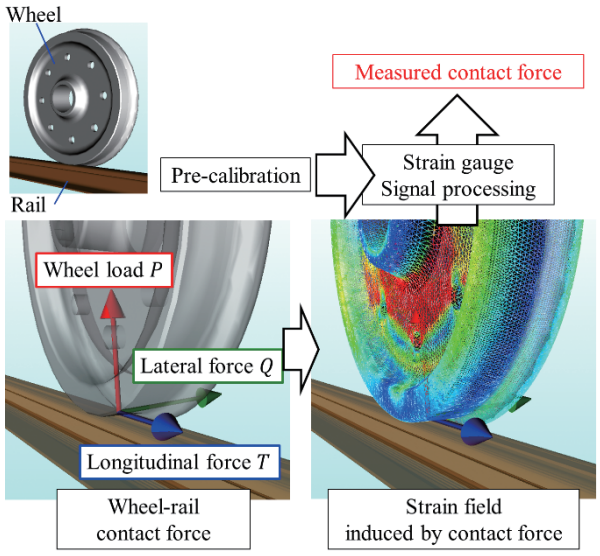

Fig. 1 Principle of measuring wheel-rail contact forces using instrumented wheelset

2. Instrumented wheelset utilizing shear strains on wheel web

2.1 Configurations of bridge circuit

The configurations of the bridge circuits of the proposed meth-

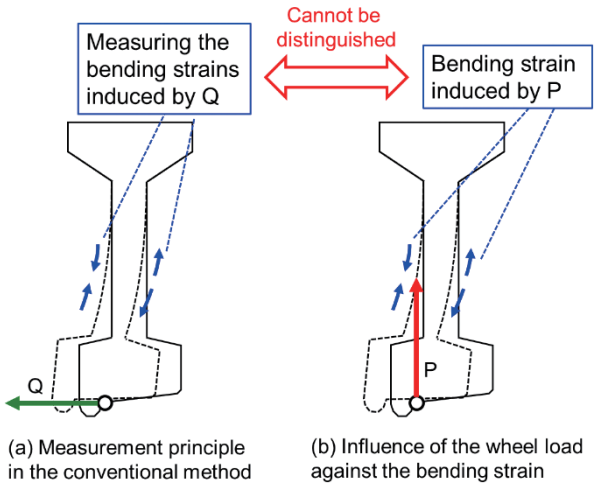

Fig. 2 Mechanism of reducing measurement accuracy of lateral force due to wheel load

od for measuring lateral force are shown in Fig. 3. In this method, 3-axis strain gauges, which are generally used for rosette analyses, are attached where strain gauges for measuring the wheel load are attached, and shear strains are simultaneously measured with vertical strains. The vertical strains are used as a measure of the wheel load. On the other hand, the concept of the proposed method is to measure the shear strains with remaining two orthogonal strain gauges and use them as a measure of the lateral force.

2.2 Approximation of static sensitivity as analytic functions

Static load tests were carried out to calibrate the instrumented wheelset before rolling tests. The conditions of the static load tests are as follows:

- Lateral force loading: A lateral force was applied to 32 points in the circumferential direction of the wheel from the back surface of the wheel.
- Wheel load loading: A vertical force was applied to 32 points in the circumferential direction and three points in the lateral direction (96 points in total on the wheel tread).

The results of the above static load tests were arranged for each loading position as bridge output per unit load, that is, the sensitivity of bridge output. The bridge circuits of the conventional method were also configured to compare the two methods (Fig. 4). The bridge circuits for measuring the wheel load are configured using the method proposed by Ishida et al [2].

The characteristics of sensitivity of the proposed and conventional methods are shown in Fig. 5 when the lateral force is applied in each circumferential position. The proposed method reduces the sensitivity to the lateral force to about 1/3 of that of the conventional method. On the other hand, both the conventional method and the proposed method have the same periodic characteristics of sensitivity as shown in the figure. The output sensitivities of the bridge circuits for the lateral force measurement, qs1 and qs2, are expressed by the periodic function $h(\phi)$:

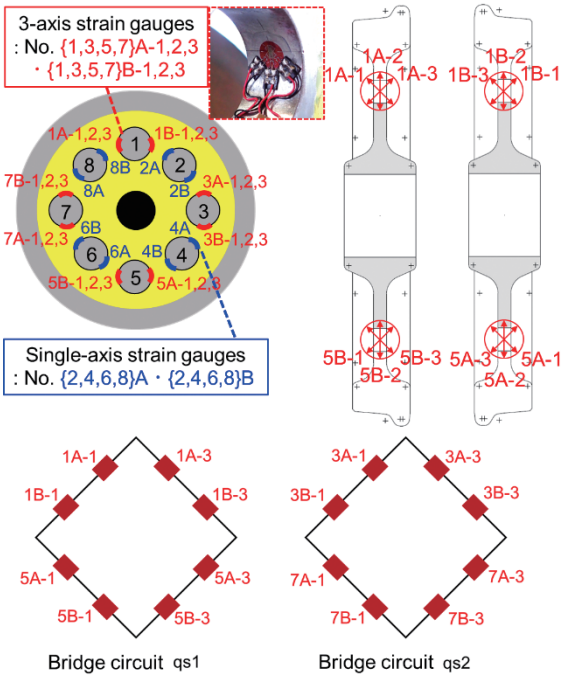

Fig. 3 Configuration of bridge circuits in the proposed method

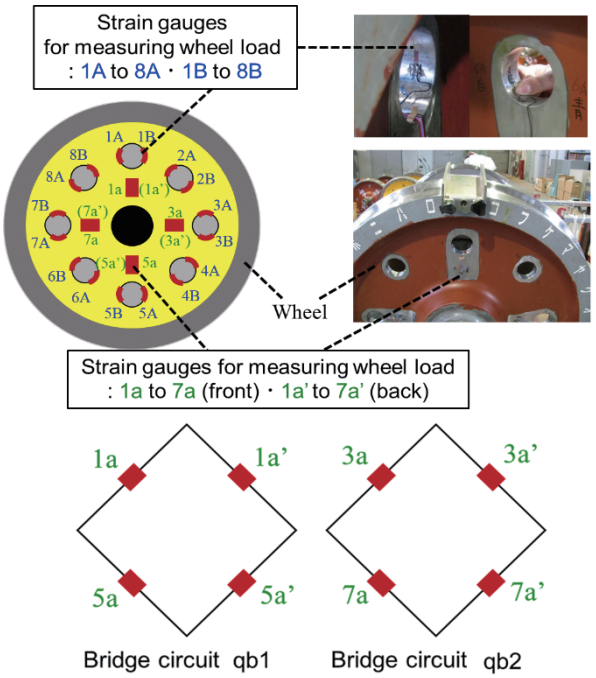

Fig. 4 An example of configuration of bridge circuits in the conventional method

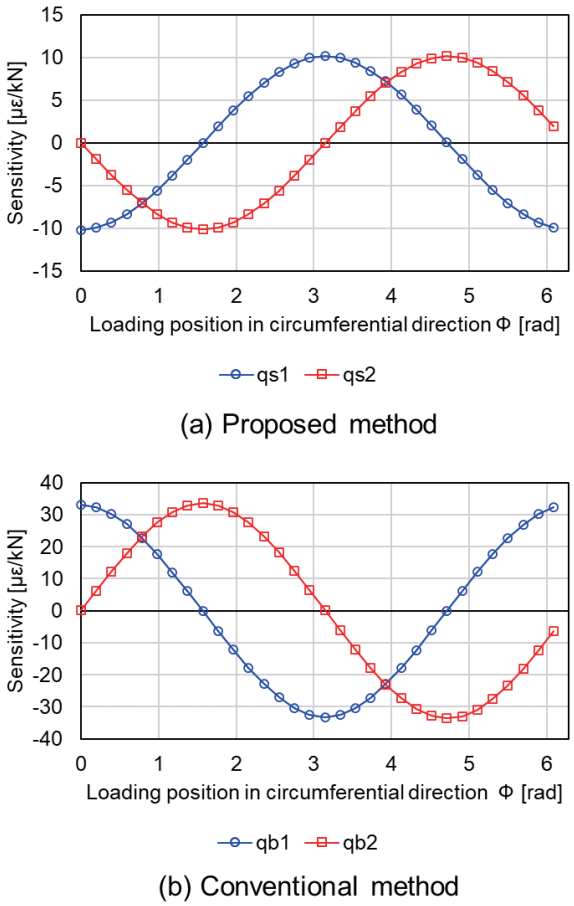

Fig. 5 Characteristics of sensitivity with respect to the lateral force in the proposed and conventional methods

$$h(\phi) = \sum_{n=1}^{D} (S_n^{\mathrm{H}} \sin n\phi + C_n^{\mathrm{H}} \cos n\phi) \tag{1}$$

where S_n^{H} and C_n^{H} are the Fourier coefficients, which are determined by using a least square method with the results of calibration test, and D is the maximum order of the Fourier series. In this investigation, D was set to 11 empirically. This expression of sensitivity can also be applied to the conventional method.

Unlike the lateral force sensitivity, the cross-sensitivity, which is the output sensitivity appeared in the bridge circuit for measuring lateral force when a wheel load or longitudinal force is applied, depends not only on the loading position in the circumferential direction ϕ, but also on the lateral position y. To express such characteristics, a function $f(\phi, y)$ is introduced as follows:

$$f(\phi, y) = y \sum_{n=1}^{D} (S_n^{\mathrm{F}} \sin n\phi + C_n^{\mathrm{F}} \cos n\phi) + \sum_{n=1}^{D} (R_n^{\mathrm{F}} \sin n\phi + B_n^{\mathrm{F}} \cos n\phi) \tag{2}$$

This function is a combined function of the linear function and the Fourier series. The output strain ϵ can be approximated as Eq. (3) using Eq. (1) and Eq. (2), when the contact positions (ϕ, y), applied wheel load P and applied lateral force Q are given.

$$\epsilon \approx Qh(\phi) + Pf(\phi, y) \tag{3}$$

The parameters of the function $f(\phi, y)$ are also determined using a least square method; in the case of the bridge circuits, qs1 and qb1, implemented on the wheelset used for this investigation, the parameters were identified as shown in Table 1. As a reference, Fig. 6 shows a plot of the function $f(\phi, y)$ as a two-variable function.

Table 1 Fourier coefficients identified by static load tests

n	S_n^{H}	C_n^{H}	S_n^{F}	C_n^{F}	R_n^{F}	B_n^{F}
	Bridge circuit qb1					
1	-0.01496	32.68030	0.00113	0.10622	0.00990	-0.11826
2	-0.01000	-0.00928	-0.00004	-0.00053	-0.02189	-0.00840
3	0.00276	0.41712	-0.00013	-0.00185	0.00098	0.01630
4	-0.00304	0.01179	0.00014	-0.00032	-0.00400	-0.00426
5	-0.00943	0.03066	0.00009	-0.00115	0.00159	0.00004
6	-0.00553	-0.02120	0.00014	-0.00053	0.00084	-0.00525
7	-0.01349	0.01289	-0.00006	-0.00054	0.00028	-0.00266
8	-0.00422	-0.00228	0.00003	-0.00031	0.00045	-0.00255
9	-0.00825	-0.00851	0.00006	-0.00037	0.00015	-0.00403
10	0.01660	-0.00487	0.00003	-0.00031	0.00008	-0.00634
11	0.00229	-0.00335	0.00000	-0.00037	0.00118	-0.00482
	Bridge circuit qs1					
1	-0.06838	-10.10660	-0.00012	-0.02830	-0.00297	0.00854
2	0.01647	-0.00801	-0.00005	0.00008	0.00020	0.01332
3	-0.00193	-0.05614	0.00003	0.00283	-0.00095	-0.02052
4	0.00052	-0.00386	-0.00004	0.00006	0.00084	0.00704
5	0.00236	-0.00908	-0.00004	0.00167	-0.00094	-0.01098
6	0.00153	0.00654	-0.00005	0.00013	0.00086	0.00341
7	0.00332	-0.00903	0.00001	0.00104	-0.00009	-0.00592
8	0.00149	-0.00013	-0.00001	0.00007	0.00056	0.00137
9	0.00220	-0.00156	-0.00003	0.00060	0.00000	-0.00251
10	-0.00506	0.00095	-0.00001	0.00007	0.00048	0.00197
11	-0.00146	-0.00242	0.00000	0.00034	-0.00022	-0.00046

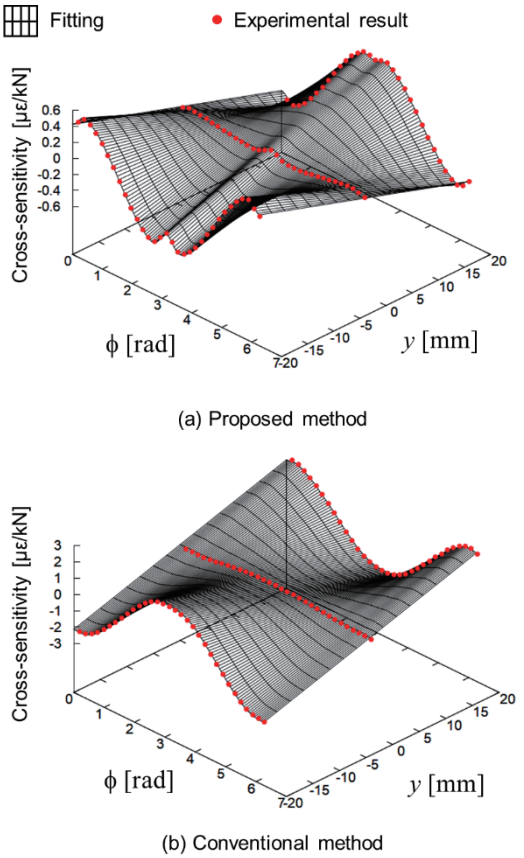

Fig. 6 Characteristics of cross-sensitivity with respect to wheel load in the proposed and conventional methods

Although it is beyond the scope of this paper, recent research has clarified that even when longitudinal force is applied to the wheel tread, an output is generated in each bridge circuit for the lateral force measurement and the characteristics can also be approximated by the form of function $f(\phi, y)$ [5]. When longitudinal force acts during a run at a curve section, this effect can also lead to errors in the lateral force measurement. On the other hand, the magnitude of the cross-sensitivity with respect to the longitudinal force is slightly smaller than the magnitude of the cross-sensitivity with respect to the wheel load. In addition, in most cases, the longitudinal force is smaller than the wheel load. Those facts mean that the influence of the longitudinal force is smaller than that of the wheel load with regard to the accuracy of the lateral force measurement. In addition to those facts, the periodic function of cross-sensitivity with respect to the longitudinal force is orthogonal to the function of sensitivity with respect to the lateral force, which means that the cross-sensitivity on the longitudinal force is zero at the point where the lateral force sensitivity is the maximum. Therefore, by introducing an intermittent method, which is one of signal processing techniques that detects only peak values of strain signals and converts to force, the influence of the longitudinal force can be negligible. In this investigation, under consideration of applying an intermittent method to the proposed method, only the effect of wheel load is examined in detail. Hereinafter, the lateral force and wheel load extracted by the intermittent method are referred to as "intermittent lateral force" and "intermittent wheel load," respectively.

3. Single-wheelset roller-rig test

3.1 Test and evaluation method

Rolling tests were carried out using a single-wheelset roller-rig test bench (Fig. 7) owned by the Railway Technical Research Institute. The instrumented wheelset was rolled for more than one minute under various conditions of the angle of attack and wheel load imbalance, and strain signals were recorded using a data recorder. The rolling speed was set to 30 km/h in all of cases. In addition to recording strain signals, the lateral contact positions between wheels and rollers were measured by using a marker. Specifically, a rolling test was performed with a marker applied to the wheel tread, and after the test was completed, the both ends of the area where the marker had peeled off were measured with a special ruler. The average value of the both ends was calculated as the lateral contact position.

The peak values were extracted from the recorded strain signals and converted to the intermittent lateral force by the following procedure:

- A low-pass filter with a cut-off frequency of 100 Hz is applied to the strain signals to remove high frequency components from the strain data for a period of 40 seconds while the roller speed is constant.
- The contact position in the circumferential direction ϕ is evaluated by Eq. (4).

$$\phi = \tan^{-1}\left(\frac{\epsilon_{qb2}}{\epsilon_{qb1}}\right) \tag{4}$$

where ϵ_{qb1} and ϵ_{qb2} are the strain outputs of the conventional bridge circuits, qb1 and qb2.

- The average values $\bar{\epsilon}_{qb1}$ and $\bar{\epsilon}_{qb2}$ of ϵ_{qb1} and ϵ_{qb2} respectively are calculated over the range of -0.02 rad $< \phi < 0.02$ rad.

The intermittent lateral forces Q_b^{int} and Q_s^{int} for the conventional and proposed method are calculated using the sensitivities with respect to the lateral forces at $\phi = 0$ rad obtained from the calibration test; the sensitivities are 33.1 με/kN for the conventional method and -10.2 με/kN for the proposed method, therefore the Q_b^{int} and Q_s^{int} are calculated as $\bar{\epsilon}_{qb1}/33.1$ and $-\bar{\epsilon}_{qs1}/10.2$ respectively. For the later discussion, the intermittent wheel load is also calculated in the same way.

3.2 Comparison of intermittent lateral forces acquired by conventional and proposed methods

In this section, the four sets of test data are evaluated as representative data of all 21 sets of test data, which are described later in detail. The four sets of data have variations in contact positions with increments of about 5 mm. Figure 8 indicates the waveforms of strains in the four sets of data. Note that the indicated waveforms were processed by the low-pass filter. The coordinate system of the contact position is defined as Fig. 9.

The comparison of intermittent lateral forces acquired by the conventional and the proposed method is indicated in Fig. 10. It is thought that the condition of the wheelset changed during the rolling test, and it was confirmed that the lateral force was distributed over a wide range in each test. A strong correlation was observed between the intermittent lateral force acquired by the conventional and the proposed method; the correlation coefficients for each test were Test 1: 0.97, Test 2: 0.99, Test 3: 0.99 and Test 4: 1.00. On the other hand, as shown in Fig. 5, the sensitivity of the proposed method to the lateral force is reduced to about 1/3 of that of the conventional method, and there were concerns that the S/N ratio would deteriorate. However, as can be seen from the waveforms shown in Fig. 8, the noise effects were at a level that could be addressed with a commonly used low-pass filter, at least in the rolling test. Therefore, the proposed method is sufficiently practical as an alternative to the conventional method. The intermittent lateral force of the proposed method tends to be generally smaller than that of the conventional method. We discuss in the next section whether this is caused by the reduction effect of the influence of the wheel load, which was discussed in the previous work [4].

3.3 Evaluation of reduction effect in cross-sensitivity with respect to wheel load

In the evaluation described in the former section, the intermittent lateral force was calculated using the average strain value around $\phi = 0$ rad. This way of calculation is equivalent to the following procedure: ϕ is set to zero in Eq. (3) then Eq. (5) is calculated.

$$\begin{aligned}\epsilon &\approx Qh(0) + Pf(0, y) \\ &= Q\sum_{n=1}^{D} C_n^{H} + P\left(y\sum_{n=1}^{D} C_n^{F} + \sum_{n=1}^{D} B_n^{F}\right)\end{aligned} \tag{5}$$

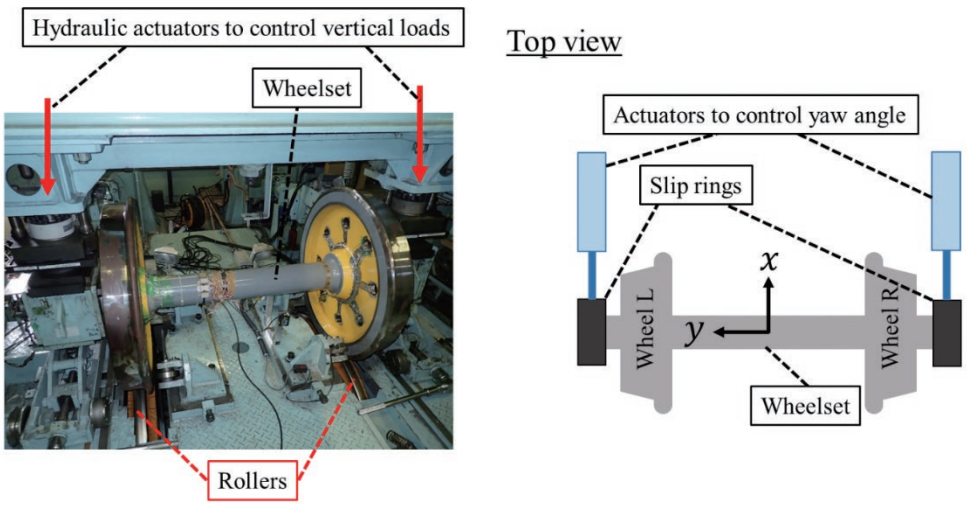

Fig. 7 Overview of the single-wheelset roller-rig test bench

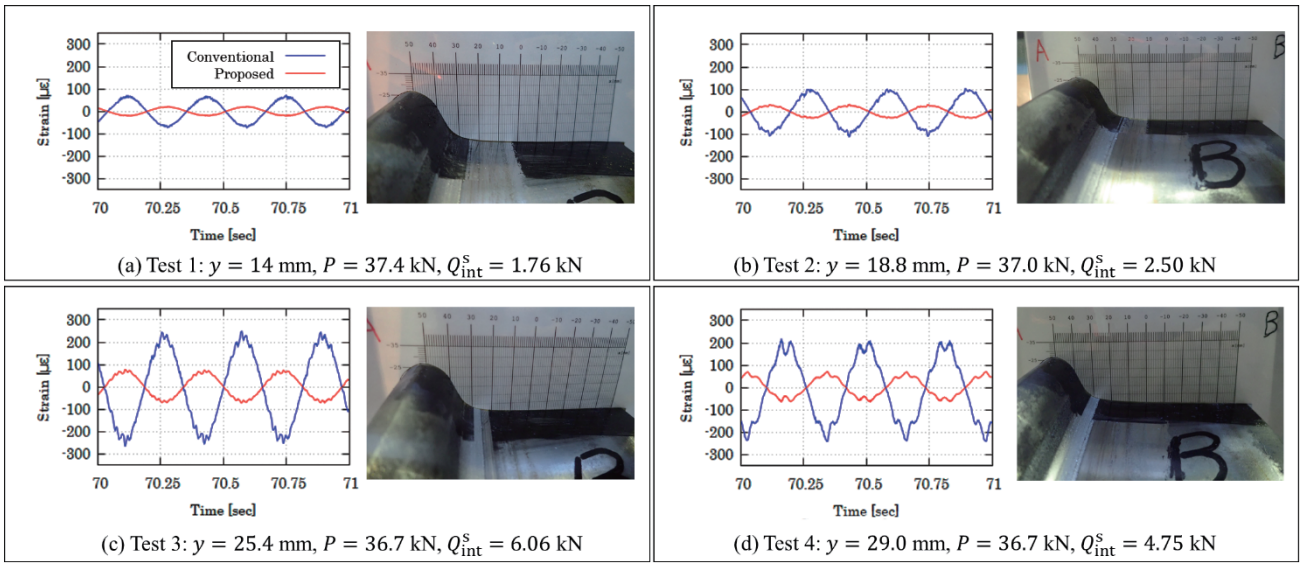

(a) Test 1: $y = 14$ mm, $P = 37.4$ kN, $Q_{\mathrm{int}}^{\mathrm{S}} = 1.76$ kN

(b) Test 2: $y = 18.8$ mm, $P = 37.0$ kN, $Q_{\mathrm{int}}^{\mathrm{S}} = 2.50$ kN

(c) Test 3: $y = 25.4$ mm, $P = 36.7$ kN, $Q_{\mathrm{int}}^{\mathrm{S}} = 6.06$ kN

(d) Test 4: $y = 29.0$ mm, $P = 36.7$ kN, $Q_{\mathrm{int}}^{\mathrm{S}} = 4.75$ kN

Fig. 8 Waveforms of strains in the four sets of data which are evaluated in the section 3.2

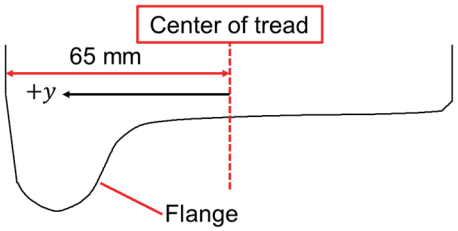

Fig. 9 Definition of the coordinate system of the contact position

Since $\Sigma_{n=1}^{D} C_n^{\mathrm{H}}$ is the sensitivity with respect to the lateral force at $\phi = 0$ rad, the process of calculating the intermittent lateral force Q^{int} from the strain ϵ can be expressed as follows:

$$Q^{\mathrm{int}} = Q + P(\alpha y + \beta),$$
$$\alpha = \frac{\sum_{n=1}^{D} C_n^{\mathrm{F}}}{\sum_{n=1}^{D} C_n^{\mathrm{H}}}, \quad \beta = \frac{\sum_{n=1}^{D} B_n^{\mathrm{F}}}{\sum_{n=1}^{D} C_n^{\mathrm{H}}} \tag{6}$$

Note that Q and P represent the true values of the lateral force and the wheel load, while the error due to the influence of the wheel load is superimposed on Q^{int}. The intermittent lateral force Q^{int} can be calculated by both the conventional and the proposed method as follows:

$$Q_{\mathrm{b}}^{\mathrm{int}} = Q + P(\alpha_{\mathrm{b}} y + \beta_{\mathrm{b}}),$$
$$Q_{\mathrm{s}}^{\mathrm{int}} = Q + P(\alpha_{\mathrm{s}} y + \beta_{\mathrm{s}}) \tag{7}$$

where α_{b}, β_{b}, α_{s} and β_{s} are the constants determined by the results of calibration tests. These constants are calculated for both the conventional and the proposed methods. Subtracting the intermittent lateral force acquired by the proposed method from that of conventional method and dividing by wheel load P results in Eq. (8).

$$\frac{Q_{\mathrm{b}}^{\mathrm{int}} - Q_{\mathrm{s}}^{\mathrm{int}}}{P} = (\alpha_{\mathrm{b}} - \alpha_{\mathrm{s}})\, y + (\beta_{\mathrm{b}} - \beta_{\mathrm{s}}) \tag{8}$$

That is, if the reduction in lateral force of the proposed method compared to the conventional method, which is indicated in Fig. 10, is because of reducing the influence of the wheel load, the difference in the intermittent lateral force divided by the intermittent wheel load should be a linear function of the lateral contact position y.

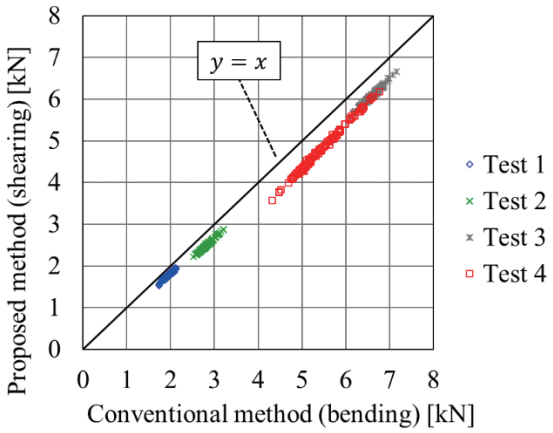

Fig. 10 Comparison of intermittent lateral forces between proposed and conventional methods

In order to verify whether the relationship shown in Eq (8) is observed in the test results of the rolling test, the total of 21 test results, including the Test 1, 2, 3 and 4 in Fig. 8, were evaluated. In concrete, the right side of Eq. (8) was calculated by using the measured lateral contact position using the marker, and the left side was calculated by using the measured lateral forces and the wheel load using the instrumented wheelset, then the relation between them was evaluated. The measured results of contact position, intermittent wheel load and intermittent lateral force for all 21 tests are shown in Fig. 11. From the figure, the contact position was distributed in the range of 5 mm to 35 mm, the intermittent wheel load was distributed in the range of 15 kN to 40 kN, and the intermittent lateral force was distributed in the range of 0 kN to 15 kN in the series of test.

The relation between measured $(Q_{\mathrm{b}}^{\mathrm{int}} - Q_{\mathrm{s}}^{\mathrm{int}})/P$, which is called as "normalized difference of lateral force," and measured contact position is shown in Fig. 12. This figure also indicates the linear function, which predicts the relation between the normalized difference of lateral force and y using the constants obtained by the calibration test α_{b}, β_{b}, α_{s} and β_{s}. The plots which indicate the experimental results are distributed near the linear function with strong

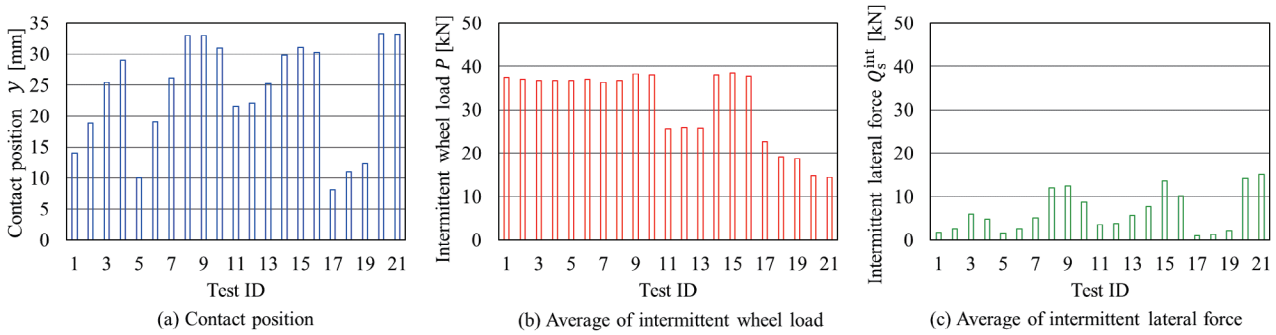

(a) Contact position (b) Average of intermittent wheel load (c) Average of intermittent lateral force

Fig. 11 Measured data of contact position, intermittent wheel load and intermittent lateral force in all 21 tests

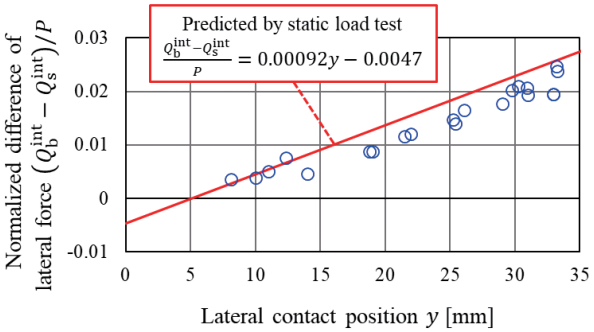

Fig. 12 Relation between the normalized difference of lateral force and the measured contact position

correlation (correlation coefficient was 0.97). This result supports the hypothesis that "the lateral force reduction in the proposed method is due to the effect of reducing the influence of the wheel load compared to the conventional method," and it was shown that the proposed method is less affected by the bending moment caused by the wheel load than the conventional method, even under the rotating conditions of the wheelset.

4. Conclusions

This paper reported the verified results for validating a method designed to measure lateral force using the shear strains of a wheel web under the rotating conditions of a wheelset. The verification through the single-wheelset roller-rig tests clarified the following:

- There was a strong correlation between the intermittent lateral force measured by the conventional and the proposed method. Although the sensitivity with respect to the lateral force is reduced to about 1/3 in the proposed method, the effect of noise was at a level that can be dealt with using a low-pass filter.
- The measurement result of lateral force by the proposed method was smaller than that by the conventional method under the condition where the wheel tread contacts the rail in the area from the center of the tread to the flange.
- The reduction of the lateral force in the proposed method was considered to be due to the effect of reducing the bending moment caused by the wheel load, which had been confirmed in static load tests carried out in previous work.

In sum, this paper shows that the proposed method is sufficiently practical as an alternative to the conventional method, since it reduces the influence of wheel load which is one of the factors that reduce accuracy.

References

[1] Bracciali, A., et al., "Review of Instrumented Wheelset Technology and Applications," *in Proceedings of the Second International Conference on Railway Technology: Research, Development and Maintenance*, No. 167, 2014.

[2] Ishida, H., et al., "Method of measuring wheel and rail contact forces and derailment quotients continuously (development of measuring device)," *Transactions of the Japan Society of Mechanical Engineers, Series C*, Vol. 63, No. 614, pp. 3417-3423, 1997 (in Japanese).

[3] Sato, K., et al., "Development of wheel load and lateral force measurement processing system combining intermittent and continuous measurement methods," *RTRI Report*, Vol. 22, No. 2, 2005 (in Japanese).

[4] Hondo, T., et al., "Measurement Method of Lateral Force Utilizing Shear Strains inside Wheel Load Measuring Holes of Instrumented Wheelset," *Quarterly Report of RTRI*, Vol. 63, No. 2, 2022.

[5] Hondo, T. et al., "Numerical and Experimental Investigations on Cross-sensitivity Characteristics of Instrumented Wheelset Associated with Longitudinal Force and Lateral Contact Position," *Journal of Computational and Nonlinear Dynamics*, Vol. 17, No. 5, pp. 051011-1—051011-9, 2021.

Author

Takatoshi HONDO, Ph.D.
Assistant Senior Researcher, Vehicle Mechanics Laboratory, Vehicle Dynamics Division
Research Areas: Vehicle Running Safety, Measurement Technology, Signal Processing

Summaries of Papers in RTRI REPORT (in Japanese)

Evaluation Method of Passenger Thermal Comfort Considering Effects of Airflow by Cross-flow Fan in Commuter Vehicles in Summer

Hiroharu ENDOH, Shota ENAMI, Fumitoshi KIKUCHI, Sachiko YOSHIE, Yasuhiko IZUMI, Jun NOGUCHI
(Vol.37, No.8, 1-8, 2023.8)

The purpose of this study is to propose a method for evaluating passenger thermal comfort in non-steady state thermal environments with airflow by cross-flow fans in commuter trains in summer. The proposed method is composed of a human thermoregulation model applicable to non-steady state thermal environments and a statistical model derived from the results of experiments conducted in commuter trains in summer. To evaluate the thermal comfort considering the influence of a cyclic wind by cross-flow fans, the proposed method converts the cyclic wind to a constant wind speed equal to the total amount of heat loss from the whole-body calculated by human thermoregulation model. Applying the proposed method to our previous research, it was confirmed that the observed data and predictions are agree well.

Monitoring Method to Prevent Rail Defects due to Water Drips in Tunnel from Occurring

Hiroyuki AIZAWA, Mitsuru HOSODA, Ryuichi YAMAMOTO, Hirofumi TANAKA, Kenya MORI
(Vol.37, No.8, 9-13, 2023.8)

There have been cases where rail defects due to water dripping in tunnels occur. This paper proposes a monitoring method to prevent this kind of rail defects from occurring. Firstly the authors investigate the cause of broken rails in tunnels, and it is revealed that rail-head irregularities and hanging sleepers cause significant bending stresses at rail foot. Field tests and numerical simulations were used to derive relationship between rail-foot stresses, rail-head irregularities and hanging sleepers. Finally, we developed a method for evaluating soundness of rails based on rail-foot stresses using data acquired by track inspection cars.

Crossing Rod Breakage Detection Method Using Surveillance Camera Images

Ryo KAGEYAMA, Nozomi NAGAMINE
(Vol.37, No.8, 15-20, 2023.8)

For early and automatic detection of crossing rod breakage caused by vehicles forcibly entering in level crossing, we developed a method for detecting crossing rod breakage using surveillance camera images. The proposed method determines the presence or absence of stripes peculiar to level crossing by extracting the color components from images and identifying the spatial frequency of the waveforms converted from the extracted color components. This paper describes the details of the proposed method and the results of performance evaluation tests.

Evaluation Method of Structural Design of Impedance Bonds Molded by Resin

Shunsuke SHIOMI, Takuro SHINDO, Tsuyoshi KAMIYA, Terutaka SATO, Naoyuki OKO
(Vol.37, No.8, 21-27, 2023.8)

Thermal effects on signalling field devices, such as high air temperature, intense sunlight, and Joule heat by return currents, can be tested independently. However, it has been difficult to evaluate the effects by multiple sources of heat. Therefore, failures of signalling field devices occasionally have occurred relating heat, such as a deformation of a structure by heat. To reduce such failures, we developed a method for evaluating thermal effects for impedance bonds using a computer simulation of heat-stress analysis. We also proposed a method for evaluating thermal effects for impedance bonds by combination of analytical and experimental methods.

Cage Wear Prediction Based on Measurement of Contact Force between Rolling Element and Cage in Traction Motor Bearings in Railway Vehicles

Daisuke SUZUKI, Ken TAKAHASHI, Fumihiro ITOIGAWA, Satoru MAEGAWA, Yoshiaki OKAMURA
(Vol.37, No.9, 1-7, 2023.9)

Bearings used in traction motors in railway vehicles are used under light loads and at high rotational speeds, so that their life is determined by cage wear due to contact with rolling elements rather than raceway flaking. In this paper, in order to predict the cage wear, we measured the forces of rolling elements which act on cage. As a result, the magnitude, duration of action, and frequency of the forces could be obtained. In addition, the forces were integrated with time to obtain impulses to show the relationship between the impulses and the cage wear.

Automating Visual Inspection for Underfloor Equipment of Railway Vehicles Using On-Track Cameras

Takashi KOJIMA, Kohei MIYAHARA, Akihito KAZATO, Masato UKAI
(Vol.37, No.9, 9-15, 2023.9)

The authors developed an image capturing system and a diagnosis algorithm for automating visual inspection of underfloor equipment of railway vehicles. The developed system consists of a line scan camera, line lights, a laser Doppler velocimeter and a computer, to scan passing vehicles from the ground. Test results using real vehicles indicate that the system can obtain detailed continuous images of the side of vehicles. The proposed algorithm using template matching and subtraction is designed to be robust against disturbances. The algorithm was tested on images captured under simulated variations in weather and the stain of underfloor equipment. As a result, the algorithm diagnosed, for example, whether the valve was fully open normally with an accuracy of AUC 0.990.

Method for Estimating Bending Stiffness of Concrete Girder during Train Passage Considering Effects of Concrete Cracks and Non-Structural Member

Munemasa TOKUNAGA, Manabu IKEDA
(Vol.37, No.9, 17-24, 2023.9)

This paper presents the results of a study on the evaluation method of concrete girder stiffness when calculating the impact coefficient and deflection. Based on the fatigue test of concrete members, we proposed an estimation formula that considers bending stiffness reduction due to crack propagation in cyclic loading. In addition, we quantified the stiffness contribution of each type of nonstructural members by means of finite element analysis for various girder structures. Finally, we proposed a simple evaluation method for the reloading bending stiffness of the girder considering the stiffness reduction due to concrete member cracks and the stiffness contribution of non-structural members.

Simple Estimation Method of Buckling Temperature of Continuous Welded Rail Considering Lateral Track Irregularities

Daiki YAMAOKA, Shingo TAMAGAWA, Yuki NISHINOMIYA

(Vol.37, No.9, 25-31, 2023.9)

The control index for buckling of continuous welded rails in Japan is set based on the lowest rail temperature increase that buckling can occur theoretically. However, there is a considerable difference between the index temperature and the buckling temperature at which the actual rail buckling occurs. Therefore, the current buckling control index may have an excessive safety margin for buckling. In order to improve the accuracy of control index, it is necessary to estimate buckling temperature affected by lateral track irregularities. In this study, we have proposed a method for easily estimating the buckling temperature of continuous welded rails considering lateral track irregularities measured by a track inspection car.

Quantitative Evaluation Method of Lifetime Prolonging Measures for Electronic Signalling Equipment

Hiroyuki FUJITA, Ken TAKASAKI, Takuro SHINDO, Tsuyoshi KAMIYA

(Vol.37, No.9, 33-39, 2023.9)

There is a strong need for prolonging the lifetime of electronic signalling equipment to reduce the replacement costs. On the other hand, the availability of equipment has become an issue due to the recent shortage of semiconductors. Since the actual lifetime of electronic signalling equipment depends on the lifetime of the electronic components and solder joints with the substrates, it is possible to prolong the lifetime by selecting suitable electronic components and improving the environment of use. In this paper, a method for quantitatively evaluating the effect of lifetime prolonging measures was investigated utilizing the developed method for evaluating the lifetime of electronic signalling equipment.

Typology of off-Train Evacuation from the Viewpoint of Information Provision and Sorting out Issues

Ayano SAITO, Takayuki MASUDA, Hiroaki SUZUKI, Tadashi TAKAI, Kana YAMAUCHI

(Vol.37, No.9, 41-47, 2023.9)

As a baseline study on the provision of information to enable a prompt evacuation from a train, the types of evacuation were grouped into three categories: immediate evacuation with passengers only, evacuation by remote instruction and evacuation by Staff Guidance. The web-based survey has shown that there is a certain degree of role awareness in helping fellow passengers each other during escape, and that cooperative behavior can be expected. It has also shown that those who understood instructions more clearly tended to act more immediately. Thus, it is considered important to inform passengers about their expected role, the flow of action to be taken, and the overall evacuation process.

Design Method for Corrosion of Reinforcing Bars in Concrete Structures by Water Penetration and Carbonation Progress

Shuntaro TODOROKI, Tetsuya ISHIDA, Hiroshi UEDA, Toshiya TADOKORO

(Vol.37, No.10, 1-8, 2023.10)

The effect of water and carbonation on the corrosion of reinforcing bars was investigated by field surveys on members with different levels of water supply. In addition, a design method for corrosion of reinforcing bars due to water penetration was verified by comparison with the cover depth where spalling had occurred, or the design cover depth determined by consideration in terms of carbonation. Even if the un-carbonation depth (=cover depth – carbonation depth) becomes less than 10 mm, when water is not supplied, the risk of the spalling of concrete is low and the corrosion rate of the reinforcing bars is slow, thus, it is important to consider the impact of water supply for the reinforcing bars. It was also confirmed that the design method based on corrosion of reinforcing bars due to water penetration is applicable.

Evaluation Method for Shear Strength of RC Pile Foundation Footing with Small Shear Span Ratio

Shuntaro TODOROKI, Toshiya TADOKORO, Yukihiro TANIMURA, Yoshinori SHINDO

(Vol.37, No.10, 9-14, 2023.10)

The authors investigate the shear failure properties of pile foundation footings with a small shear span ratio of 1.0 or less and an equation to calculate the effective width used for shear strength evaluation. The result showed that the shear strength increases with a smaller shear span ratio even when the shear span ratio is less than 1.0. In contrast, when using the conventional equation to calculate the shear strength in design, the shear strength calculated tends to be smaller as the shear span ratio is smaller, when the shear span ratio is approximately 1.0 or less. To solve this problem, we have proposed an equation to calculate the effective width used for shear strength evaluation so that the shear strength is not calculated too small even if the shear span ratio is smaller.

Cross-Section Repair of Track Slab for Tunnel Section Using Polymer Cement Mortar

Takatada TAKAHASHI, Masaru HOJO, Narita TAKAHASHI

(Vol.37, No.10, 15-22, 2023.10)

Direct seat fastening systems are used for slab tracks laid in straight sections in tunnels. A shoulder of a track slab supports the curved part of a plate-spring used in the fastening system. However, it is reported that shoulders of some track slabs are damaged due to ASR or rebar corrosion. To repair the damages, resin mortars with high material costs are generally used for cross-section repair of track slabs. Therefore, from the viewpoint of cost, we investigated the application of Polymer Cement Mortar (PCM) with lower material costs than Resin Mortar, to the cross-section repair of track slabs in tunnel sections. As the results of various tests, we confirmed that the shoulder repaired with PCM has sufficient shear capacity and trains can be passed after 2 hours of material age.

Rolling Stock Scheduling Algorithm for Temporary Timetable After Natural Disaster

Satoshi KATO, Jun IMAIZUMI, Taichi NAKAHIGASHI, Tatsuya KOKUBO

(Vol.37, No.10, 23-28, 2023.10)

In this paper, we focus on rolling stock scheduling after a large-scale natural disaster. In general, a temporary timetable is generated when some sections in of the line are partially disrupted from the damage caused by the disaster. The next step is to create a rolling stock schedule that is as close as possible to the basic schedule at the time of the timetable revision. We propose a two-phase rolling stock scheduling method based on the mathematical programming algorithm to cope with the temporarily changed timetable. In addition, we confirm that the proposed algorithm can produce a practical solution in terms of evaluation criteria and computational time.

QUARTERLY REPORT of RTRI

第 64 巻　第 4 号
2023 年 11 月 1 日　発行
監修・発行所：公益財団法人鉄道総合技術研究所
〒 185-8540　東京都国分寺市光町 2-8-38
発行人：芦谷公稔
問い合わせ：鉄道総研広報

Vol. 64, No. 4
Published date: 1 November 2023
Supervision/Publisher: Railway Technical Research Institute
Address: 2-8-38 Hikari-cho, Kokubunji-shi, Tokyo 185-8540, Japan
Issuer: Dr. Kimitoshi ASHIYA
Contact us: Public Relations, Railway Technical Research Institute
Mail Address: rtripr@rtri.or.jp

QUARTERLY REPORT of RTRI

RAILWAY TECHNICAL RESEARCH INSTITUTE

Printed in Japan